

**UCSF**

**UC San Francisco Electronic Theses and Dissertations**

**Title**

Observing conformational changes in membrane proteins using cryoEM

**Permalink**

<https://escholarship.org/uc/item/4bh6f3vb>

**Author**

Pourmal, Sergei

**Publication Date**

2023

Peer reviewed|Thesis/dissertation

Observing conformational changes in membrane proteins using cryoEM

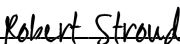
by  
Sergei Pourmal

DISSERTATION  
Submitted in partial satisfaction of the requirements for degree of  
DOCTOR OF PHILOSOPHY


in  
Chemistry and Chemical Biology

in the  
GRADUATE DIVISION  
of the  
UNIVERSITY OF CALIFORNIA, SAN FRANCISCO

Approved:

DocuSigned by:  
  
DCB8526CD1A74DB... Robert Stroud  
Chair

DocuSigned by:  
  
Yifan Cheng

DocuSigned by:  
  
6F8EED39591F4A0... Charles Craik

---

---

Committee Members

Copyright 2023

by

Sergei Pourmal

## **Acknowledgements**

I would first like to thank my Ph.D. advisor, Robert Stroud, who has enthusiastically supported me and guided my research at UCSF. He afforded me the freedom to pursue whatever I found interesting, and for that I am particularly grateful. Bob's commitment to science and his joie de vivre are a constant inspiration to those who know him. Thank you to my committee, Yifan Cheng and Charly Craik, both of whom provided invaluable advice during my graduate career and pushed me to better myself as a scientist. Thank you to my collaborators at UCSF, including Deanna Kroetz, Oren Rosenburg, and the many faculty members of the QCRG, all of whom generously offered their thoughts and suggestions during the course of my Ph.D.

I additionally want to thank my scientific advisors prior to UCSF. I thank Rich Olson at Wesleyan University for introducing me to structural biology and mentoring me as a young undergraduate. At the Sloan Kettering Institute, I thank Nikola Pavletich and Chun Zhou for the rigorous training in protein expression, protein purification, and X-ray crystallography. Thank you to Leonid Chernomordik and everyone in his group at the NIH for many enjoyable summers studying membrane biophysics.

I want to thank members of the UCSF community for generously sharing their knowledge with me. Thank you to the many members of the Stroud lab, including Thomas Tomasiak and Pawel Dominick for introducing me to the field of ABC transporters. Thank you Meghna Gupta for years of productive discussions. I would also like to thank the generous postdocs of our neighboring labs. Thank you Nicole Poweleit, Alexander Myasnikov, and Axel Brilot for training me in cryoEM sample preparation, data collection,



and data processing. Thank you David Bulkley for further hands-on training with the microscopes. Thank you Tristan Owens for helpful suggestions on purification strategies.

I would like to show my appreciation to my many friends, classmates, and colleagues from whom I learned something new every day: Sasha Dickinson, Cynthia Chio, Daniel Asarnow, Nat Hendel, Cole Helsell, Elizabeth McCarthy, Paul Thomas, and so many others over the years. Thank you to my Chemistry & Chemical Biology cohort for commiserating, and to members of the Agard Lab for the countless social and scientific conversations.

Thank you to my father, Andrei Purmal, for sharing your love of science. Thank you for tours of your labs and camping trips in New England woods. Thank you to my mother, Elena Pourmal, for everything I am today. Thank you for your love and sacrifice while raising me and Pavel. Thank you for being an inspiration to me. I proudly share this accomplishment with you.

To Julie Chen, I love you forever and always. Thank you for spending your life with me. Thank you for your constant support, your thoughtfulness, your beautiful smile. This work would not have been possible without you. To Sasha, thank you for joining us. Thank you for your constant laughs and your boundless curiosity. Thank you for our walks around Potrero Hill. I promise to always lead you to bigger puddles. To our next love, we'll meet someday soon, and then we'll share the world with you.

This dissertation is dedicated to my grandmother, Kommunara Trostina, my grandfather, Igor Trostin, and my brother, Pavel Pourmal, whose memories I will forever cherish.

## Contributions

This dissertation contains two chapters, each composed of reprinted material as it appears in the following publications:

### Chapter 1

S. Pourmal et al. “Structural Basis of Prostaglandin Efflux by MRP4.” *bioRxiv*, 2022, doi: <https://doi.org/10.1101/2022.12.22.521501>

### Chapter 2

M. Dickinson, S. Pourmal, M. Gupta et al. “Symmetry Reduction in a Hyperpolarization-Activated Homotetrameric Ion Channel.” *Biochemistry*, vol. 61, no. 20, pp. 2177–2181, 2021.

# Observing conformational changes in membrane proteins using cryoEM

## Abstract

Sergei Andreevich Pourmal

Proteins are the macromolecular machines responsible for many of life's fundamental processes. As extended polymers of amino acids, proteins fold into unique three-dimensional shapes in order to carry out their biological roles. Understanding the connection between protein structure and function has been an active area of research for much of the last century, and throughout that time the primary method of structure determination has been X-ray crystallography. Recent advances in the field of cryo-electron microscopy (cryoEM), particularly with respect to electron detectors and algorithms for image processing, have allowed the technique to reach resolutions that rival X-ray diffraction studies. Without the requirement of a crystallized sample, cryoEM opens the possibility of visualizing previously intractable protein targets as well as flexibility and motion within those proteins. My thesis focuses on the application of single particle cryoEM to study membrane proteins in lipidic environments and the conformational changes they undergo.

In the first chapter, I present a series of structures of the *Bos taurus* multidrug resistance protein 4 (MRP4). MRP4 is an ATP binding cassette transporter belonging to the ABCC family and is responsible for the rapid efflux of multiple endogenous and exogenous substrates. Included among these substrates are prostaglandins, a group of biologically active lipid molecules tied to physiological processes as diverse as inflammation and vasoactivity, and whose dysregulation is implicated in pathologies such

as cancer and thrombosis. While MRP4 plays a crucial role in localized cell-to-cell signaling as the sole prostaglandin exporter identified in eukaryotes, the molecular details of its transport activity are poorly understood. Using single particle cryoEM, I determined five high resolution structures of MRP4 along various steps of the substrate transport cycle. These structures reveal for the first time the basis of MRP4's affinity for prostaglandins and other organic anions, how substrate binding can stimulate MRP4's basal ATPase activity several fold, and the conformational changes required for substrate transport. These results broaden our understanding not only of MRP4, but also closely related members of the ABCC family.

In the second chapter, I and others describe the novel structure of *Arabidopsis thaliana* AKT1, a hyperpolarization-activated voltage-gated K<sup>+</sup> channel responsible for K<sup>+</sup> uptake by the plant's roots. AKT1 is a Shaker-like channel, and forms homo-tetramers that are under multiple, redundant levels of regulation. Our single particle cryoEM analysis revealed a potential novel form of autoinhibition via a disulfide bond between a soluble N-terminal helix and C-linker. The orientation of this covalent linkage sterically hinders the activation of AKT1's voltage-sensing domain and induces a dramatic restructuring of the tetramer from a C4-symmetric channel into a C2-symmetric one. The transitions between the two conformations of AKT1 found in the C2-symmetric channel resemble those of cyclic-nucleotide gated ion-channels upon cyclic nucleotide binding, suggesting a regulatory role for the previously unreported disulfide bond. Our proposed model of AKT1 autoinhibition provides insights into similar forms of regulation across other hyperpolarization-activated channels.

## Table of Contents

<b>CHAPTER 1: STRUCTURAL BASIS OF PROSTAGLANDIN EFFLUX BY MRP4</b>	<b>1</b>
Abstract	2
Introduction	2
Results	6
<i>Purification, nanodisc reconstitution, and functional characterization of MRP4</i>	6
<i>Structures of apo, substrate-bound and ATP-bound MRP4 determined by cryo-EM</i>	7
<i>Conformational changes upon substrate and ATP binding</i>	10
<i>Structural features of MRP4's NBDs</i>	12
<i>Substrate binding by MRP4</i>	14
<i>Structural comparison between MRP4 and the leukotriene transporter MRP1</i>	17
Discussion	19
Figures	24
Tables	51
Methods	54
<i>MRP4 expression and membrane preparation</i>	54
<i>MRP4 nanodisc reconstitution</i>	54
<i>ATPase Assay</i>	55
<i>Cryo-EM sample preparation and data acquisition</i>	56
<i>Image processing</i>	57
<i>Model building and structure refinement</i>	58
<i>Data availability</i>	59
Acknowledgements	60
Author Contributions	60

References	61
<b>CHAPTER 2: SYMMETRY REDUCTION IN A HYPERPOLARIZATION-ACTIVATED HOMOTETRAMERIC ION CHANNEL</b>	<b>70</b>
Abstract	71
Introduction	71
Results	73
Discussion	77
Figures	79
Tables	87
Table 2.1   Cryo-EM data collection, refinement, and validation statistics	87
Methods	88
<i>AtAKT1 expression and purification</i>	88
<i>AtAKT1 nanodisc reconstitution</i>	89
<i>Cryo-EM sample preparation and data acquisition</i>	90
<i>Image processing</i>	90
<i>Model building and structure refinement</i>	92
Acknowledgements	92
Author Contributions	92
References	93

## List of Figures

Figure 1.1   Functional characterization of MRP4 and identification of three stimulating substrates	24
Figure 1.2   Structures of MRP4 in multiple conformations along the substrate transport cycle	26
Figure 1.3   Comparison of the inward open, inward narrow, and outward occluded conformations of MRP4	27
Figure 1.4   Structural asymmetry between NBD1 and NBD2	28
Figure 1.5   DHEA-S and prostaglandin binding to MRP4	30
Figure 1.6   Structural comparison between MRP4 and related ABCC family members	32
Figure 1.7   Proposed translocation cycle of MRP4	34
Figure 1.8   Sequence alignment of MRP4 and MRP1 homologs	35
Figure 1.9   Biochemical characterization of MRP4	37
Figure 1.10   Image processing of nucleotide-free, substrate-free MRP4 leading to a 3.1 Å cryo-EM reconstruction	39
Figure 1.11   Image processing of DHEAS-bound MRP4 leading to a 2.7 Å cryo-EM reconstruction	41
Figure 1.12   Image processing of PGE <sub>1</sub> -bound MRP4 leading to a 3.5 Å cryo-EM reconstruction	43
Figure 1.13   Image processing of PGE <sub>2</sub> -bound MRP4 leading to a 2.9 Å cryo-EM reconstruction	45

Figure 1.14   Image processing of ATP-bound MRP4 <sub>E1202Q</sub> leading to a 3.1 Å cryo-EM reconstruction	47
Figure 1.15   cAMP does not elicit a conformational change in MRP4	48
Figure 1.16   The domains of MRP4 move as rigid bodies throughout the substrate transport cycle	49
Figure 1.17   The outward-facing occluded state of MRP4 closely resembles the structure of SUR1 bound to ADP/ATP	50
Figure 2.1   CryoEM structure and functional state of AKT1 in a lipid bilayer	79
Figure 2.2   Symmetry reduction in AKT1 and its implications for voltage activation	80
Figure 2.3   Purification of AKT1 from HEK GnTi- cells	82
Figure 2.4   Image processing of AKT1 leading to a 2.8 Å cryo-EM reconstruction	83
Figure 2.5   Cryo-EM map and model validation	84
Figure 2.6   Sequence alignment of AKT1 and other cyclic nucleotide-gated and hyperpolarization-activated channels of known structure.	85
Figure 2.7   AKT1 pore structure and hydration	86



## List of Tables

Table 1.1   Cryo-EM data collection, refinement and validation statistics	51
Table 1.2   Kinetic parameters for ATPase activity of MRP4	53
Table 2.1   Cryo-EM data collection, refinement and validation statistics	87

## Chapter 1: Structural Basis of Prostaglandin Efflux by MRP4

### Contributing Authors

Sergei Pourmal<sup>1</sup>, Evan Green<sup>1</sup>, Ruchika Bajaj<sup>2</sup>, Ilan E. Chemmama<sup>2</sup>, Giselle M. Knudsen<sup>4</sup>, Meghna Gupta<sup>1</sup>, Andrej Sali<sup>2,3,4</sup>, Yifan Cheng<sup>1,5</sup>, Charles S. Craik<sup>3</sup>, Deanna L. Kroetz<sup>2\*</sup> and Robert M. Stroud<sup>1\*</sup>

<sup>1</sup>Department of Biochemistry and Biophysics, University of California San Francisco, San Francisco, CA, USA.

<sup>2</sup>Department of Bioengineering and Therapeutic Sciences, University of California San Francisco, San Francisco, CA, USA.

<sup>3</sup>Department of Pharmaceutical Chemistry, University of California San Francisco, San Francisco, CA, USA.

<sup>4</sup>Quantitative Biosciences Institute, University of California San Francisco, San Francisco, CA, USA.

<sup>5</sup>Howard Hughes Medical Institute, University of California San Francisco, San Francisco, CA, USA.

\*Corresponding Authors

## **Abstract**

MRP4 is unique among the C family of ATP-binding cassette transporters for its role in translocating prostanoids, an important group of signaling molecules derived from unsaturated fatty acids. Using a reconstituted system, we report that a pair of prostaglandins (PGs) and the sulfonated-sterol DHEA-S preferentially enhance the ATPase activity of MRP4 over other previously proposed physiological substrates such as cyclic nucleotides or leukotrienes. We determined the cryo-EM structures of nanodisc embedded bovine MRP4 in (i) a nucleotide- and substrate-free state, (ii) in complex with PGE<sub>1</sub>, (iii) PGE<sub>2</sub>, and (iv) DHEA-S, and (v) a catalytically dead mutant E1202Q bound to ATP-Mg<sup>2+</sup>. The substrate-bound structures suggest unique features of the MRP4 binding site that distinguish its specificity for prostanoids from that of the related leukotriene transporter MRP1. The ATP-bound structure is in an outward-occluded conformation, revealing a novel state in the proposed alternate-access mechanism of MRP transport. Our study provides insights into the endogenous function of this versatile efflux transporter.

## **Introduction**

The prostanoid family of lipid mediators are important signaling molecules involved in physiological processes as diverse as inflammation, nociception, immune response, vasoactivity, and parturition [1]-[7]. Prostanoids are derived from the cyclooxygenase (COX1/COX2)-mediated metabolism of unsaturated fatty acids and subsequently converted in a tissue-specific manner into various prostaglandins (PGs) or thromboxanes

(TXs) [8]. Acting in an autocrine or paracrine fashion, secreted prostanoids activate their cognate G-protein coupled receptors, leading to modulation of intracellular  $\text{Ca}^{2+}$  or cAMP levels that affect downstream signaling and gene expression. Altered prostanoid signaling has implications for a variety of pathologies, including thrombosis, blood pressure, gastrointestinal cancers and regulation of the tumor microenvironment [9]-[11]. Synthetic prostaglandins have clinical use for induction of labor and abortions, treatment of glaucoma and pulmonary hypertension, vasodilation, and the prevention of stomach ulcers [12]-[16]. Despite the numerous physiological roles of prostanoids and the therapeutic potential of their analogs, structural details on their active transport from the cell are limited.

The efflux of prostaglandins is mediated by the multidrug resistance associated protein 4 (MRP4) [17]. Broadly expressed in tissues including the liver, kidneys, blood-brain barrier, and blood cells, MRP4 is a membrane bound ATP-binding cassette (ABC) transporter from the ABCC family that functions as a unidirectional cellular efflux pump. It is a single polypeptide chain organized as two half transporters in tandem, each consisting of a transmembrane domain (TMD) composed of six transmembrane (TM) helices followed by a nucleotide binding domain (NBD) (**Figure 1.1A**) [18]. It is the only member of the MRP subfamily that has an established role in the transport of prostanoids, including  $\text{PGE}_1$ ,  $\text{PGE}_2$ ,  $\text{PGD}_2$ ,  $\text{PGF}_2\alpha$ , and  $\text{TXB}_2$  [17], [19], [20]. Among these substrates,  $\text{PGE}_2$  is of interest as the most abundant prostanoid produced by the cyclooxygenases and for its suggested roles in cancer pathology.  $\text{PGE}_2$  promotes tumor cell growth and metastasis through the activation of E-prostanoid (EP) receptors and the transactivation

of growth factor signaling. It further facilitates cancer aggressiveness by suppressing anti-tumor immunity while enhancing tumoral immune evasion [9], [11], [21]. The requirement for PGs to be exported for EP signaling, the rapid rate of PG metabolism in the cytoplasm, and the lack of any alternative known PG exporter implicate MRP4 in pathological PG efflux. Consistent with this role for MRP4, its overexpression in breast tumors has been associated with poor prognosis [22], suggesting therapeutic potential in modulating MRP4 function.

In addition to its role in PG efflux, MRP4 has been linked to the transport of numerous structurally diverse substrates. MRP4 overlaps with other MRP family members in the transport of steroid conjugates, including dehydroepiandrosterone sulfate (DHEA-S), the steroid with the highest concentrations in human circulation and a precursor for androgens and estrogens, and estradiol 17 $\beta$ -D-glucuronide (E217 $\beta$ G), a conjugated metabolite of estradiol [23]. MRP4 has also been classified as a cyclic nucleotide transporter [24]. Studies in *Mrp4*<sup>-/-</sup> mice have linked cyclic nucleotide transport by MRP4 to vascular reactivity and resistance to hypoxic pulmonary hypertension [25], impaired platelet activation [26], and cystic fibrosis transmembrane conductance regulator-mediated chloride flux and secretory diarrhea [27], [28]. Other substrates of MRP4 identified through overexpression systems include cysteinyl leukotrienes, bile salts, folate, sphingosine-1-phosphate (S1P), cephalosporin antibiotics, and antivirals [23], [29]-[37], though to date none of these substrates, including the prostanoids, DHEA-S and E217 $\beta$ G, have been validated in reconstitution experiments.

Structural information on MRP4 and its substrate binding has long been limited to homology-based models. More recently, AlphaFold2 and other protein folding software have provided atomic-level predictions, though these models are currently limited to a single state of this dynamic transporter. In order to better understand the molecular details of MRP4 function and to identify the structural elements that define MRP4 substrate selectivity, we used cryo-electron microscopy (cryo-EM) to determine high-resolution structures of lipid nanodisc-reconstituted MRP4 under five conditions. Our nucleotide- and substrate-free (apo-), three substrate-bound (DHEA-S, PGE<sub>1</sub> and PGE<sub>2</sub>) and ATP-bound structures represent three distinct states along the MRP4 substrate translocation cycle. Along with our *in vitro* examination of MRP4 ATPase activity, the substrate-bound structures provide insights into the basis of substrate discrimination among closely related members of the MRP subfamily. Our ATP-bound MRP4 structure expands our understanding of the ABCC family conformational landscape by revealing the outward-facing occluded state, an important intermediate in the proposed alternating access mechanism of substrate translocation. This series of structures will enable further computational investigations into the role of MRP4 in transporting xenobiotic and endogenous substrates and provides a basis for designing small molecules to modulate MRP4-mediated efflux.

## Results

### Purification, nanodisc reconstitution, and functional characterization of MRP4

GFP-tagged orthologs of MRP4 were screened using fluorescence size exclusion chromatography (FSEC). *Bos taurus* MRP4, which shares 90% similarity to human MRP4 (**Figure 1.8**), was selected for its expression level and biochemical behavior and is the focus of this study. This ortholog was heterologously expressed in *Spodoptera frugiperda* (Sf9) cells with a cleavable C-terminal 8-His tag that allowed for detergent purification using metal-affinity TALON resin followed by SEC. To pursue ATPase activity assays and cryoEM structure determination in a native lipid environment, we reconstituted MRP4 into MSP E3D1 lipid nanodiscs directly on affinity resin, which substantially increased the efficiency of incorporation into nanodiscs (**Figure 1.1B**).

As Type IV exporters display substrate-dependent increases in ATPase activity [38]-[40], we used stimulation of MRP4 ATP hydrolysis to assess previously identified substrates for cryoEM analysis. The ATPase activity of MRP4 in the absence of any substrate was determined to have a  $K_m$  for ATP of 0.60 mM (95% confidence interval (CI) 0.47 - 0.77 mM) and  $V_{max}$  of 19.7 nmol min<sup>-1</sup> mg<sup>-1</sup> (95% CI 18.4 - 21.1 nmol min<sup>-1</sup> mg<sup>-1</sup>) (**Figure 1.1C**), similar to previously reported values for human MRP4 [41]; these values correspond to a baseline specific activity of 4.1 min<sup>-1</sup> (95% CI 3.8 – 4.4 min<sup>-1</sup>) assuming a total molecular weight of 210 kDa for MRP4 and two copies of MSP E3D1. PGE<sub>1</sub>, PGE<sub>2</sub> and DHEA-S (**Figure 1.1F**) stimulated the ATPase activity of MRP4 in a concentration-dependent manner (**Figure 1.9B-C; Table 1.2**), with maximal stimulation of approximately 4-fold for PGE<sub>1</sub>, and 5-fold for PGE<sub>2</sub> and DHEA-S (**Figure 1.1D**). In contrast, we observed

no concentration-dependent stimulation of ATPase activity for several other previously reported MRP4 substrates, including the cyclic nucleotides cAMP and cGMP, the nucleoside analog tenofovir, the sterol E217 $\beta$ G, the vitamin folic acid, the sphingolipid S1P, and the MRP1 substrate leukotriene C4 (LTC4) [18], [42] (**Figure 1.1D**; **Figure 1.9C-F**). As the results with PGE<sub>1</sub>, PGE<sub>2</sub>, and DHEA-S suggested the presence of a high-affinity transporter-cargo complex, we pursued structures of MRP4 bound to these three ATPase stimulating substrates.

As typically seen in other Type IV transporters, ATP-binding induces dimerization of the NBDs. The two ATPase sites are composed of residues contributed by both NBDs, as the Walker A and B motifs from one NBD form a site with the signature sequence from the other. In MRP4, sequence analysis (**Figure 1.8**) reveals that the NBD2 Walker B motif contributes a catalytic E1202 to form a canonical active ATPase site. In contrast, the NBD1 Walker B contains D560 in the corresponding position, suggesting this latter ATPase site is degenerate and catalytically compromised. In order to pursue a nucleotide-bound structure of MRP4, we introduced an E1202Q mutation (MRP4<sub>E1202Q</sub>) to prevent hydrolysis of ATP while retaining the ability to bind nucleotides. MRP4<sub>E1202Q</sub> had negligible ATPase activity, consistent with the critical role of E1202 in ATP hydrolysis and confirming the degeneracy of the NBD1 Walker B motif (**Figure 1.1E**).

### **Structures of apo, substrate-bound and ATP-bound MRP4 determined by cryo-EM**

Purified MRP4 in lipid nanodiscs was frozen in the absence of any substrate or nucleotide (apo) directly on cryo-EM grids for data collection. The resulting density map



has a resolution of 3.1 Å by the Fourier shell correlation (FSC, 0.143) criterion (**Figure 1.2A, Figure 1.10, Table 1.1**) and has well-defined density for all transmembrane helices and NBD2, which allowed the interpretation of these regions in context of the primary structure. While NBD1 is not defined at near-atomic resolution in the apo density, the domain is well resolved in the subsequent ATP-bound dataset from this study. NBD1 from the ATP-bound state was used as a starting model for positioning and refinement into the apo density. N-terminal segments of the lasso motif and the linker between NBD1 and TMD2 are unresolved.

To capture substrate-bound states of MRP4, separate datasets were collected for nanodisc reconstituted MRP4 in the presence of either DHEA-S, PGE<sub>1</sub> or PGE<sub>2</sub>. The data collected from these complexes yielded reconstructions at 2.7 Å, 3.5 Å and 2.9 Å resolution, respectively (**Figure 1.2B-D, Figure 1.11-1.13, Table 1.1**), with clear densities for the TMDs, NBD2, and the substrates in their binding sites. Portions of the N-terminal lasso motif, a common feature of ABCC family members that precedes the elbow helix of TMD1, are resolved in the DHEA-S and PGE<sub>1</sub>-bound structures. NBD1 was poorly resolved in all three substrate-bound maps, though the pose and relative orientation could be modeled following the procedure described for the apo structure.

In addition to these three stimulating substrates, a dataset was collected for MRP4 in the presence of cAMP, a substrate which failed to enhance MRP4 ATPase activity in vitro yet whose transport has been reported to be MRP4-dependent in various cell types and membrane-derived vesicle assays [24], [43]. Cryo-EM analysis of MRP4 in the presence of 1 mM cAMP (concentrations far higher than previously reported Km values

and cytoplasmic levels of this important signaling molecule) revealed a structure at 3.7 Å, with no apparent conformational change relative to apo MRP4 (**Figure 1.15A,B**) and no strong additional density observed for cAMP in the substrate binding pocket (**Figure 1.15C**). The structure of MRP4 in this condition was not modeled.

A final image dataset was collected under saturating ATP-Mg<sup>2+</sup> conditions, with substrate added to promote progression through the transport cycle. MRP4<sub>E1202Q</sub> in the presence of nucleotide and PGE<sub>2</sub> resulted in a 3.1 Å resolution map with high resolution throughout the transporter, including both NBDs bound to ATP and magnesium (**Figure 1.2E, Figure 1.14, Table 1.1**). The NBD models built into this map were used to fit NBDs into the apo and substrate-bound states. All five models were refined into their respective densities, and together reveal three distinct conformations of MRP4 at high resolution, including the first structure of an ABCC family exporter in an inward closed, outward-occluded state (**Figure 1.2E**).

The overall architecture of MRP4 resembles that of other mammalian ABC transporters, with two halves each consisting of a TMD and a cytoplasmic NBD, on a single polypeptide chain (**Figure 1.1A**). An N-terminal lasso motif consists of a membrane-embedded helix that packs against TM helices 3, 10 and 11 before continuing into a second extended helix that runs parallel to the membrane's inner leaflet. The TMD-NBD halves are configured in a pseudo-2-fold symmetric arrangement perpendicular to the membrane, with an unstructured, flexible 82-residue linker connecting NBD1 and TMD2; this linker remains unresolved in all five structures. Similar to other type IV ABC exporters, a pair of TM helices are domain swapped from one TMD to the other, so that

helices 1, 2, 3, 6, 10 and 11 form one distinct transmembrane bundle, and TM helices 4, 5, 7, 8, 9 and 12 form another (**Figure 1.2A-E**). This helical swapping permits extended cytosolic loops in either TMD to interact with both NBD1 and NBD2, allowing for allosteric coupling between soluble and membrane-bound regions. The NBDs of MRP4 each contain a RecA-type core featuring the highly conserved Walker A, Walker B and signature sequence motifs that coordinate the binding and hydrolysis of ATP (**Figure 1.8**). Immediately following NBD2 is a 27-residue, unstructured C-terminal linker containing the terminal PDZ-binding sequence 'ETAL', which interacts with PDZ adaptor proteins to modulate cell surface expression of MRP4 [44].

### **Conformational changes upon substrate and ATP binding**

The apo state of MRP4 is in an inward open conformation. A solvent-filled cavity ( $\sim 11,000 \text{ \AA}^3$ ) is present between the two transmembrane bundles, extending from the cytoplasm into the lipid bilayer, ending at the interface of the bundles and the site of substrate binding. The bundles are at their maximal observed separation and the substrate binding site is accessible, characterized by a  $17.1 \text{ \AA}$  distance between the backbone  $C\alpha$  of a pair of substrate-binding residues, F211 from TMD1 and W995 from TMD2 (**Figure 1.3A**). The NBDs are oriented in a quasi-symmetric head-to-tail fashion and are separated from one another by about  $27 \text{ \AA}$  at either of the two ATPase sites (**Figure 1.3B**), as measured by the  $C\alpha$  distance between the signature sequence serine of one NBD and the Walker A glycine of the other NBD.

MRP4 undergoes a clamshell-like closure upon substrate binding. The angle between the two transmembrane bundles decreases by 20°, leaving the central cavity more constricted (~5,400 Å<sup>3</sup>) compared to the apo state. Though this conformation is narrower, substrate-bound MRP4 remains open toward the cytoplasm. At the substrate-binding site, the distance between F211 and W995 is reduced by 1 Å, indicating only modest rearrangements in the transmembrane region (**Figure 1.3A**). More pronounced conformational changes are observed in the distal cytoplasmic portions of MRP4, where the two NBDs move closer together and are now slightly askew. The narrowing of the transporter results in unequal distances of 8 and 15 Å between the Walker A of one NBD and signature sequence of the other NBD (**Figure 1.3B**). Binding of any of the three ATPase stimulating substrates results in similar changes in MRP4. The largest RMSD among the three substrate-bound structures is 1.2 Å, suggesting they represent a common substrate-bound conformation (**Figure 1.16E**).

The structure of MRP4<sub>E1202Q</sub> in the presence of PGE<sub>2</sub> and ATP exhibits substantial global changes compared to apo and substrate-bound MRP4. The NBDs dimerize around two copies of ATP-Mg<sup>2+</sup> and the transmembrane bundles tightly pack in a parallel orientation, resulting in a conformation that is closed to the interior of the cell (**Figure 1.3A,B**). The cytoplasmic portions of TM3 and TM10 contact TM4 and TM9 respectively, forming an intracellular gate that removes access to the central cavity. The movement of the transmembrane bundles occludes the substrate binding site, as the backbones of F211 and W995 move 4 Å closer and their sidechains make van der Waals contacts, preventing substrate binding. This closure of MRP4's soluble cavity follows transport of

substrate across the membrane, consistent with the lack of observed PGE<sub>2</sub> density in this state.

The extracellular surface of MRP4 remains closed and is highly superimposable across all states (**Figure 1.3C**). Hydrophobic residues I117, F352, L735 and L981 pack together to form an extracellular gate that seals the interface of the two TMDs. The presence of a closed gate in our ATP-bound structure suggests that the substrate exit pathway at the extracellular face can reset independent of ATP hydrolysis and NBD dissociation, possibly to maintain unidirectional transport. Throughout MRP4's substrate transport cycle, the two halves of the transporter move as rigid bodies around a pivot point at the extracellular surface and show only minor conformational rearrangements within the pair of TMDs and NBDs (**Figure 1.16A-D**).

### **Structural features of MRP4's NBDs**

The interface between the TMDs and NBDs is essential for connecting substrate transport to ATP hydrolysis. As in other type IV ABC exporters, a pair of coupling helices (CH) in the loops between the domain-swapped TMs 4,5 and 10,11 fit into a shallow cleft in either NBD (**Figure 1.4B,C**). Compared to NBD1, NBD2 contains an insertion of 13 residues between the Walker A motif and the signature sequence (**Figure 1.4A**). These residues (1099-1111) form two short helices that cap the distal end of the NBD2 cleft and tightly pack with the linker between TM12 and NBD2 (**Figure 1.4C**). H1111 from the second inserted helix hydrogen bonds with E292 from TM5 while simultaneously forming p-p interactions with W1025 from the TM12-NBD2 linker. A turn of the helix away, R1114

forms a salt bridge with E1022, further stabilizing contact with the linker (**Figure 1.4D**). The absence of a corresponding region in NBD1 results in a smaller interface and fewer contacts with the cytoplasmic extensions of transmembrane helices (**Figure 1.4B**), possibly contributing to the lower resolution of NBD1 density observed across apo- and all substrate-bound states (**Panel F of Figure 1.10-1.14**).

In the ATP-bound state, clear density defines the ATP and  $Mg^{2+}$  in the E1202Q mutated consensus site, and in the degenerate ATP binding site (**Figure 1.14B,F**). ATP binding is mediated in both sites by highly conserved features. These include electrostatic interactions between  $Mg^{2+}$  and the Walker A motif (K451, K1081), and between phosphates and the Walker B motif (D560, E1202Q), the Q loop (Q480, Q1122) and the His loop (H592, H1233) from one NBD and the signature sequence (S536, S1178) from the other NBD (**Figure 1.4E,F**). Aromatic residues (W419, Y1050) coordinate the adenine rings of ATP through  $\pi$ - $\pi$  interactions (**Figure 1.4E,F**). The distance of the catalytic carboxyl group of D560 from the phosphorus of the  $\gamma$ -phosphate of ATP of 4.6 Å in the E1202Q mutant is increased to 6.1 Å in the inactive degenerate site. This increased separation accounts for the inability of D560 to catalyze ATP hydrolysis at the degenerate site. Residues from CH1 and CH3 are also important in coordinating ATP binding. Specifically, N183 and D814 coordinate the NH2 group of the adenine ring in the degenerate and consensus site, respectively (**Figure 1.4E,F**).

## Substrate binding by MRP4

PGE<sub>1</sub> and PGE<sub>2</sub> were found to stimulate MRP4 ATPase activity. Both are composed of 20 carbon atoms, organized as a cyclopentanone core (C8-C12) with two alkyl chain substituents (the  $\alpha$  chain, C1-C7, and  $\omega$  chain, C13-C20). These two PGs share a carboxyl at C1, a ketone at C9, hydroxyls at C11 and 15, and a carbon-carbon double bond at C13 (**Figure 1.1F**). PGE<sub>1</sub> differs from PGE<sub>2</sub> only by the saturation of a second carbon-carbon double bond at C5, and both substrates share a similar pose when bound to MRP4. Though the map for PGE<sub>2</sub>-bound MRP4 is higher resolution than the PGE<sub>1</sub>-bound sample, either substrate can be confidently placed in its respective density. Both PGE<sub>1</sub> and PGE<sub>2</sub> bind MRP4 in the solvent-accessible central cavity, engaging residues from both TMD1 and TMD2 (**Figure 1.5C,D**). The binding site is a narrow channel composed of a large hydrophobic region and pockets of charged residues that coordinate the substrate's polar groups (**Figure 1.5B**).

In either PG-bound structure, the alkyl chains and the cyclopentanone core are wedged between W995 on TMD2 and a hydrophobic patch on TMD1. F156, F211, F324, L363, L367, and F368 form extensive van der Waals contacts with the 20-carbon backbone. The shared polar substituents of PGE<sub>1</sub> and PGE<sub>2</sub> serve to further orient the substrates. The C1 carboxyl sits in a positively charged pocket (P-site #1) located between TM 2, 11, and 12. The group forms salt bridges with R946 and R998, and maintains additional electrostatic interactions with H152, Q160 and Q994. The C11 hydroxyl and the C9 ketone substituents of the cyclopentanone ring point toward a narrow solvent-accessible cavity that extends above the substrates toward the extracellular half

of MRP4, while the C15 hydroxyl of either PG faces a pocket on TM9 formed by D842, Q845, and T846. Taken together, the combination of a hydrophobic core, the  $\alpha$  chain carboxyl, and the C9, 11 and 15 substituents allows MRP4 to bind and translocate these PGs specifically.

In addition to these two prostanoids, we also found that DHEA-S stimulated MRP4 ATPase activity. The sterol core of DHEA-S is conjugated by a sulfate ester at the  $3\beta$  position and has a ketone substituent on C17, providing polar groups at either end of the aliphatic sterol core for electrostatic interactions (**Figure 1.1F**). The map of DHEA-S-bound MRP4 is of high resolution (2.7 Å), allowing for definitive assignment of the substrate and relevant sidechain conformations. MRP4 binds DHEA-S in the same site as PGE<sub>1</sub> and PGE<sub>2</sub>, using residues from both TMD1 and TMD2 (**Figure 1.5E**). The binding site residues in all three substrate-bound structures adopt similar rotamers, revealing a common substrate-bound state.

The 17-ketosteroid backbone of DHEA-S makes extensive van der Waals contacts through its  $\beta$  face with the hydrophobic patch formed by residues from TMD1. Residues L363, L367, and F368 intercalate between the two methyl substituents of DHEA-S, while F156, F211, and F324 pack against the periphery of the substrate's sterol core. W995 from TM12 stacks against the  $\alpha$  face of DHEA-S, and the indole ring of W995 hydrogen bonds with the carboxyl of D842. The basic P-site #1, composed of H152 from TM2, R946 from TM11, and R998 and Q994 from TM12, surrounds the steroid's ketone moiety and an ordered water. The  $3\beta$  sulfate lies in a distinct pocket of positive charge (P-site #2) at the interface of TM6 and TM9, where R362 and Q849 form electrostatic interactions with



one of the sulfate's three non-bridging oxygens. A second oxygen is coordinated by Q845 and makes a water-mediated interaction with D842, creating a network of interactions that links the sulfo group to W995. The third oxygen is not coordinated by the protein but instead faces a narrow solvent-filled tunnel that continues in the direction of the extracellular face. Neither PGE<sub>1</sub> nor PGE<sub>2</sub> make notable contacts with the sidechains directly involved in binding the sulfo-group of DHEA-S.

Although the two helical bundles clamp around the substrates in all three structures, there is little change to the rotamers of most substrate-binding residues compared to the apo state (**Figure 1.5A**). The few residues that adopt new conformations include F156 and F324, which flip to line the periphery of the hydrophobic face of TMD1. The repositioning of F156 allows for R946 to rotate from facing out of the helical bundle (toward the lasso motif, partially resolved in the DHEA-S and PGE<sub>1</sub> bound structures) to facing in toward the central cavity, where its guanidino group contributes to P-site #1. A similar inward rotation by H153 adds further positive-charge character to the pocket relative to the apo state (**Figure 1.5B**).

In the ATP-bound state, MRP4's transmembrane regions are in an arrangement incompatible with substrate binding. The two halves of the transporter have rotated inward toward the central cavity and F211, L367, and F368 from the hydrophobic face of TMD1 are within van der Waals contact distance of W995, sterically preventing DHEA-S or either PG from occupying the site (**Figure 1.5F**). ATP-binding also results in the intrusion of TMD2 hydrophobic residues into the regions of positive charge at either end of the substrate binding pocket. P-site #1 is disrupted by the insertion of F156 and H152,

displacing the substrate binding residues Q994 and R998. Q994 rotates away to neutralize D953 from TM11, while R998 adopts electrostatic interactions with Q160 and Q999 and forms a salt bridge with E1002 (**Figure 1.5G**). At the other end of the substrate binding pocket, F324 occupies the former site of the DHEA-S sulfo group in P-site #2 (**Figure 1.5H**). Of the residues previously involved in coordinating the sulfate's oxygens, R362 and N849 hydrogen bond with one another, while N845 flips away and is stabilized by the backbone carbonyl of L321. The tight packing observed at both P-sites and between the hydrophobic face on TMD1 and W995 from TMD2 is consistent with substrate expulsion from the binding site, though no clear exit pathway is present.

### **Structural comparison between MRP4 and the leukotriene transporter MRP1**

MRP4 shares 37% sequence identity with the closely related and well-studied MRP1 (**Figure 1.8**). While both are recognized as transporters of amphipathic organic anions, only MRP1 is well described as a transporter of glutathione conjugates, including the eicosanoid LTC<sub>4</sub>. In our studies, LTC<sub>4</sub> failed to stimulate MRP4, unlike reported effects on MRP1 [45]. Differences in the binding sites of substrate-bound MRP4 and MRP1 are consistent with their respective substrate specificities. The structure of DHEAS-bound MRP4, when superimposed onto LTC<sub>4</sub>-bound MRP1 (PDB ID: 5UJA), aligned via TM bundle 2, shows that the MRP4 substrate binding site is narrower and lacks shape complementarity to the leukotriene (**Figure 1.6A**). TM bundle 1 of MRP4 is rotated toward the central axis of the transporter by ~13° compared to its position in MRP1, resulting in

an apparent clash between TM2 residues in MRP4 and the glutathione moiety of LTC<sub>4</sub> (**Figure 1.6B**).

Per residue differences between the binding pockets of MRP4 and MRP1 may further explain the lack of LTC<sub>4</sub> stimulation by MRP4. Of the fifteen MRP1 residues involved in LTC<sub>4</sub> binding, ten are identical or similar at the equivalent positions in MRP4, while the remaining five are altered (**Figure 1.6C**). Two MRP1 residues (K332, H335) that hydrogen bond with a carboxyl from the LTC<sub>4</sub> glutathione moiety are replaced by a threonine and a glutamic acid in MRP4, forming an acidic pocket in place of the basic pocket in MRP1 (**Figure 1.6D**). M1092, part of the hydrophobic region of the MRP1 binding site that packs against the lipid tail of LTC<sub>4</sub>, is equivalent to D842 in MRP4, which has a crucial role in orienting polar groups of DHEA-S and the PGs. T550 in MRP1 is replaced by L321 in MRP4, which could sterically clash with LTC<sub>4</sub> in the binding site. Together, these differences can account for the lack of substrate specificity of MRP4 for glutathione conjugates while maintaining transport of other organic anions.

The molecular structure of ATP-bound MRP4 illuminates a new state along the ABCC family substrate transport cycle, differing substantially from the ATP-bound state of MRP1 (PDB ID: 6BHU) (**Figure 1.6E**). Whereas MRP1 is outward open upon ATP-binding and contains a narrow channel extending between helices 6,11,12 and 17 from the substrate binding residues to the extracellular milieu, the ATP-bound MRP4 structure contains a closed extracellular gate with no apparent substrate exit tunnel. The closure of this extracellular pathway is independent of ATP hydrolysis or subsequent phosphate release and supports the 'alternating-access' mechanism for directionality of substrate

transport where the extracellular face of the exporter resets prior to the cytoplasmic portions of the transporter.

## Discussion

Our series of structures offer insights into the mechanism of substrate recognition and translocation by the organic anion transporter MRP4 (**Figure 1.7**). Based on our structures and on the closely related MRP1<sub>E1454Q</sub> bound to ATP-Mg<sup>2+</sup>, we propose the following translocation model for MRP4. In the inward-open apo state, the amphipathic substrate-binding site is located in the large central cavity between two helical bundles. The hydrophobic region on TMD1 and at least two distinct pockets of positive charge allow MRP4 to recognize organic anions of varying chemical scaffolds. In our PG and DHEA-S bound structures, residues from both TMDs engage the substrates, bringing the two helical bundles in toward the central axis of the transporter. The inter-NBD distance is shortened by up to 19 Å in the resulting inward-open narrow conformation, priming the NBDs for an accelerated rate of dimerization in the presence of ATP-Mg<sup>2+</sup>. Nucleotide binding drives the global conformational transition that results in substrate transport across the membrane. Our ATP-bound MRP4<sub>E1202Q</sub> features dimerized NBDs and no observable exit pathway in the TMD region linking substrate-binding residues to the extracellular space. Consistent with an alternating access model, this structure represents a state subsequent to substrate translocation, where the extracellular gate has closed and ATP-hydrolysis and phosphate release have not yet reset the cytoplasmic portions of the transporter.

Our ATP-bound MRP4 structure stands in contrast to that of ATP-bound MRP1, where cryo-EM analysis of the analogous Walker A mutant MRP1<sub>E1454Q</sub> in the presence of ATP-Mg<sup>2+</sup> exclusively resolved an outward-open transporter. Extensive processing of our MRP4<sub>E1202Q</sub> dataset provided no evidence for an outward-open conformation. Several 2D classes, which together represent a minority of total particles, show MRP4 to be inward-open, and the low-resolution map using particles from those classes matches our apo structure (**Figure 1.14A**). These results suggest that the outward open conformation of MRP4 may be more transient than that of MRP1, representing subtle differences in the energy landscape of the two related transporters.

Outward-occluded states have been reported for the type IV bacterial exporters MsbA [46], TmrAB [47], Cgt [48], and McjD [49], as well as the eukaryotic phosphatidylcholine exporter ABCB4 [50]. Though the precise helical organization differs between each transporter, these outward-occluded structures are thought to represent similar states in the above model of substrate transport. The structure of ATP-bound MRP4 most strongly resembles the conformation of the ADP/ATP bound state of the ABCC family member SUR1 (**Figure 1.17A-C**), a sulphonylurea receptor that acts as the ADP sensing subunit of the KATP channel [51]. Despite SUR1 sequence homology to the MRP subfamily and overall structural resemblance to a canonical ABC transporter, it has no known transport substrates and is thought to exclusively regulate channel activity. The ATP-bound MRP4 and ADP/ATP-bound SUR1 both contain a closed extracellular gate and tightly packed TMDs sealed off from the cytoplasm, suggesting conformational similarity of MRP4 to the ABCC family extends beyond the MRPs.

We show that PGE<sub>1</sub>, PGE<sub>2</sub> and DHEA-S are preferred over other previously reported substrates, stimulating MRP4 ATPase activity several fold with apparent K<sub>m</sub> values in the micromolar range. Our substrate-bound structures are consistent with this high affinity, revealing a binding site that can accommodate multiple species of organic anions. MRP4 sequesters the non-polar cores of both PGs and DHEA-S between the hydrophobic regions of TMD1 and W995 on the opposing face of the pocket. This interaction mimics the ‘tryptophan-sandwich’ observed in the LTC<sub>4</sub>-MRP1 bound structure [45], and is likely a common feature across the MRP subfamily used to bury hydrophobic cargo. The substrate-induced transition in MRP4 from the inward open apo- to inward open-narrow results in the formation of two distinct positively charged pockets, either through sidechain flipping (as in P-site #1 with R946) or a simple clamping of the TM bundles (as in P-site #2). Both P-sites are capable of coordinating anionic groups, and their positioning at opposite ends of the binding site likely contributes to the diversity of substrates recognized by MRP4. All three substrate-bound structures are consistent with previous MRP4 mutagenesis studies that identified critical roles for F368, W995 and R998 in substrate transport [52], [53].

Our two PG-bound structures reveal comparable interactions between MRP4 and the C1 carboxyl, cyclopentanone core, and the C15 hydroxyl of either PG. Given that these functional groups are common to the other prostanoids shown to be transported by MRP4, including PGD<sub>2</sub>, PGF<sub>2α</sub>, and TXB<sub>2</sub> [17], [19], [20], it is likely that they bind through similar contacts. Furthermore, these chemical features are shared by many other PGs,

suggesting the diversity of PGs and their analogs transported by MRP4 may be currently underappreciated.

The result that PG and DHEA-S stimulate MRP4 ATPase activity contrasts with the remaining substrates tested, including the cyclic nucleotides. Despite reports which identify MRP4 as a nucleotide transporter [24], [52], [55], high concentrations of cAMP and cGMP did not notably stimulate MRP4 ATPase activity in vitro. Our cryoEM results failed to confirm a high affinity complex between cAMP and MRP4, with the final reconstruction lacking both an observed density for cAMP and any notable conformational change compared to the inward-open apo state. While we cannot rule out cAMP as an MRP4 substrate, these results suggest that any transport of cyclic nucleotides in our reconstituted system occurs at or below the basal activity of MRP4, and that cAMP binding does not induce an inward-open narrow state. Downstream signaling of various PGs through their respective GPCRs affects the levels of cytoplasmic cAMP [56], providing one possible mechanism for regulation of this cyclic nucleotide by MRP4. Further investigations will be necessary to clarify the precise molecular details of transport of cAMP and other non-stimulating substrates by MRP4.

Our study provides the first atomic-level descriptions of MRP4 in three distinct conformations and reveals the basis of its organic anion specificity. The structures of PGE<sub>1</sub> and PGE<sub>2</sub> bound to MRP4 underscore the role of this transporter in prostaglandin efflux, a signaling mechanism central to numerous physiological processes. The OF-occluded structure fills in a previously unobserved but assumed state of the MRP translocation cycle and can be used as the basis for homology models of other MRPs.

Our series of IF and IF-narrow structures will provide the groundwork for computational studies aimed at validating endogenous and xenobiotic substrates of MRP4 and will aid in structure-guided designs of inhibitors for this promiscuous transporter. Improved understanding of MRP4 function will aid in addressing multidrug resistance and transporter dysregulation.



# Figures

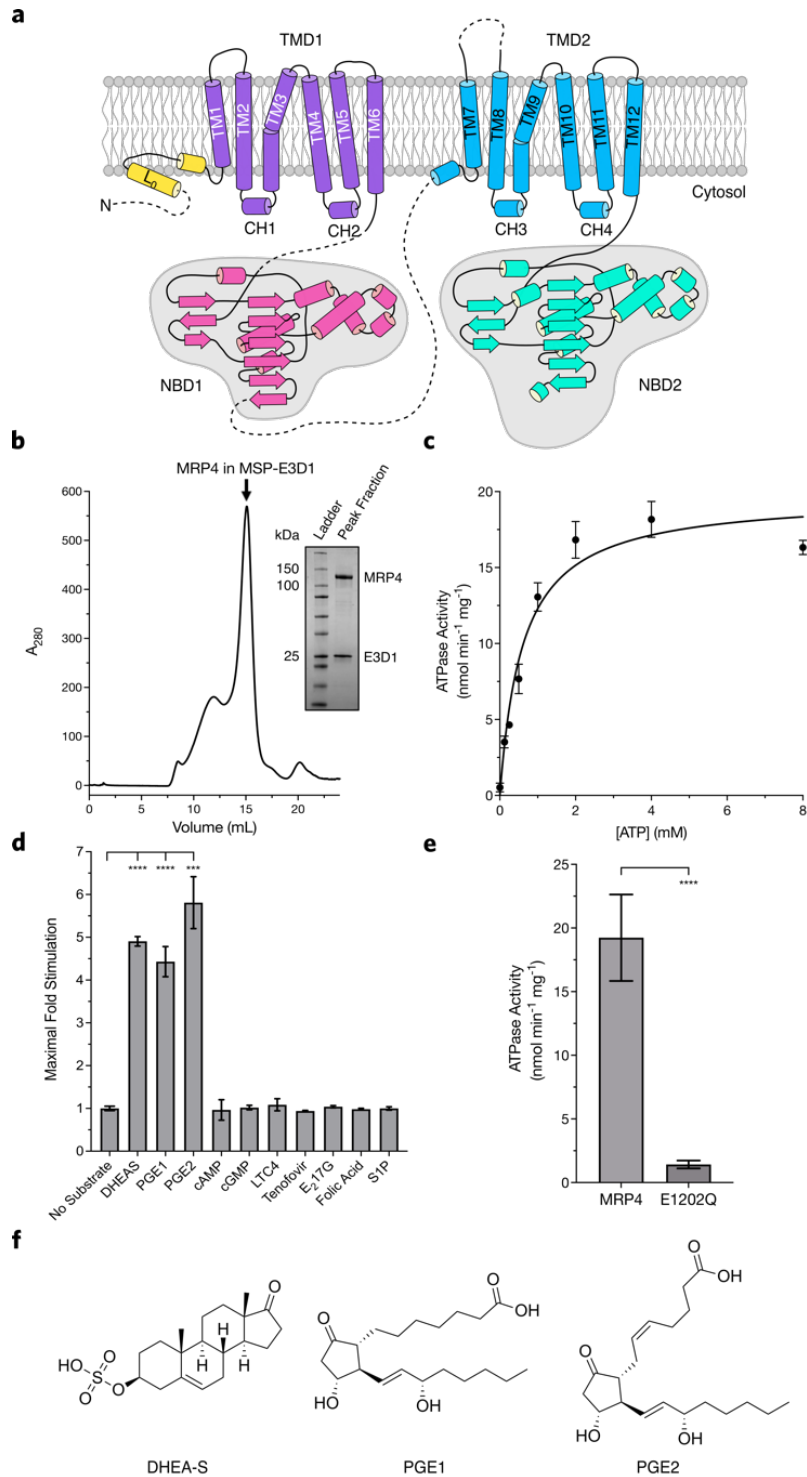


**Figure 1.1 | Functional characterization of MRP4 and identification of three stimulating substrates**

**a**, Schematic illustrating the domain architecture of MRP4 with residue numbers at domain boundaries indicated. L<sub>0</sub>, N-terminal loop domain (yellow); TMD1, transmembrane domain 1 (purple); NBD1, nucleotide-binding domain 1 (pink); TMD2, transmembrane domain 2 (blue); NBD2, nucleotide-binding domain 2 (cyan). **b**, Gel-filtration chromatography profile of WT MRP4 embedded into MSP-E3D1 lipid nanodiscs. SDS-PAGE analysis of peak fraction is inserted on the right, visualized by Coomassie blue staining. **c**, ATPase activity of nanodisc embedded MRP4. Data shown are the mean  $\pm$  SD for 3 technical replicates and fit to the Michaelis-Menten equation. Source data are provided as a Source Data file. **d**, WT MRP4 ATPase activity with 4 mM ATP in the presence of previously reported substrates. ATPase activity shown is for the highest concentration tested for a given substrate, normalized to MRP4's basal activity without a substrate. Titration curves at different concentrations of a given substrate and the effects on ATPase activity are in **Figure 1.9A-F**. Data shown are mean  $\pm$  SD for 3 technical replicates. **e**, Comparison of WT MRP4 and MRP4<sub>EQ</sub> ATPase activity in lipid nanodiscs. Data shown are mean  $\pm$  SD for 3 technical replicates. **f**, Structures of previously reported transport substrates found to stimulate MRP4 ATPase activity.

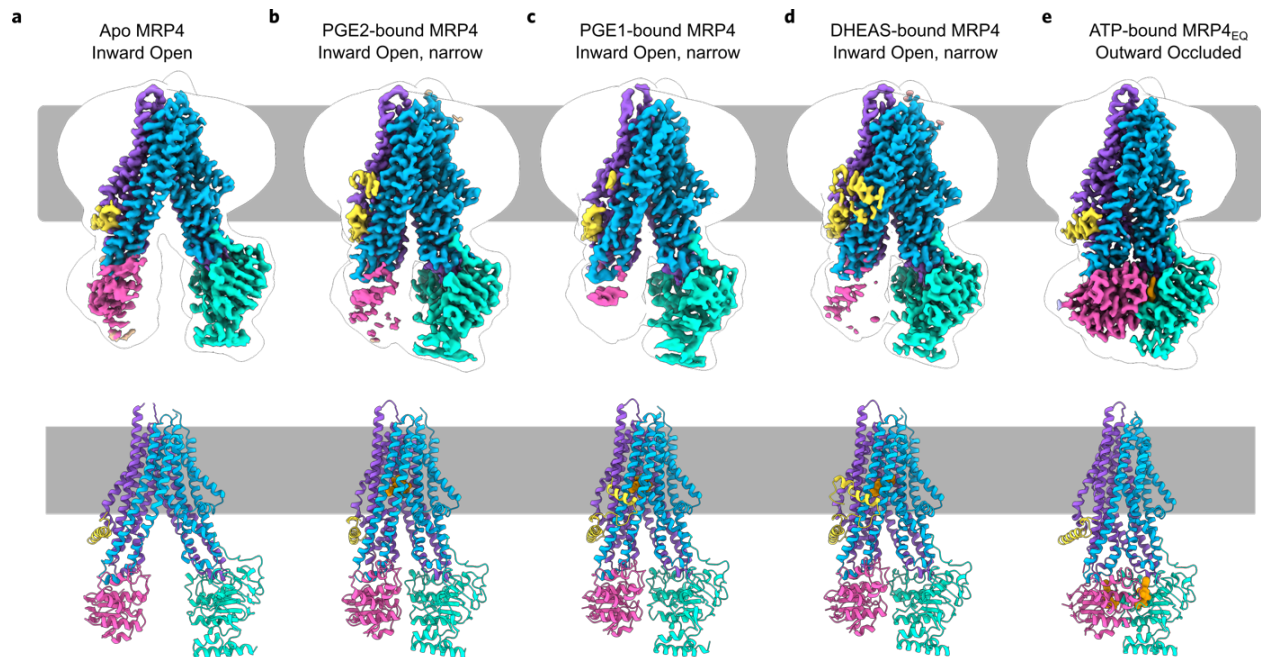


**Figure 1.2 | Structures of MRP4 in multiple conformations along the substrate transport cycle**

Side views of the cryo-EM reconstruction and atomic model of **a**, inward open, apo-conformation of MRP4, **b**, inward open narrow, DHEA-S bound MRP4 **c**, inward open narrow, PGE<sub>1</sub> bound MRP4, **d**, inward open narrow, PGE<sub>2</sub> bound MRP4, and **e**, outward occluded, ATP-Mg<sub>2</sub><sup>+</sup> bound MRP4<sub>E1202Q</sub>. The sharpened electrostatic potential maps shown were generated using DeepEMhancer. Domains in sharpened maps and models are colored as in Figure 1a. A transparent low-pass filtered envelope depicts density for the nanodisc and poorly resolved NBDs. Membrane boundaries are represented by cartoon. DHEA-S, PGE<sub>1</sub>, PGE<sub>2</sub>, and ATP-Mg<sub>2</sub><sup>+</sup> are shown as orange spheres in their respective structures.

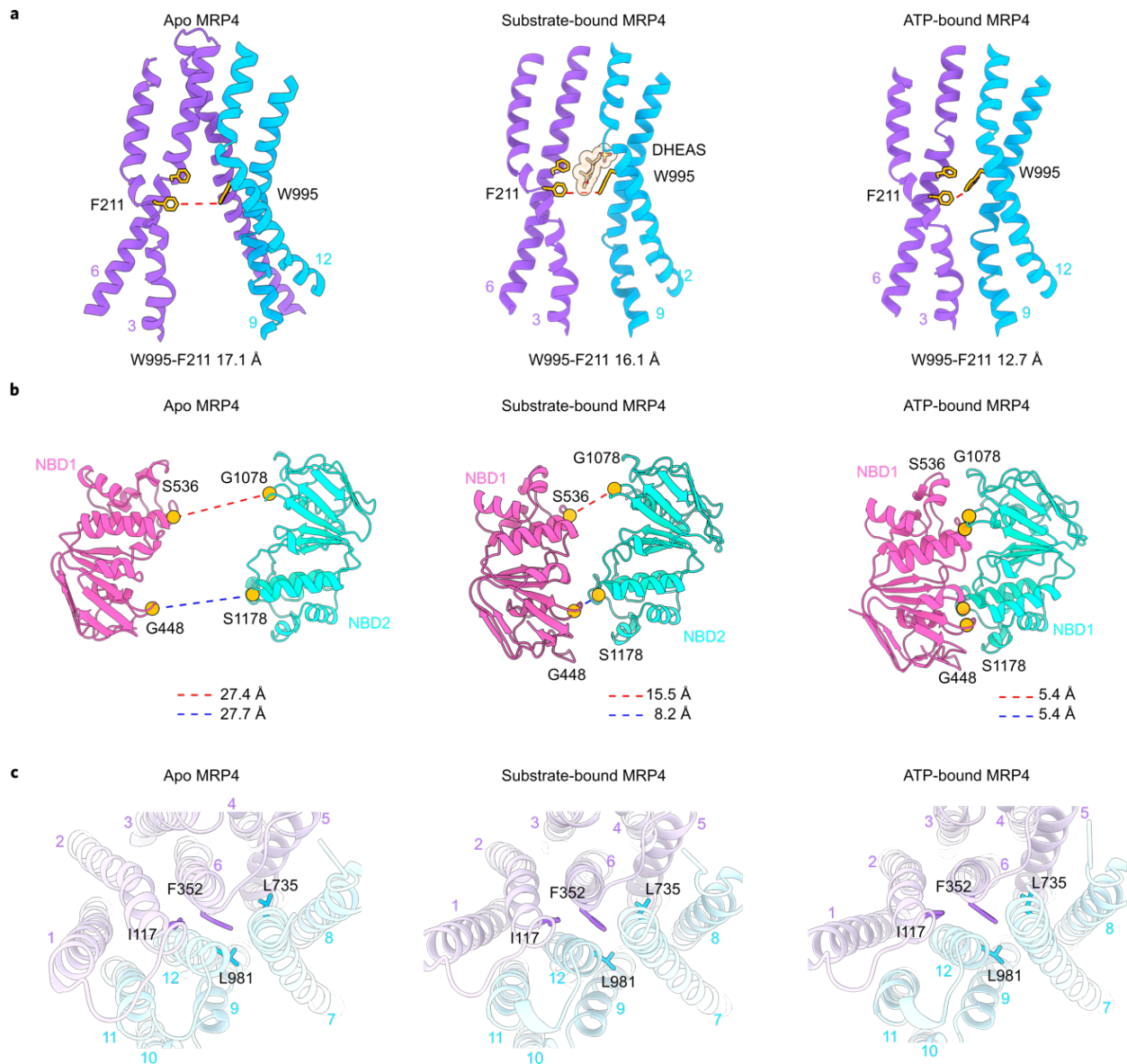


### Figure 1.3 | Comparison of the inward open, inward narrow, and outward occluded conformations of MRP4

**a**, Side view of the TMDs from the plane of the membrane for apo-, substrate-bound (DHEA-S bound structure shown), and ATP-bound states. A pair of substrate-binding residues from either TMD is shown in stick representation. The distance between these residues is drawn as a red dashed line, with values indicated in each panel. **b**, Bottom view of the NBDs, seen from the direction of the cytoplasm. Ca of signature sequence serines and Walker A glycines shown as orange spheres. Distances between opposing pairs of residues are shown as dashed lines; red for the functional consensus ATPase site, and blue for the degenerate ATPase site. Distance values are indicated in each panel. **c**, Top down views of the extracellular face. Extracellular gate residues are shown as stick representation. Domains follow the color scheme presented in **Figure 1.1A**.

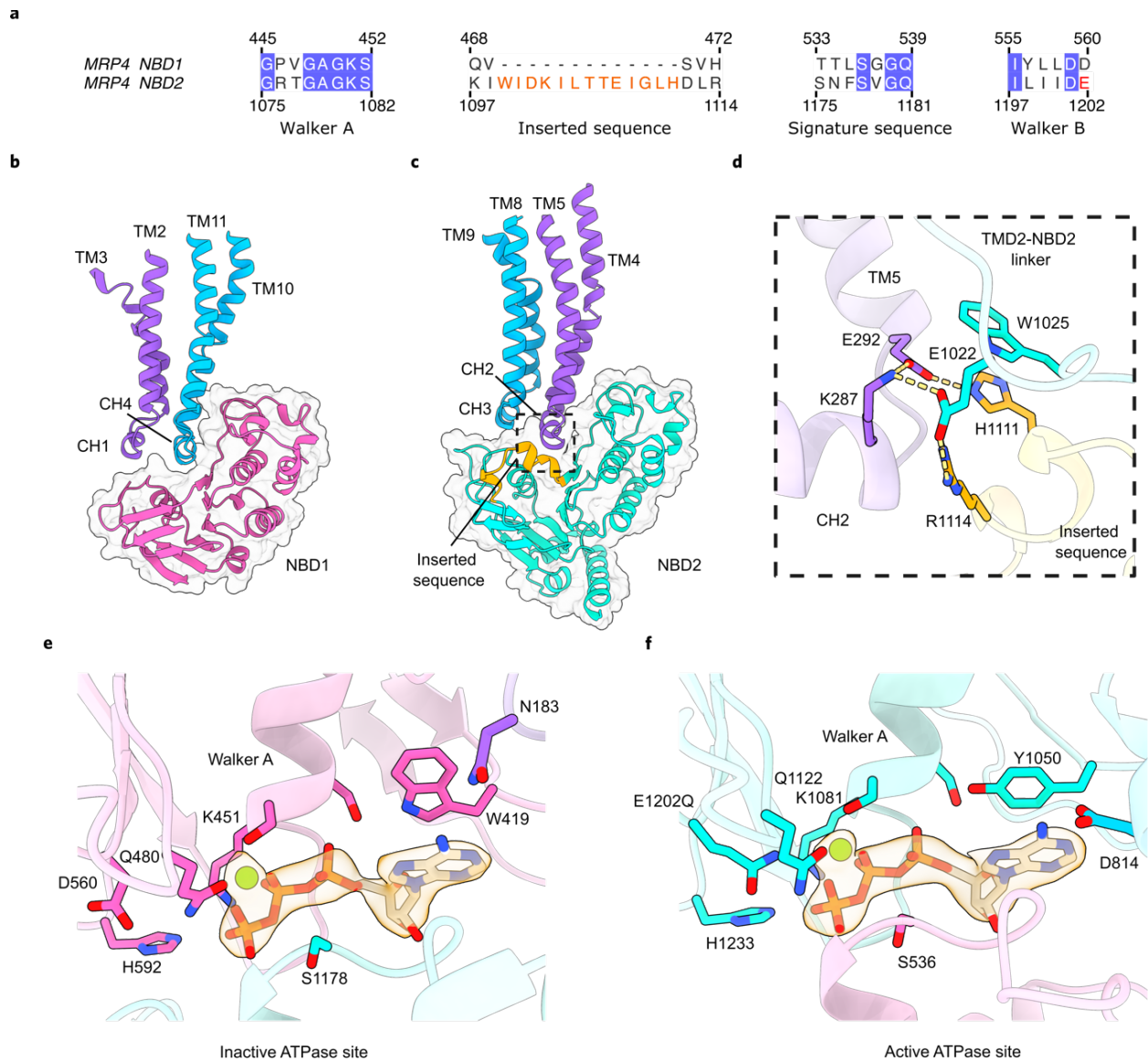


### Figure 1.4 | Structural asymmetry between NBD1 and NBD2

**a**, Sequence alignment of selected motifs from NBD1 and NBD2. Conserved residues are highlighted in blue, residues of the inserted sequence are orange, and the position of E1202Q mutant in NBD2 Walker B is in red. Side view of the TMD interactions with **b**, NBD1 and **c**, NBD2. Ribbon diagram of domains are colored as in **Figure 1.1A**, and are overlaid on a surface of either NBD in transparent grey. The inserted sequence in NBD2 is highlighted in orange. **d**, Enlarged view of the box in **c**. Electrostatic interactions between the inserted sequence, CH2, and the TMD2-NBD2 linker, with residues shown as sticks. Hydrogen bonds and salt bridges are indicated by yellow dashed lines. Close-up views of the **e**, degenerate and **f**, functional ATPase sites in the ATP-Mg<sup>2+</sup>-bound, outward occluded state. Selected side chains from interacting motifs are shown as sticks. ATP is shown as sticks, Mg<sup>2+</sup> as green spheres, and densities for

both are shown as a transparent surface. For clarity, only ATP-Mg<sup>2+</sup> density is shown. Selected electrostatic interactions are shown as yellow dashed lines.



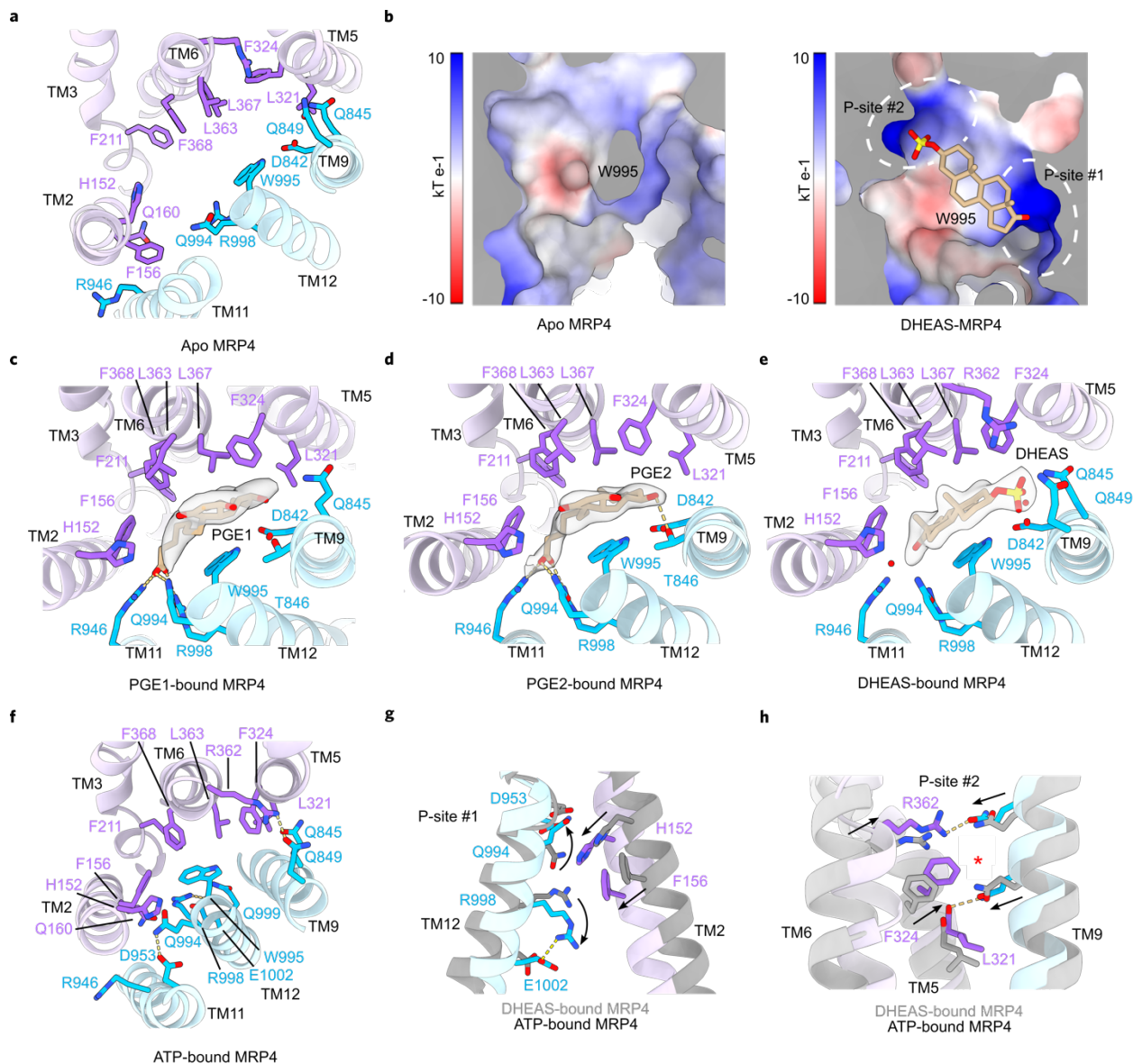


### Figure 1.5 | DHEA-S and prostaglandin binding to MRP4

Top-down view of the substrate binding pocket in **a**, the apo, inward-open state, **c**, the inward-narrow state bound to PGE<sub>1</sub>, **d**, the inward-narrow state bound to PGE<sub>2</sub>, **e**, the inward-narrow state bound to DHEA-S, and **f**, the outward-occluded state of MRP4<sub>E1202Q</sub> bound to ATP-Mg<sup>2+</sup>. Residues shown form van der Waals contacts, hydrogen bonds, or salt bridges with any of the three substrates. Substrates are represented by sticks. For clarity, only substrate densities are shown as transparent surfaces. Waters are depicted as red spheres, and electrostatic interactions are indicated as yellow dashed lines. **b**, Electrostatic potentials of the substrate-binding surfaces of MRP4's TMD2 in the apo, inward open state (left) and the inward-narrow, DHEA-S-bound state (right). Dashed circles highlight P-sites #1 and #2 that assemble upon substrate binding. Local conformational changes at **g**, P-site #1 and **h**, P-site #2 as MRP4 transitions from the inward-narrow, substrate-bound state to the outward-occluded, ATP-Mg<sup>2+</sup>-bound state.

The DHEA-S bound structure is shown in gray and the ATP-Mg<sup>2+</sup>-bound state is colored as in **Figure 1.1A**. Black arrows indicate movement of sidechains. Electrostatic interactions are shown as yellow dashed lines. Red asterisks indicate positions of substrate polar groups in their respective structures (an unoccupied P-site #2 and the C1 carboxyl in P-site #1 in the PGE<sub>1</sub> and PGE<sub>2</sub> bound structures; the 3 $\beta$  sulfate in P-site #2 and a coordinated water in P-site #1 in the DHEA-S bound structure).



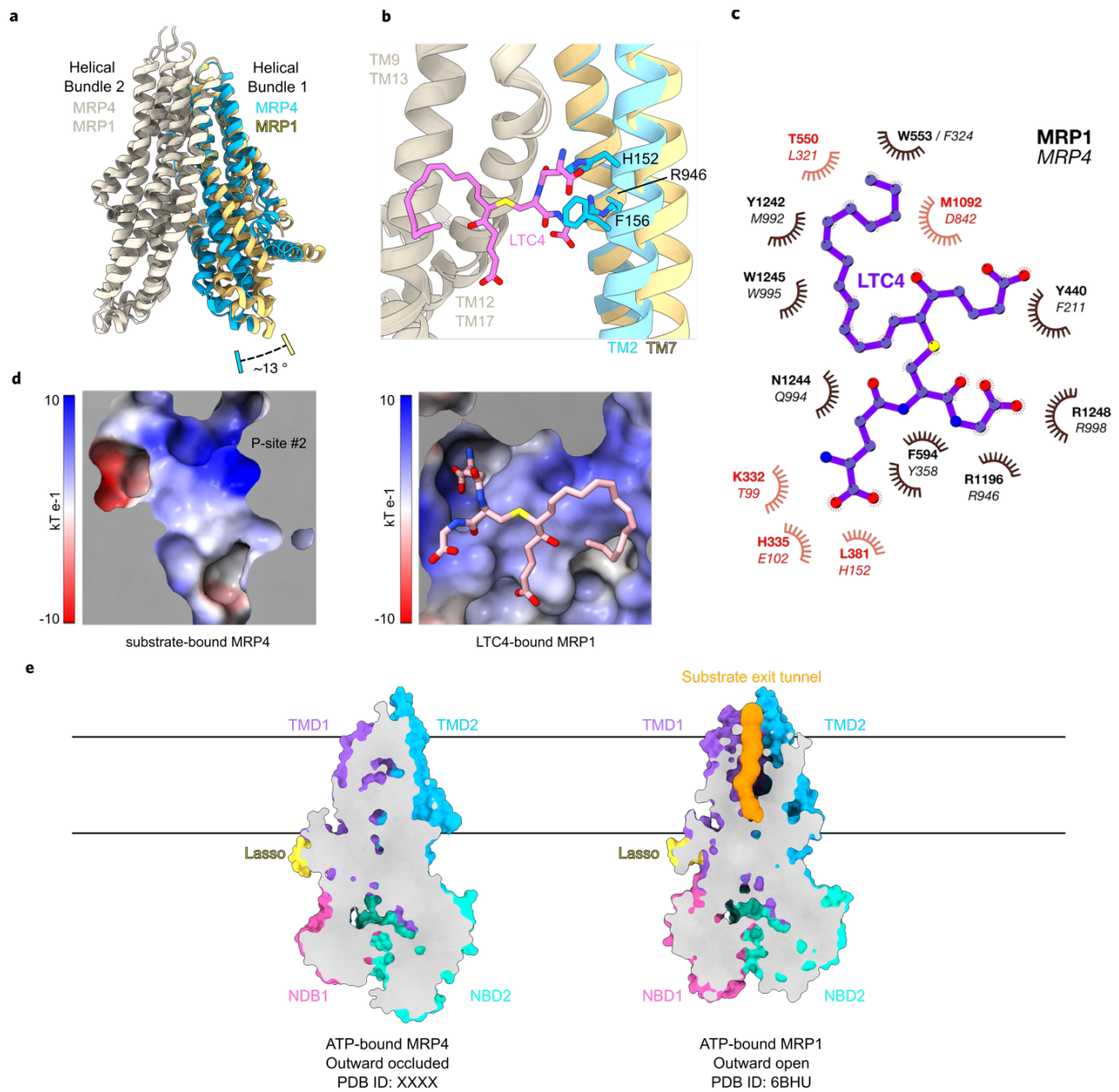


## Figure 1.6 | Structural comparison between MRP4 and related ABCC family members

**a**, Transmembrane domains of MRP1 and MRP4 aligned through helical bundle #2. Helical bundle #2 is colored bone for both transporters. Helical bundle #1 is colored canary in MRP1 and cyan in MRP4. The relative angle of rotation between MRP1's and MRP4's helical bundle 1 with respect to helical bundle 2 is indicated. **b**, Close-up view of the superimposed structures of LTC4-bound MRP1 and DHEAS-bound MRP4 (DHEAS not shown for clarity). LTC4 sterically clashes against H152, F156, and R946 as a result of MRP4's narrower substrate-bound conformation. Transmembrane regions colored as in **a**, LTC4 and MRP4's sidechains shown as sticks. **c**, Schematic of MRP1 bound to LTC4 (PDB:5UJA). MRP1 residues involved in ligand binding are labeled in bold, while

aligned MRP4 residues are noted in italics. Red text signified a change in polarity between MRP1 and corresponding MRP4 residues. **d**, Electrostatic potentials of the aligned substrate-binding surfaces of MRP4's TMD2 bound to DHEA-S (not shown for clarity) (right) and MRP1's TMD2 bound to LTC4. An acidic patch in MRP4 replaces a basic surface for coordinating glutathione carboxyl groups. LTC4 shown as sticks, colored magenta and by heteroatom. **e**, Slice-through of ATP-bound MRP4 and ATP-bound MRP1, reveals a substrate exit tunnel present only in the MRP1 structure, while MRP4 is outward-facing occluded. Transmembrane regions of MRP4 and aligned regions of MRP1 are colored as in **Figure 1.1A**. TMD0 of MRP1 hidden for clarity. The volume of the MRP1 substrate exit tunnel is shown as an orange surface.

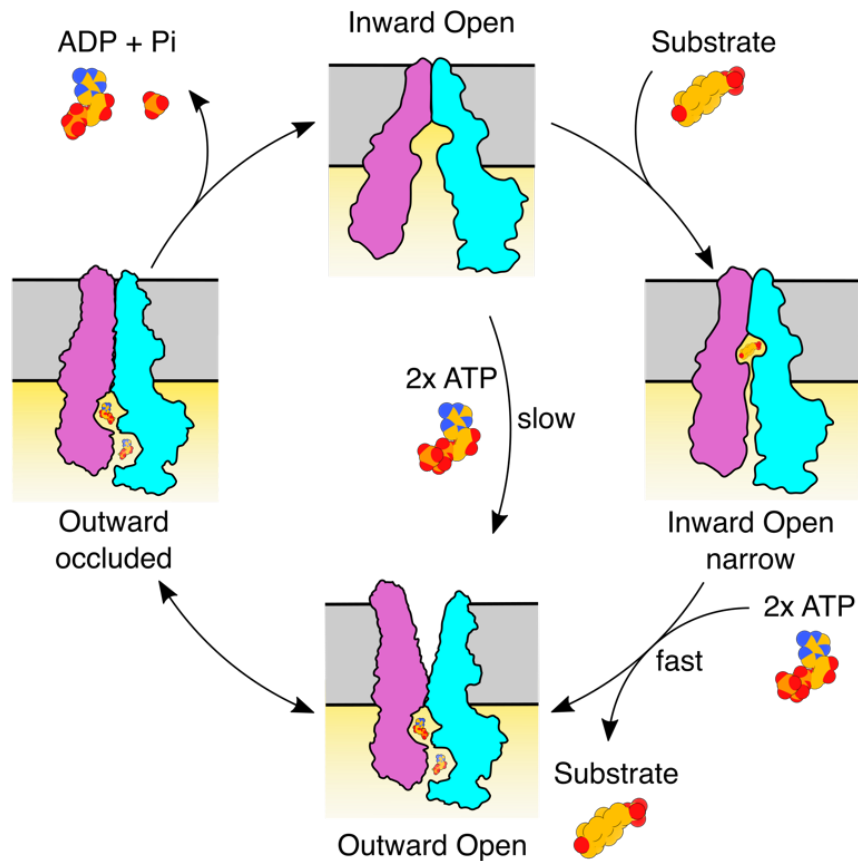


**Figure 1.7 | Proposed translocation cycle of MRP4**

Cartoon representation of the alternate access transport mechanism of MRP4, derived from current cryo-EM structures and the ATP-bound MRP1 structure (PDB ID: 6BHU). The cycle begins with MRP4 open toward the cytoplasm, featuring a solvent-accessible substrate binding cavity and widely separated NBDs. When bound to substrate, the two halves of MRP4 constrict toward one another, reducing the volume of the central cavity and bringing the NBDs into close proximity. ATP binding dimerizes the NBDs and induces substrate transport by allosterically deforming the substrate binding-site and opening the extracellular gate for substrate release. Inward open MRP4 is capable of binding ATP in the absence of substrate and proceeding to this outward open conformation, though at notably slower rate due to the separation in NBDs. In the outward occluded state, thermodynamic fluctuations reset the exit pathway, leaving the substrate binding site exposed to neither the cytoplasm nor extracellular space. ATP hydrolysis and subsequent nucleotide and  $P_i$  release allows for dissociation of the NBD dimer and return to the inward open state. The first half of MRP4 composed of the  $L_0$ , TM bundle 1, and NBD1 shown in magenta, and the second half of MRP4 composed of TM bundle 2 and NBD2 shown in cyan.



and the C-terminal PDZ-binding motif (PDZ-BM, sand). Bovine MRP4 catalytic residue E1202 is highlighted in red.

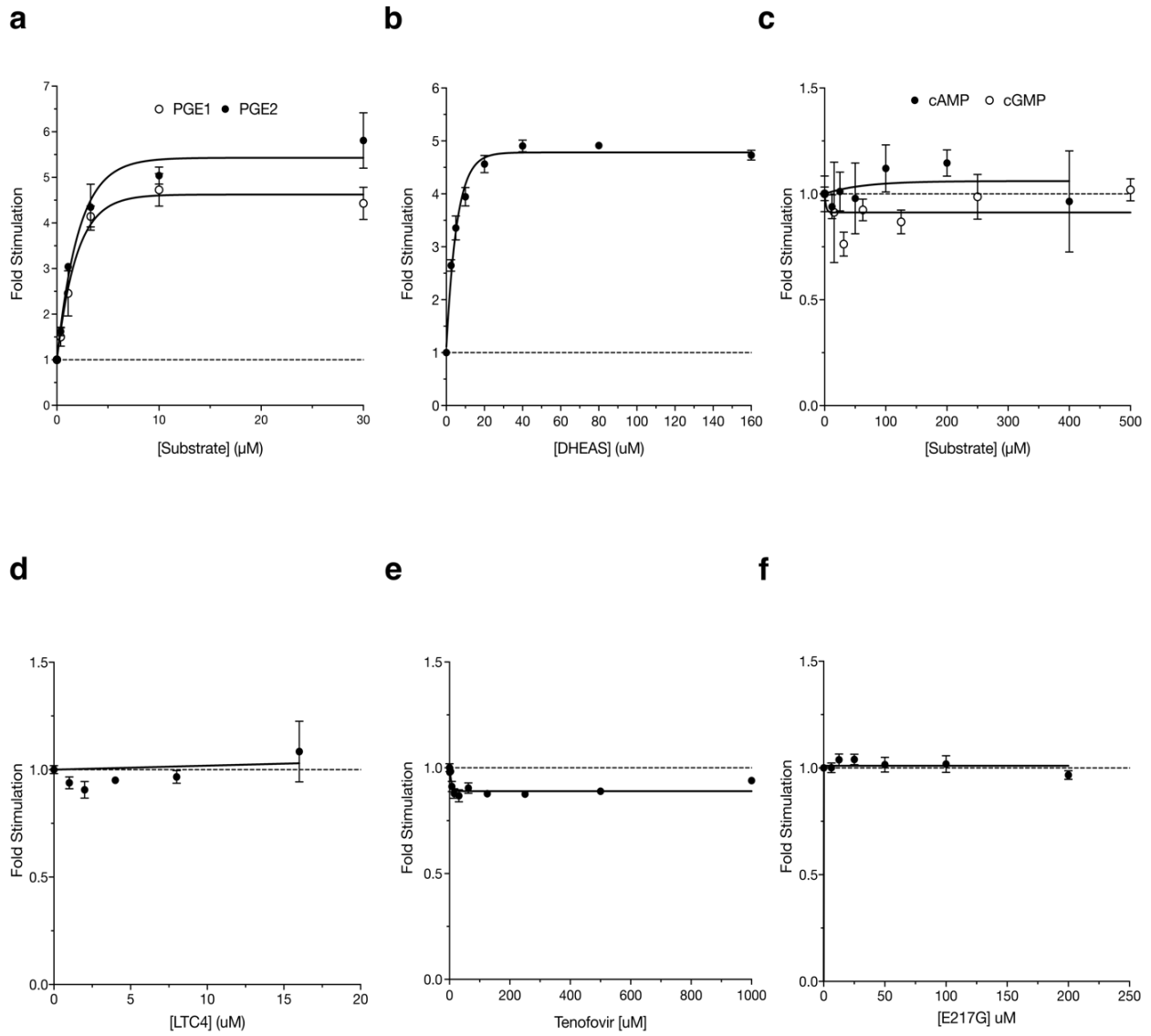
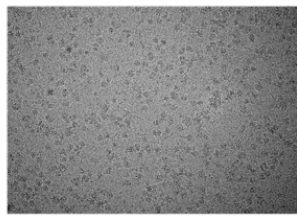


**Figure 1.9 | Biochemical characterization of MRP4**

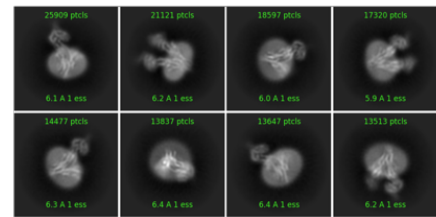
Fold change in ATPase activity relative to basal levels with the addition of increasing concentrations of **a**, PGE<sub>1</sub>, PGE<sub>2</sub>, **b**, DHEAS, **c**, cAMP, cGMP, **d**, LTC<sub>4</sub>, **e**, tenofovir and **f**, E217G. PGE<sub>1</sub>, prostaglandin E<sub>1</sub>; PGE<sub>2</sub>, prostaglandin E<sub>2</sub>; cAMP, cyclic adenosine monophosphate; cGMP, cyclic guanosine monophosphate; LTC<sub>4</sub>, leukotriene C<sub>4</sub>; DHEAS, dehydroepiandrosterone sulfate; E217G,  $\beta$ -estradiol-17 $\beta$ -D-glucuronide.



**a**

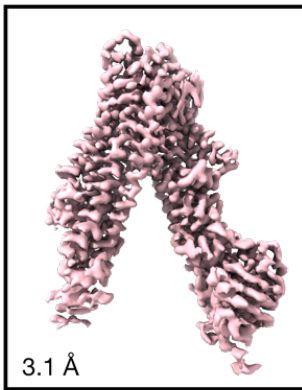


1,448,148 particles  
picked in cisTEM  
extracted in Relion 3.1



4,698 movies  
drift corrected w/ MotionCor2  
CTF estimation w/ CTFIND4

2x rounds of 2D classification  
in cryoSPARC



cryoSPARC *ab initio* reconstruction

(6 classes)

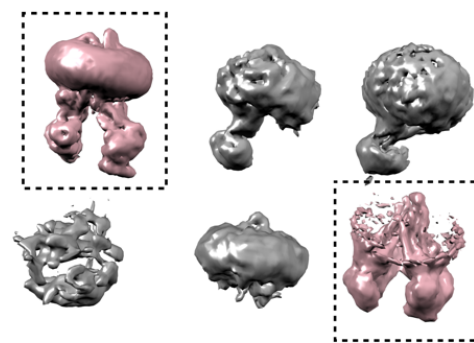
↓ 660,807

cryoSPARC heterogeneous reconstruction

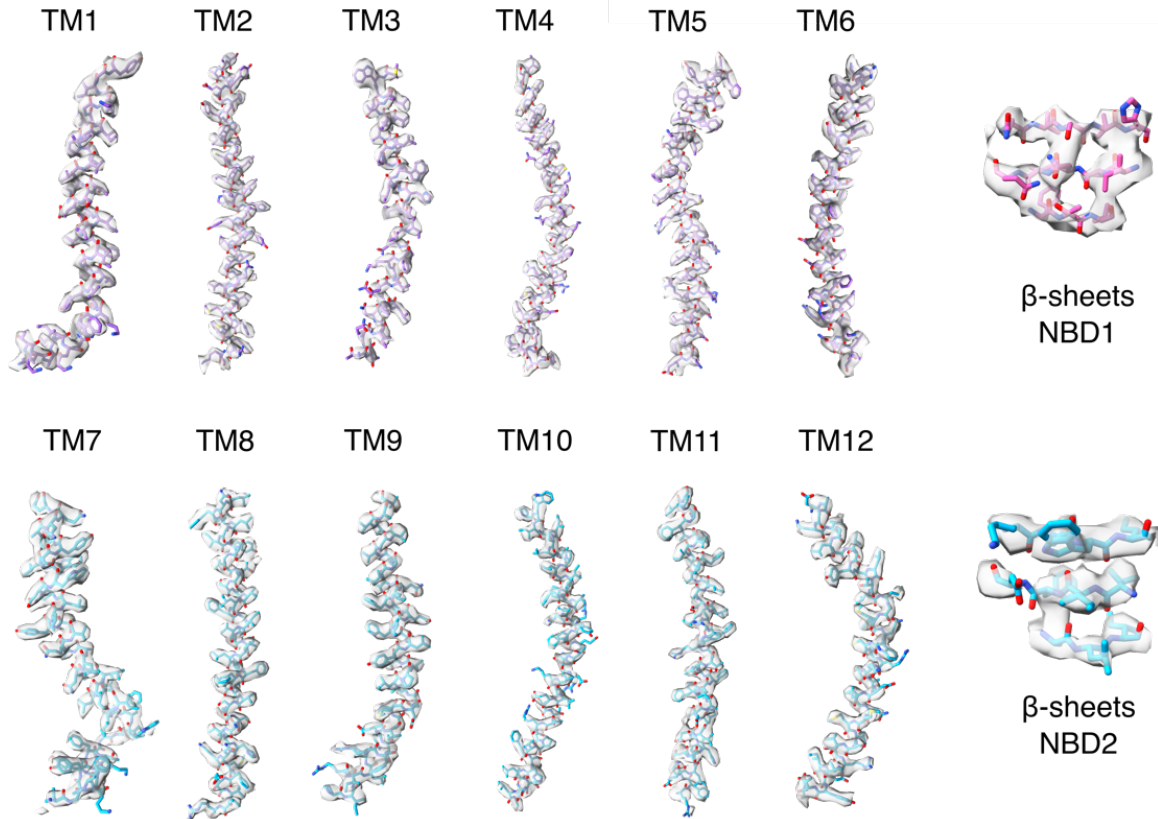
(6 classes)

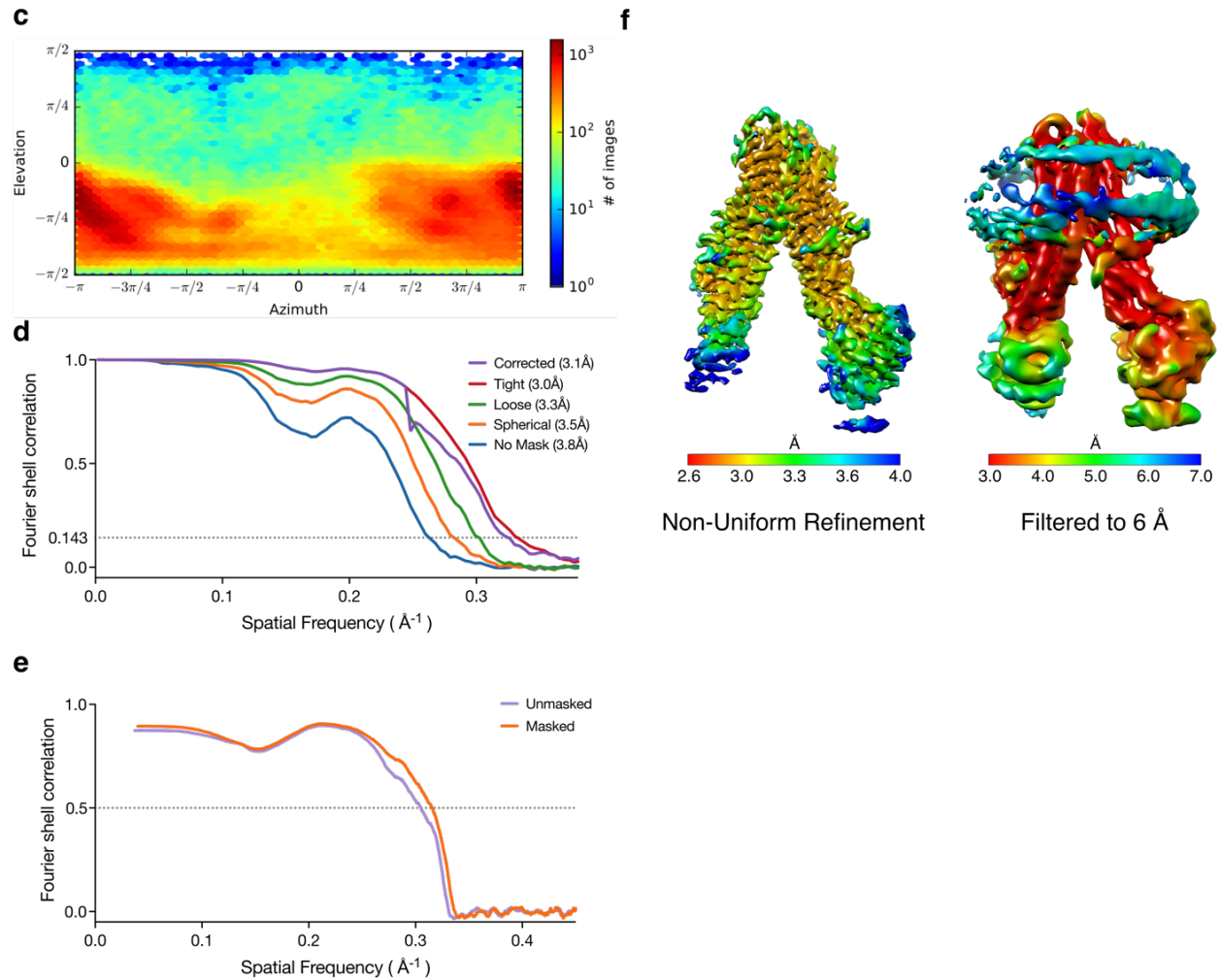


cryoSPARC  
non-uniform refinement  
←  
combine selected classes  
660,807  
particles



**b**

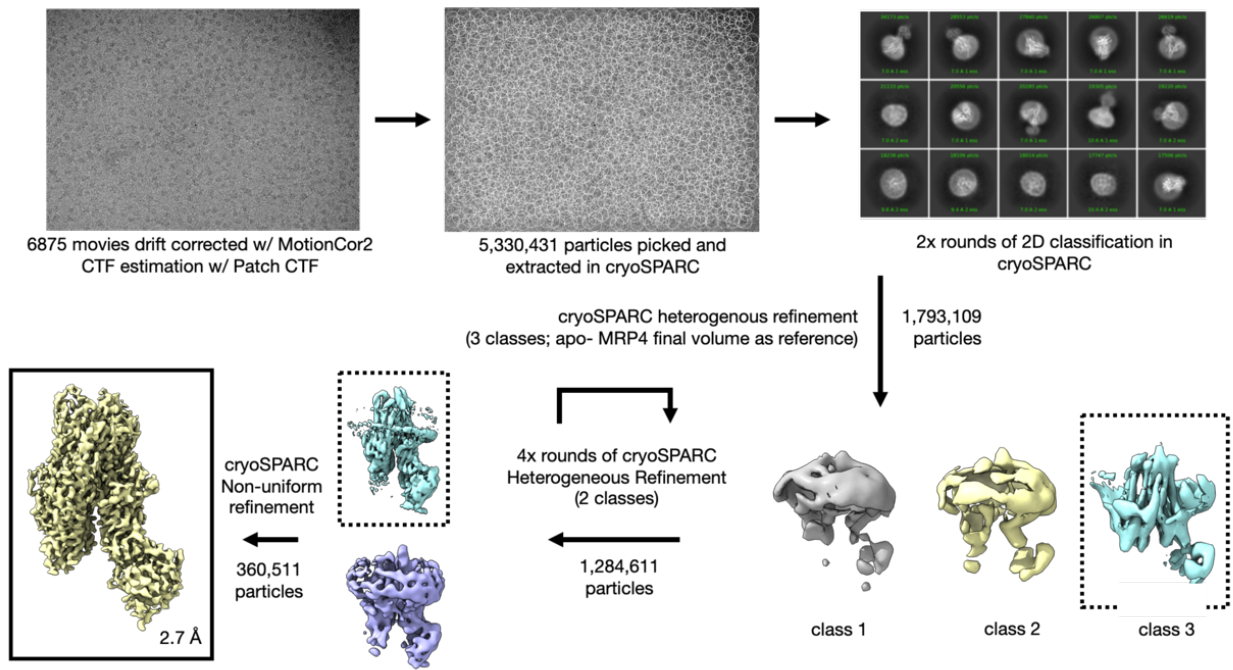
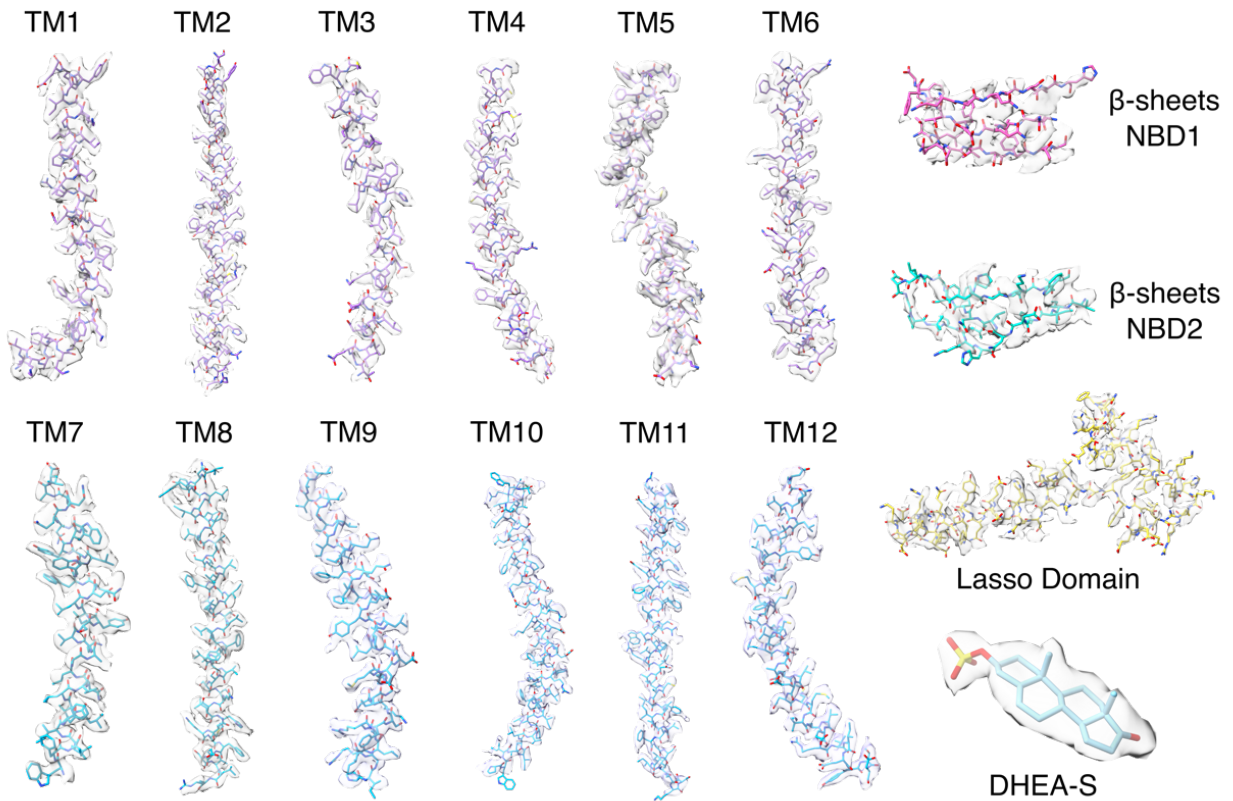


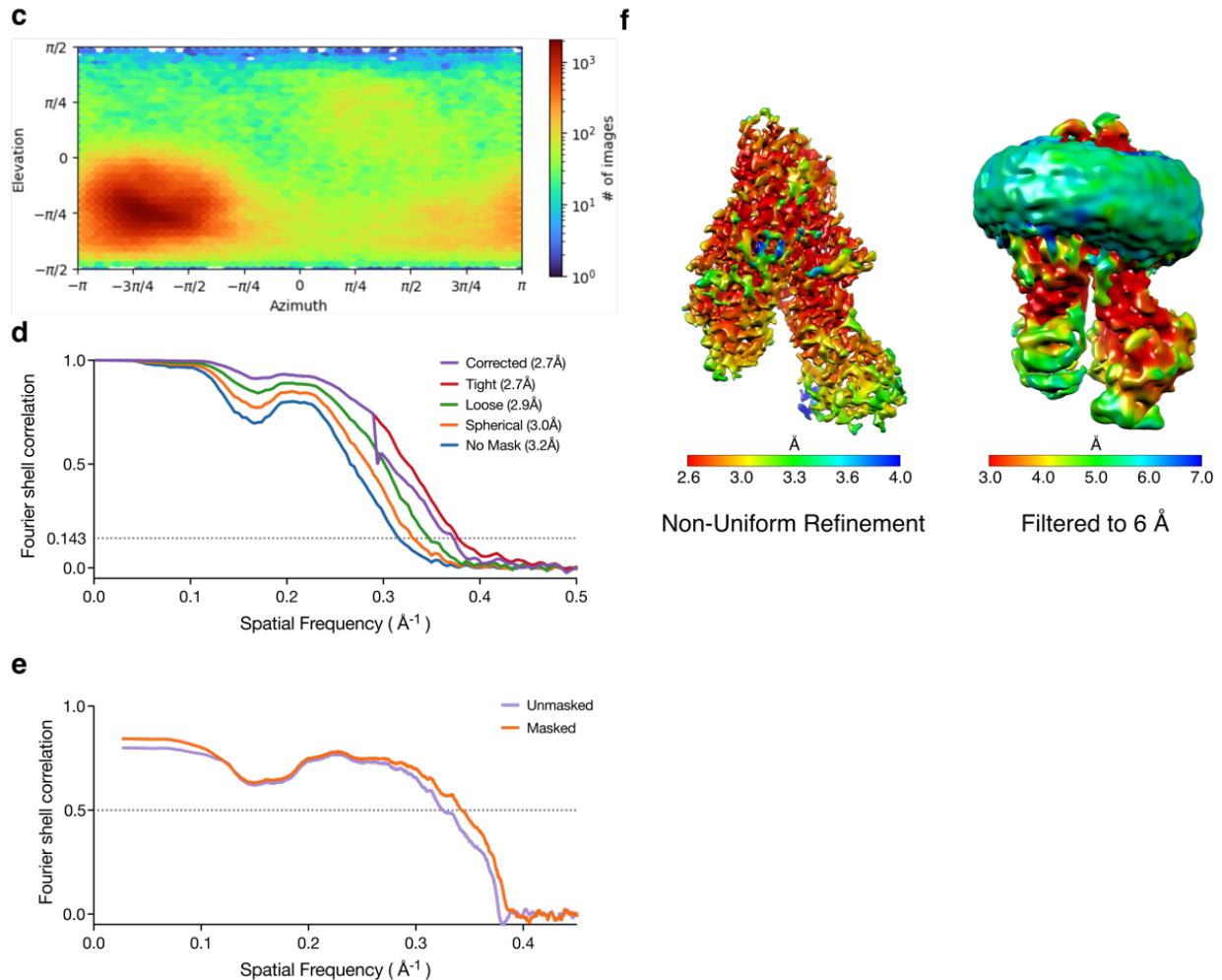


**Figure 1.10 | Image processing of nucleotide-free, substrate-free MRP4 leading to a 3.1 Å cryo-EM reconstruction**

Cryo-EM analysis of apo MRP4 in lipid nanodiscs. **a**, Processing pipeline for apo MRP4. **b**, Cryo-EM density of the sharpened map overlaid with the model from selected regions. **c**, Euler angle heat-maps for the final nucleotide-free MRP4 refinement **d**, Gold-standard Fourier shell correlation threshold from the final nucleotide-free MRP4 refinement. Average resolution determined by using a correlation threshold of 0.143. **e**, Map to model FSC plot indicating correspondence of nucleotide-free MRP4 atomic model to final density map. **f**, Final density from cryoSPARC refinement colored by local resolution. To show lower resolution features, including NBD1, the map is also shown low-pass filtered to 6 Å.

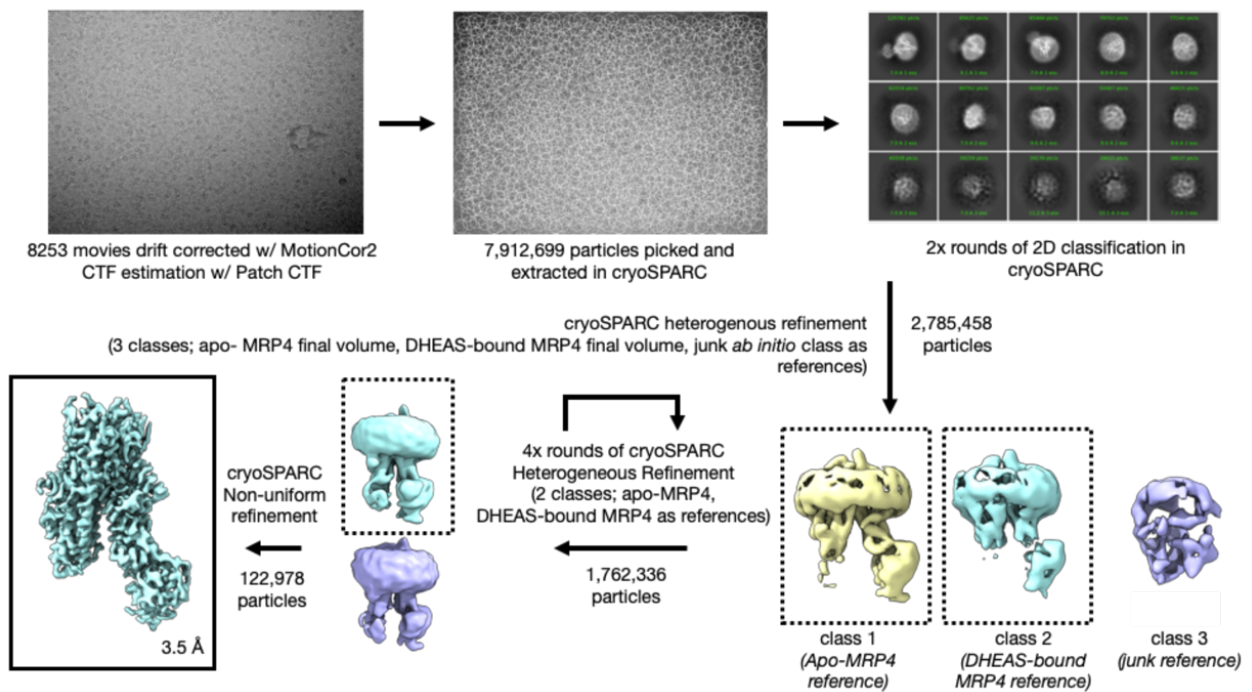
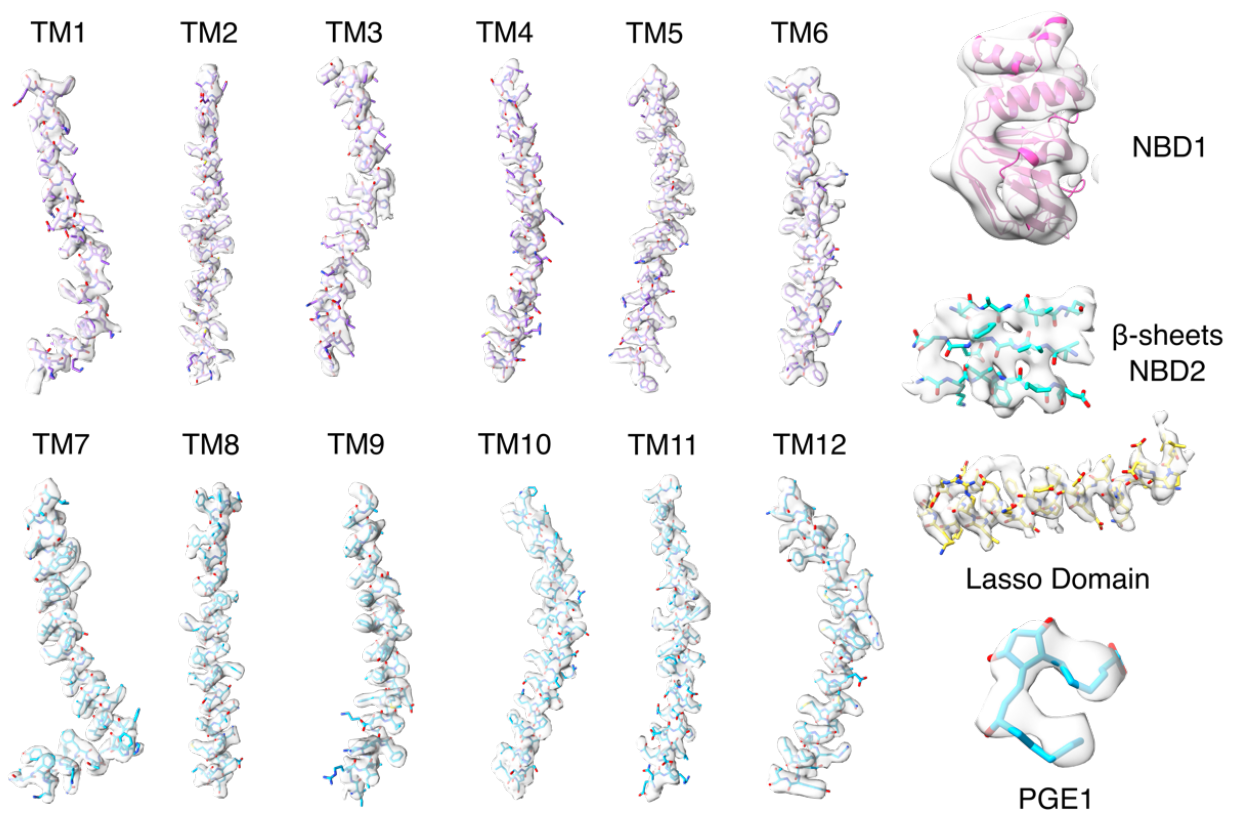


**a****b**



### Figure 1.11 | Image processing of DHEAS-bound MRP4 leading to a 2.7 Å cryo-EM reconstruction

Cryo-EM analysis of DHEAS-bound MRP4 in lipid nanodiscs. **a**, Processing pipeline for DHEAS-bound MRP4. **b**, Cryo-EM density of the sharpened map overlaid with the model from selected regions. **c**, Euler angle heat-maps for the final DHEAS-bound MRP4 refinement **d**, Gold-standard Fourier shell correlation threshold from the final DHEAS-bound MRP4 refinement. Average resolution determined by using a correlation threshold of 0.143. **e**, Map to model FSC plot indicating correspondence of DHEAS-bound MRP4 atomic model to final density map. **f**, Final density from cryoSPARC refinement colored by local resolution. To show lower resolution features, including NBD1, the map is also shown low-pass filtered to 6 Å.

**a****b**

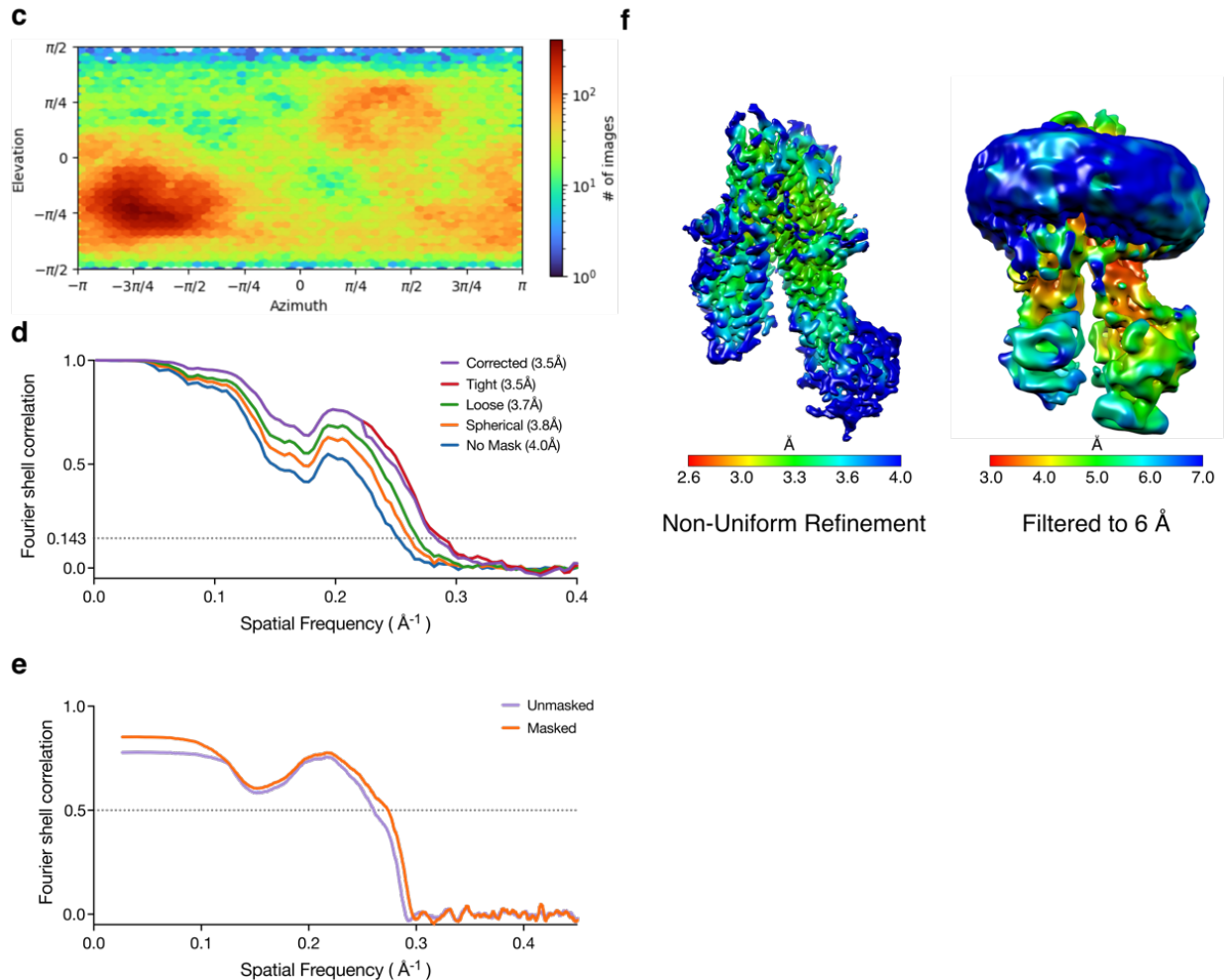
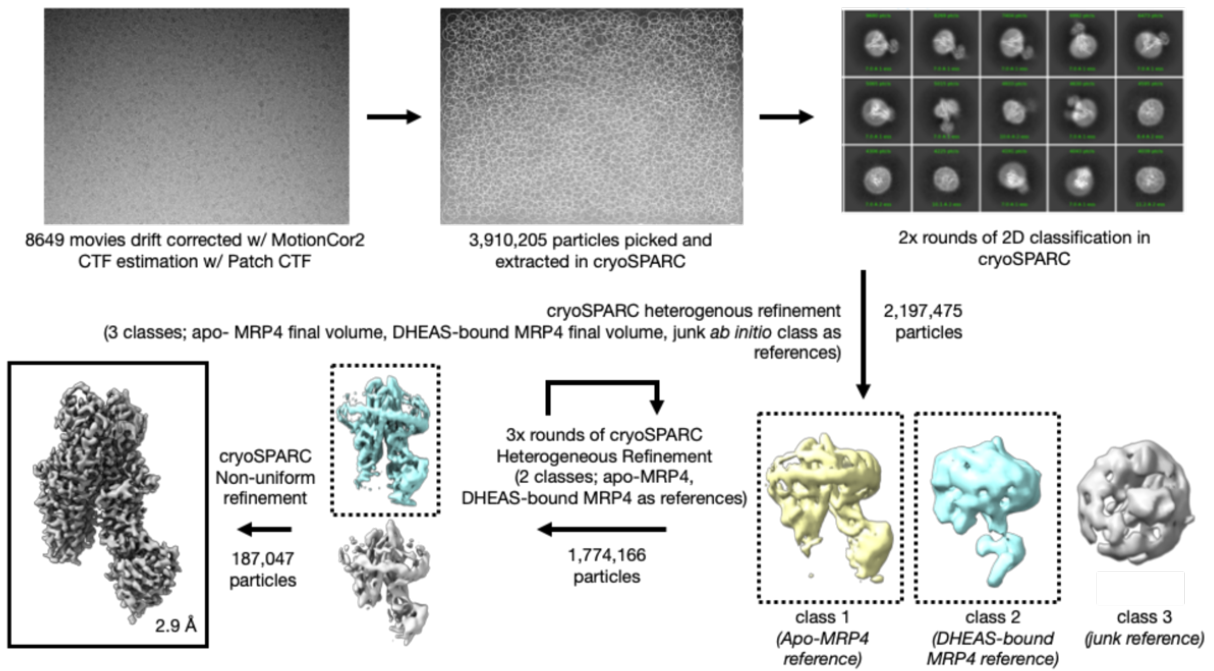


**Figure 1.12 | Image processing of PGE<sub>1</sub>-bound MRP4 leading to a 3.5 Å cryo-EM reconstruction**

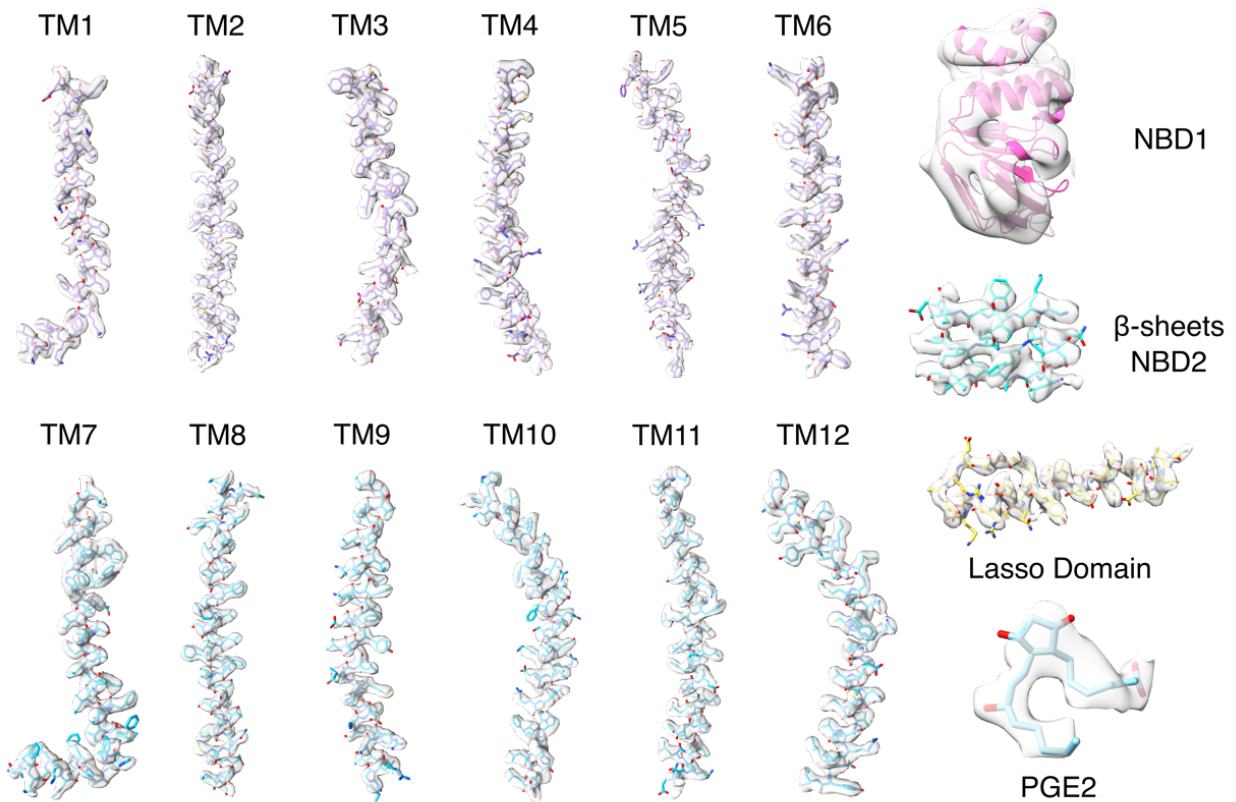
Cryo-EM analysis of PGE<sub>1</sub>-bound MRP4 in lipid nanodiscs. **a**, Processing pipeline for PGE<sub>1</sub>-bound MRP4. **b**, Cryo-EM density of the sharpened map overlaid with the model from selected regions. **c**, Euler angle heat-maps for the final PGE<sub>1</sub>-bound MRP4 refinement **d**, Gold-standard Fourier shell correlation threshold from the final PGE<sub>1</sub>-bound MRP4 refinement. Average resolution determined by using a correlation threshold of 0.143. **e**, Map to model FSC plot indicating correspondence of PGE<sub>1</sub>-bound MRP4 atomic model to final density map. **f**, Final density from cryoSPARC refinement colored by local resolution. To show lower resolution features, including NBD1, the map is also shown low-pass filtered to 6 Å.

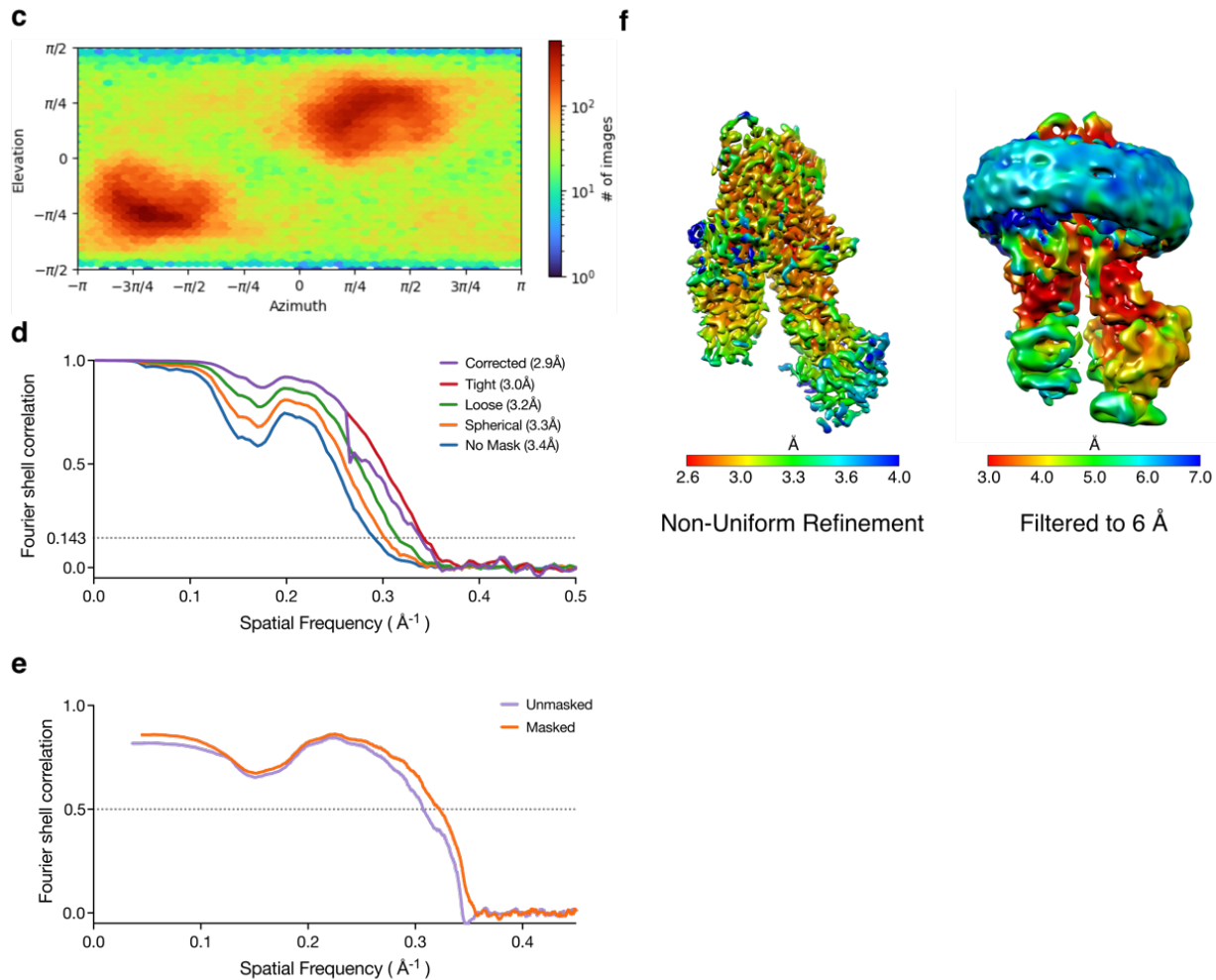


**a**



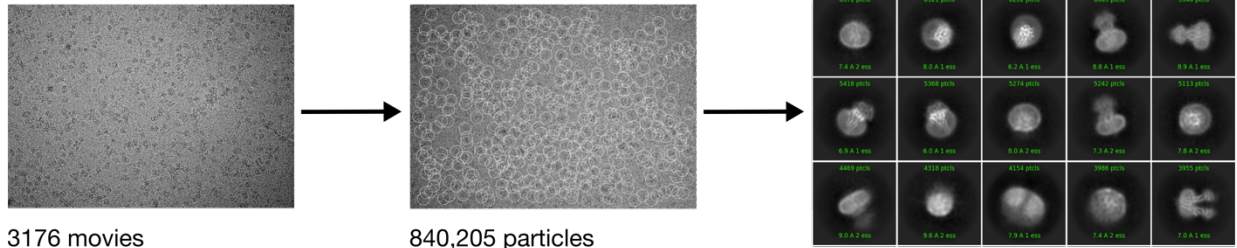
**b**





**Figure 1.13 | Image processing of PGE<sub>2</sub>-bound MRP4 leading to a 2.9 Å cryo-EM reconstruction**

Cryo-EM analysis of PGE<sub>2</sub>-bound MRP4 in lipid nanodiscs. **a**, Processing pipeline for PGE<sub>2</sub>-bound MRP4. **b**, Cryo-EM density of the sharpened map overlaid with the model from selected regions. **c**, Euler angle heat-maps for the final PGE<sub>2</sub>-bound MRP4 refinement **d**, Gold-standard Fourier shell correlation threshold from the final PGE<sub>2</sub>-bound MRP4 refinement. Average resolution determined by using a correlation threshold of 0.143. **e**, Map to model FSC plot indicating correspondence of PGE<sub>2</sub>-bound MRP4 atomic model to final density map. **f**, Final density from cryoSPARC refinement colored by local resolution. To show lower resolution features, including NBD1, the map is also shown low-pass filtered to 6 Å.

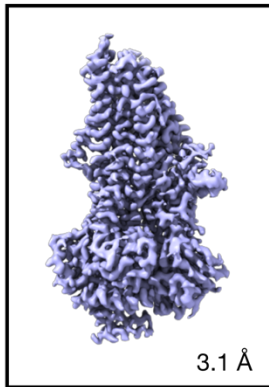
**a**

3176 movies  
drift corrected w/ MotionCor2  
CTF estimation w/ CTFFIND4

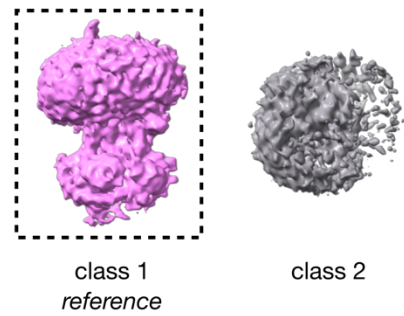
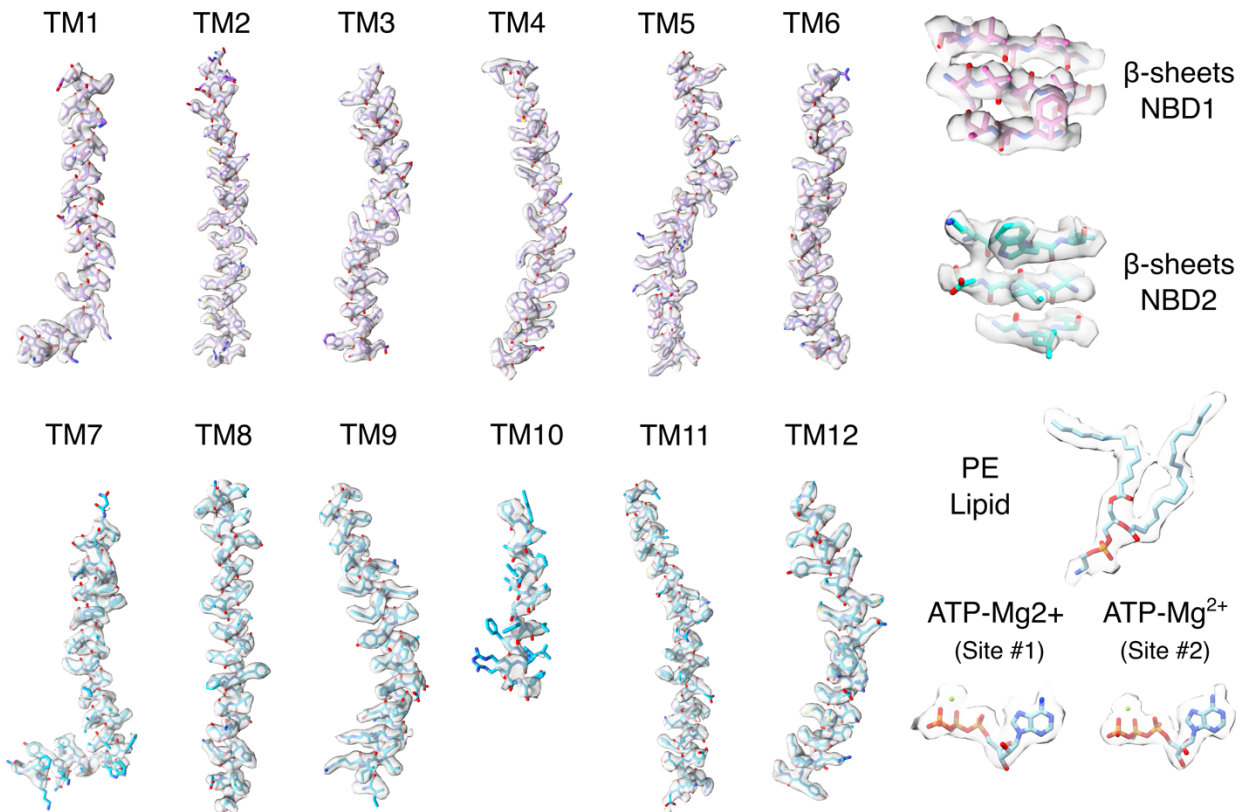
840,205 particles  
picked in cisTEM  
extracted in cryoSPARC

3x rounds of 2D classification  
in cryoSPARC

261,609 particles  
cryoSPARC *ab initio* reconstruction  
(2 classes)



iterative rounds of cryoSPARC  
heterogenous refinement /  
non-uniform refinement  
←←←←←  
104,051  
particles

**b**

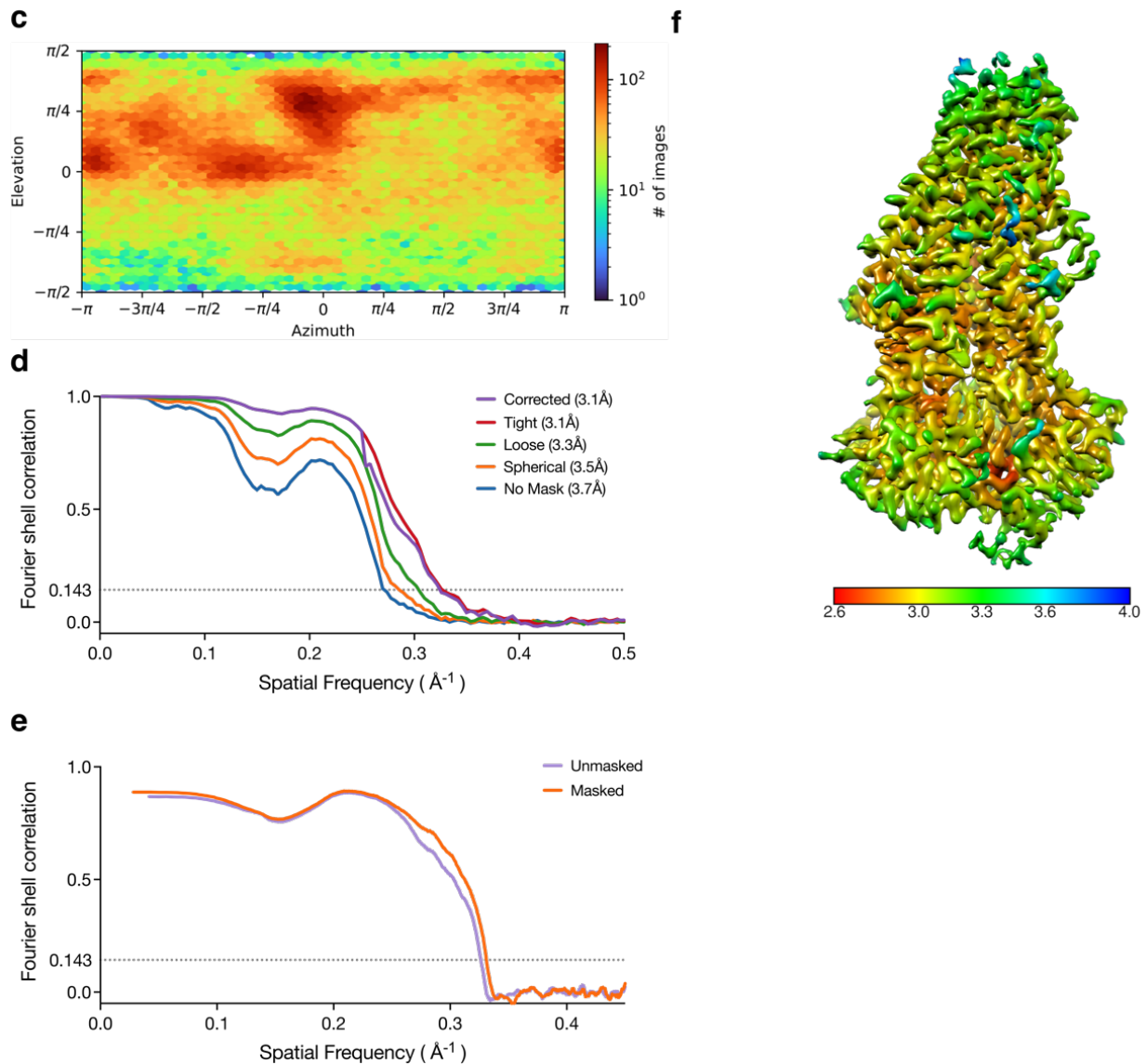


### Figure 1.14 | Image processing of ATP-bound MRP4<sub>E1202Q</sub> leading to a 3.1 Å cryo-EM reconstruction

Cryo-EM analysis of ATP-bound MRP4 in lipid nanodiscs. **a**, Processing pipeline for ATP-bound MRP4<sub>E1202Q</sub>. **b**, Cryo-EM density of the sharpened map overlaid with the model from selected regions. **c**, Euler angle heat-maps for the final ATP-bound MRP4 refinement. **d**, Gold-standard Fourier shell correlation threshold from the final ATP-bound MRP4<sub>E1202Q</sub> refinement. Average resolution determined by using a correlation threshold of 0.143. **e**, Map to model FSC plot indicating correspondence of ATP-bound MRP4<sub>E1202Q</sub> atomic model to final density map. **f**, Final density from cryoSPARC refinement colored by local resolution.



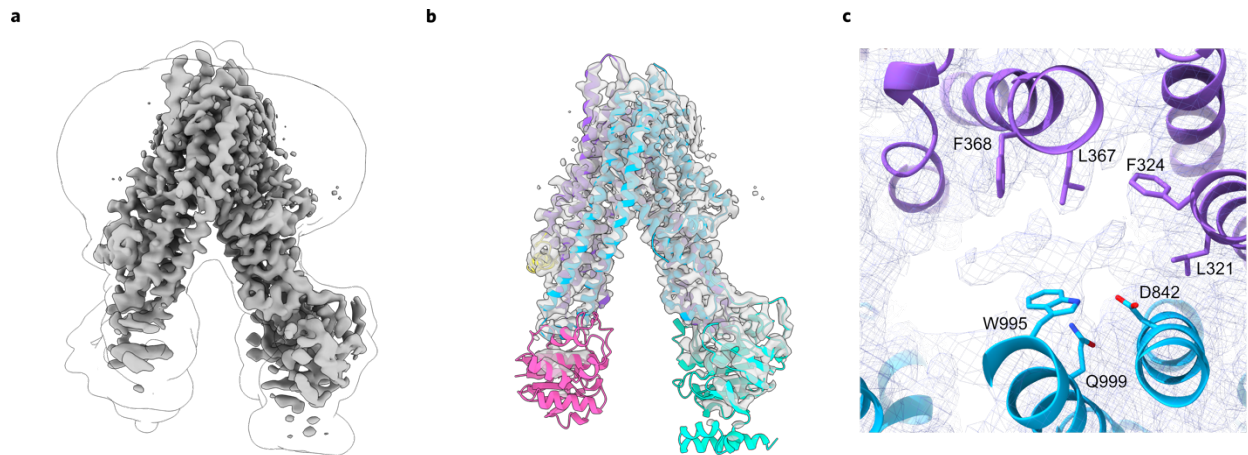


**Figure 1.15 | cAMP does not elicit a conformational change in MRP4**

**a** Final density of MRP4 in the presence of 1mM cAMP from cryoSPARC. Sharpened output volume in grey, lowpass filtered volume showing the nanodisc and NBDs as black silhouette. **b** Rigid body fitting of apo MRP4 into density obtained in the presence of 1mM cAMP. Density in grey, MRP4 domains colored as before. **c** View of substrate binding residues of the rigid-body fit apo MRP4 model in the density obtained for MRP4 in the presence of 1mM cAMP. Map contoured at low threshold, revealing non-protein density similar to our apo MRP4 refinement. Density in purple mesh, MRP4 domains colored as before.

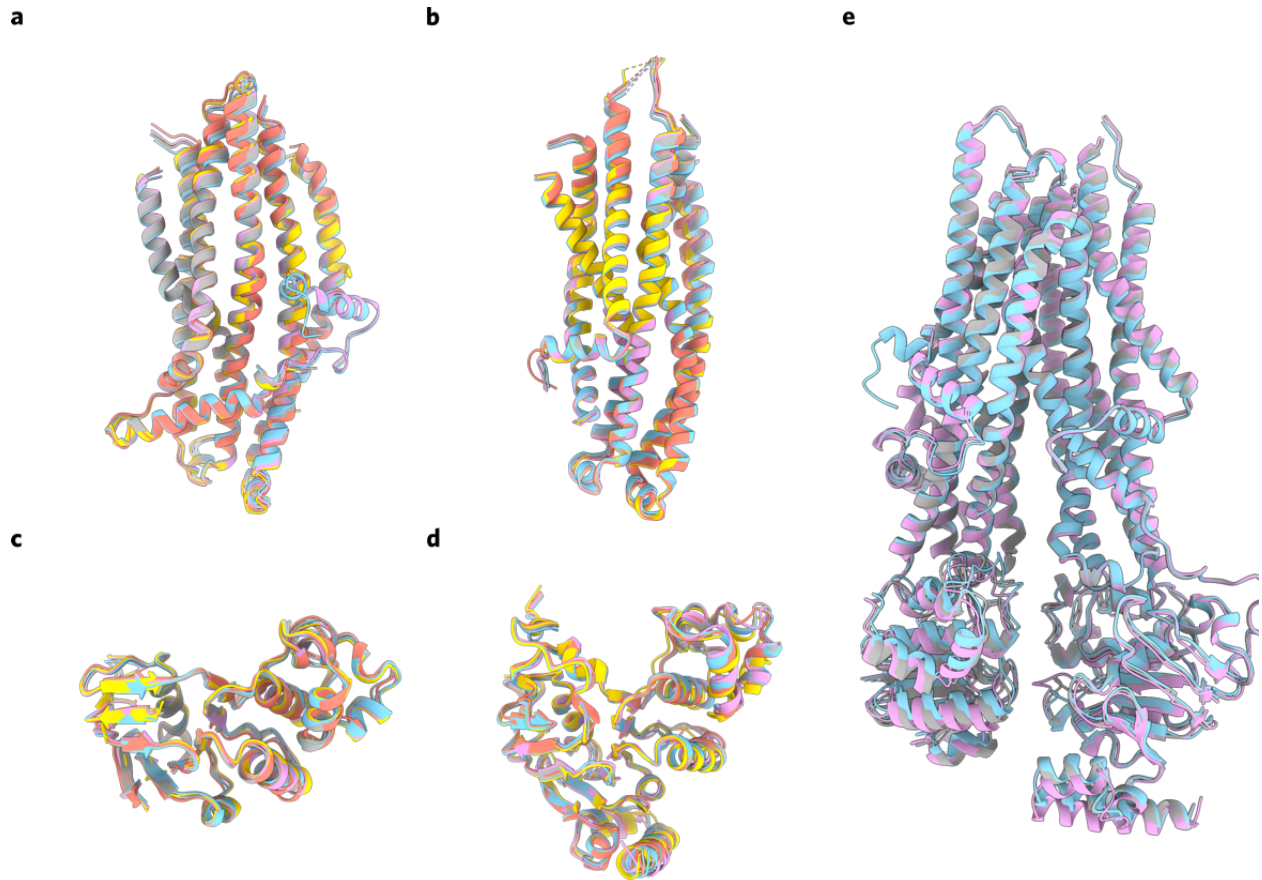


**Figure 1.16 | The domains of MRP4 move as rigid bodies throughout the substrate transport cycle**

Superposition of **a**, bundle 1 (TMs 1, 2, 3, 6, 10, 11) **b**, bundle 2 (TMs 4, 5, 7, 8, 9, 12) **c**, NBD1 and **d**, NBD2 across all five structures. Apo MRP4 in salmon, DHEA-S-bound MRP4 in cyan, PGE<sub>1</sub>-bound MRP4 in grey, PGE<sub>2</sub>-bound MRP4 in pink, ATP-Mg<sup>2+</sup>-bound MRP4 in yellow. **e**, Superposition of the three substrate-bound structures reveals them to share an inward open, narrow conformation. RMSD between all C $\alpha$  of DHEA-S-bound MRP4 and PGE<sub>1</sub>-bound MRP4 is 1.2 Å; between DHEA-S-bound and PGE<sub>2</sub>-bound is 0.87 Å; between PGE<sub>1</sub>-bound and PGE<sub>2</sub>-bound is 0.90 Å. Structures are colored as in **a-d**.

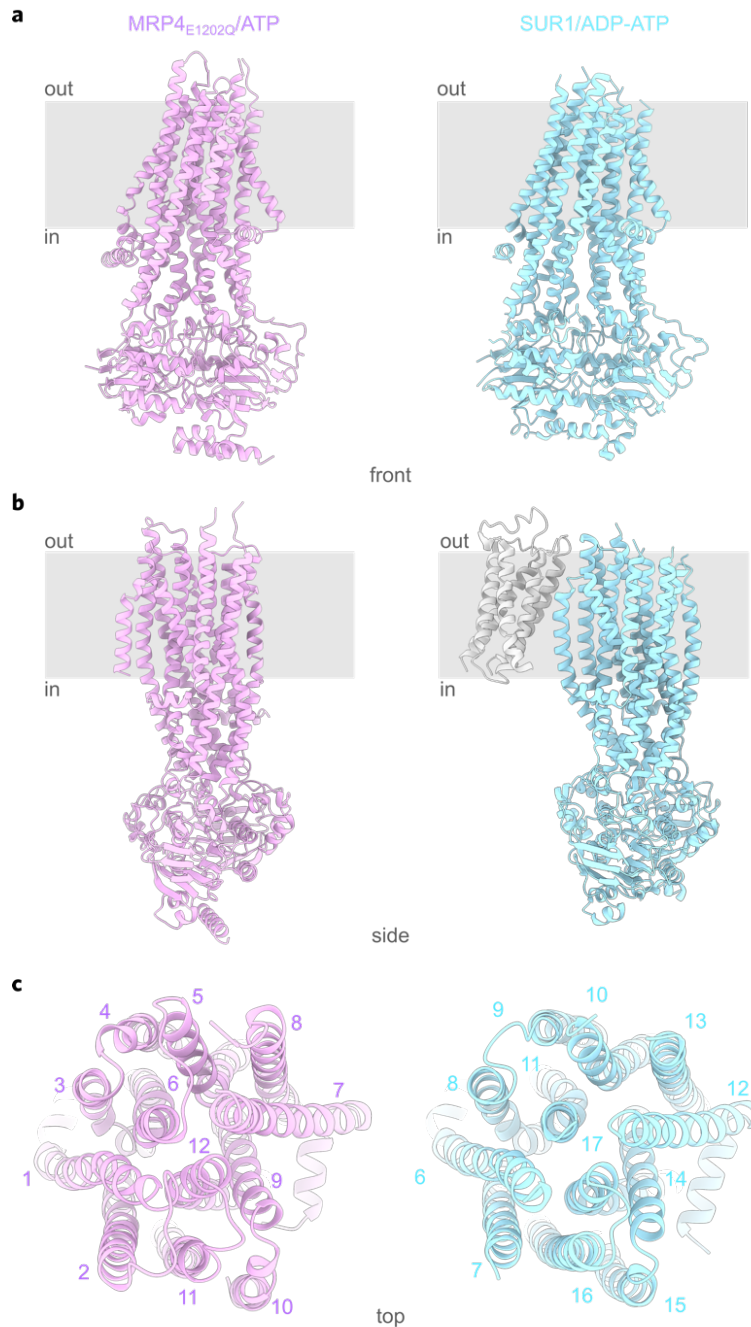


**Figure 1.17 | The outward-facing occluded state of MRP4 closely resembles the structure of SUR1 bound to ADP/ATP**

**a** Front view, **b** side view, and **c** top view of MRP4<sub>E1202Q</sub> bound to ATP-Mg<sup>2+</sup> and SUR1 bound to ADP-ATP (shown as single chain from PDBID:6C3O). TMD<sub>0</sub> domain in SUR1 is hidden for clarity in **a** and **c**. C $\alpha$  RMSD between our ATP-bound structure and SUR1 with TMD<sub>0</sub> domain deleted is 4.36 Å. MRP4<sub>E1202Q</sub> bound to ATP-Mg<sup>2+</sup> in pink, SUR1 bound to ADP-ATP in cyan, TMD<sub>0</sub> domain in light grey.

## Tables

**Table 1.1 | Cryo-EM data collection, refinement, and validation statistics**

	<b>apo MRP4</b> (EMD-XXXXX) (PDB XXXX)	<b>MRP4 + DHEAS</b> (EMD-XXXXX) (PDB XXXX)	<b>MRP4 + PGE<sub>1</sub></b> (EMD-XXXXX) (PDB XXXX)	<b>MRP4 + PGE<sub>2</sub></b> (EMD-XXXXX) (PDB XXXX)	<b>MRP4 + ATP-Mg<sup>2+</sup></b> (EMD-XXXXX) (PDB XXXX)
<b>Data collection and processing</b>					
Microscope	Titan Krios G3	Titan Krios G3	Titan Krios G3	Titan Krios G3	Titan Krios G3
Imaging System	K3 BioQuantum, 20 eV slit	K3 BioQuantum, 20 eV slit	K3 BioQuantum, 20 eV slit	K3 BioQuantum, 20 eV slit	K3 BioQuantum, 20 eV slit
Voltage (kV)	300	300	300	300	300
Electron exposure (e <sup>-</sup> /Å <sup>2</sup> )	67	67	67	67	67
Exposure time (s)	5.9	5.9	5.9	5.9	5.9
Underfocus range (μm)	-1.0 to -2.0	-0.5 to -2.0	-0.5 to -2.0	-0.5 to -2.0	-0.5 to -2.0
Pixel size (super- resolution)	0.4175 Å pix <sup>-1</sup>	0.4175 Å pix <sup>-1</sup>	0.4175 Å pix <sup>-1</sup>	0.4175 Å pix <sup>-1</sup>	0.4175 Å pix <sup>-1</sup>
Frames per movie	117	117	117	117	117
Movies collected	4698	5609	7219	8649	3176
Acquisition software	SerialEM	SerialEM	SerialEM	SerialEM	SerialEM
Symmetry imposed	C1	C1	C1	C1	C1
Initial particle images (no.)	1,448,148	5,330,431	7,912,699	3,910,205	840,205
Final particle images (no.)	660,807	360,511	122,978	187,047	104,051
Map resolution (Å)	3.1	2.7	3.5	2.9	3.1
FSC threshold	0.143	0.143	0.143	0.143	0.143
<b>Refinement</b>					
Model resolution (Å)					
Masked	3.2	2.9	3.6	3.1	3.2
Unmasked	3.3	3.0	3.8	3.2	3.3
FSC threshold	0.5	0.5	0.5	0.5	0.5
Model composition					
No. Atoms (non- hydrogen)	9109	9521	9418	9202	9155
No. Residues	1144	1188	1175	1152	1135
No. Water	0	3	1	1	0
No. Ligands	0	XH0: 1	XPG: 1	P2E: 1	MG: 2 ATP: 2 PTY: 1
<i>B</i> factors (Å <sup>2</sup> ) min/max/mean					
Protein	37.02/230.10/125.69	1.73/190.69/85.26	34.87/204.17/100.34	7.57/190.27/89.80	101.57/273.17/150.35
Ligand	---	10.47/41.83/24.62	46.19/46.19/46.19	37.95/55.85/44.75	142.09/187.07/157.54
Water	---	28.76/36.26/32.62	41.80/41.80/41.80	33.33/33.33/33.33	---
R.m.s. deviations					
Bond lengths (Å) (# > 4σ)	0.006 (0)	0.004 (0)	0.005 (0)	0.006 (1)	0.005 (1)
Bond angles (°) (# > 4σ)	0.687 (6)	0.674 (0)	0.831 (0)	0.898 (3)	0.876 (2)

	apo MRP4 (EMD-XXXXX) (PDB XXXX)	MRP4 + DHEAS (EMD-XXXXX) (PDB XXXX)	MRP4 + PGE <sub>1</sub> (EMD-XXXXX) (PDB XXXX)	MRP4 + PGE <sub>2</sub> (EMD-XXXXX) (PDB XXXX)	MRP4 + ATP-Mg <sup>2+</sup> (EMD-XXXXX) (PDB XXXX)
<b>Validation</b>					
MolProbity score	1.61	1.12	0.78	0.77	0.65
Clashscore	6.77	2.34	0.94	0.64	0.43
Ramachandran plot					
Favored (%)	96.47	97.46	98.03	97.73	98.67
Allowed (%)	3.53	2.54	1.97	2.27	1.33
Outliers (%)	0.00	0.00	0.00	0.00	0.00
Rama Z-score (RMSD)					
Whole	(N=1134) -1.93 (0.22)	(N=1180) -1.48 (0.21)	(N=1167) -0.82 (0.21)	(N=1144) -0.13 (0.23)	(N=1125) -0.80 (0.22)
Helix	(N=759) -1.23 (0.17)	(N=764) -1.18 (0.16)	(N=767) -1.46 (0.15)	(N=744) -0.28 (0.17)	(N=745) -0.74 (0.16)
Sheet	(N=47) 0.82 (0.71)	(N=51) 0.38 (0.63)	(N=73) -0.49 (0.49)	(N=73) 0.59 (0.58)	(N=83) 0.35 (0.53)
Loop	(N=328) -1.27 (0.31)	(N=365) -0.26 (0.30)	(N=327) -0.40 (0.32)	(N=327) 0.72 (0.36)	(N=297) 0.37 (0.35)

**Table 1.2 | Kinetic parameters for ATPase activity of MRP4**

ATPase activity in the presence of increasing concentrations of the indicated compounds was fit to a Michaelis-Menten equation. The kinetic parameters are mean values from at least three replicate experiments with 95% confidence intervals (CI). NA, not applicable.

<b>Condition</b>	<b>Km (<math>\mu</math>M) (95% CI)</b>	<b>Vmax (nmol min<sup>-1</sup> mg<sup>-1</sup>) (95% CI)</b>	<b>Maximal Fold Change</b>
MRP4 + PGE <sub>1</sub>	1.37 (0.84-2.28)	57.76 (49.38-66.16)	4.14
MRP4 + PGE <sub>2</sub>	1.68 (1.15-2.52)	57.97 (52.27-63.70)	5.05
MRP4 + DHEAS	2.32 (1.60-3.2)	113.1 (106.6-119.9)	4.78
MRP4 + LTC <sub>4</sub>	NA	NA	1.01
MRP4 + E217G	NA	NA	1.01
MRP4 + cAMP	NA	NA	1.07
MRP4 + cGMP	NA	NA	0.95

## Methods

### MRP4 expression and membrane preparation

The wild-type bovine MRP4 gene and the MRP4<sub>E1202Q</sub> mutant were synthesized by Genscript and cloned into pFastBac with a C-terminal thrombin-cleavable 8xHis tag. For all constructs, recombinant baculovirus was produced using the Bac-to-Bac Baculovirus Expression System (Thermo Fisher Scientific). High-titer ( $>10^9$  viral particles/mL) P<sub>3</sub> virus was used to infect *Spodoptera frugiperda* (*Sf9*) cells at a cell density of  $3 \times 10^6$  cells mL<sup>-1</sup>. Cells were harvested 48 hours post infection by centrifugation at 2000 *g*, flash frozen and stored at -80°C until use. Frozen cell pellets were thawed and resuspended in lysis buffer, 50 mM Tris (pH 8.0), 300 mM NaCl, 1 mM TCEP, 1 mM phenylmethylsulfonyl fluoride (PMSF), and EDTA-free cOmplete protease inhibitor cocktail tablets (Sigma-Aldrich). The resuspended cells were repeatedly homogenized with a Dounce homogenizer, then sonicated on ice at 1 s<sup>-1</sup> for 5 minutes. Membranes were spun down at 100,000 *g* for 90 minutes, then resuspended in working buffer (50 mM Tris (pH 8.0), 200 mM NaCl, 1 mM TCEP), supplemented with 1 mM PMSF, with EDTA-free cOmplete protease inhibitor cocktail, and flash frozen in aliquots for future use.

### MRP4 nanodisc reconstitution

Thawed membranes were solubilized with 1% (w/v) *n*-dodecyl- $\beta$ -D-maltopyranoside (DDM, Anatrace) added at a detergent to protein ratio of 0.2 (w/w) and stirred for 4 h. The supernatant was separated from insoluble fractions by centrifugation at 100,000 *g* for 30 minutes and clarified through a 0.22  $\mu$ m filter. After adding 5 mM

imidazole, the supernatant was batch bound to TALON IMAC resin (Clontech) for 2 h at 4°C. The resin was washed with 10 column volumes of working buffer supplemented with 10 mM imidazole and 0.05% DDM, and then returned to working buffer supplemented with 5 mM imidazole and 0.05% DDM. Resuspended resin with bound MRP4 was mixed with Soybean Polar Lipid Extract (Avanti) to a final estimated lipid concentration of 1.2 mM and mixed for 1 h at room temperature. Purified MSPE3D1 was added to the mixture at a final concentration of 0.6 mg ml<sup>-1</sup> and mixed for 1 h at room temperature. Finally, 60 mg ml<sup>-1</sup> of methanol-activated Bio-Beads SM2 resin (Bio-Rad) was added and allowed to mix overnight at 4°C. The heterogenous resin mixture was washed with resuspension buffer extensively to remove empty nanodiscs, and resin-bound MRP4-nanodisc complexes were eluted using buffer supplemented with 150 mM imidazole. The elution fraction was concentrated at 2000 g in a 100 kDa Amicon Ultra concentrator (Millipore), filtered, and purified by SEC on a Superdex 200 Increase column (Cytiva) in 20 mM Tris pH 8.0, 150 mM NaCl, 1 mM TCEP. All steps were performed at 4°C.

### **ATPase Assay**

ATP hydrolysis by MRP4 was observed using an established NADH-coupled ATPase assay [57] by monitoring  $\lambda_{ex} = 340$  nm and  $\lambda_{em} = 445$  nm on a SpectroMax plate reader. MRP4-nanodisc (400 nM), 60 mg mL<sup>-1</sup> pyruvate kinase (Sigma-Aldrich), 32 mg mL<sup>-1</sup> lactate dehydrogenase (Sigma-Aldrich), 4 mM phosphoenolpyruvate, and 150 mM NADH were mixed in 50 mM Tris pH 8.0, 150 mM KCl, 2 mM MgCl<sub>2</sub> buffer. For the ATP concentration dependency studies, ATP was added at the specified concentrations.



For investigation of substrate concentration dependence, ATP was held constant at 4 mM while substrate was added at the specified concentrations. The resulting data were analyzed using GraphPad Prism to fit the Michaelis-Menten equation.

### **Cryo-EM sample preparation and data acquisition**

Freshly purified MRP4 in lipid nanodiscs was concentrated to 0.6 mg ml<sup>-1</sup> for vitrification. Quantifoil R1.2/1.3 400-mesh Cu Holey Carbon Grids (EMS) were glow discharged at 15 mA for 30 s immediately before use. Sample was applied and grids were blotted using a Mark IV Vitrobot (Thermo Fisher Scientific) for 5 s at 100% humidity and 4°C before plunge freezing in liquid N<sub>2</sub>-cooled ethane. For the ATP-bound state, MRP4<sub>E1202Q</sub> in lipid nanodiscs was treated similarly, except for the addition of 1 mM PGE<sub>2</sub> and 10 mM ATP, 10 mM MgCl<sub>2</sub> followed by a 10 min incubation at 37°C prior to applying on grids. The substrate-bound samples were prepared similar to apo, except for the use of MRP4<sub>E1202Q</sub> in lipid nanodisc and the inclusion of 200 mM of either DHEA-S, PGE<sub>1</sub>, or PGE<sub>2</sub> or 400 mM cAMP. All three substrate-bound samples were blotted on Quantifoil R1.2/1.3 300-mesh Au Holey Carbon Grids (EMS). For all samples, grids were screened for ice quality and particle density using a Talos Arctica (Thermo Fisher Scientific) microscope.

For the nucleotide-free MRP4-nanodisc sample, 4698 118-frame super-resolution movies were collected on an FEI Titan Krios (Thermo Fisher Scientific) operated at 300 keV, equipped with a Bioquantum energy filter (Gatan) set to a slit width of 20 eV and a post-GIF K3 camera in single-electron counting mode. The dataset was collected with a

beam image-shift over a 3x3 hole array at a nominal magnification of 105,000x and physical pixel size of  $0.834 \text{ \AA pix}^{-1}$ , using an underfocus range of 1.0 to  $2.0 \mu\text{m}$ . SerialEM was used for all data acquisition using semi-automated scripts. The ATP-bound MRP4<sub>E1202Q</sub> dataset was collected on a different FEI Titan Krios using similar parameters, except for a physical pixel size of  $0.835 \text{ \AA pix}^{-1}$ . That dataset was composed of 3176 super-resolution movies collected at an underfocus ranging from 0.5 to  $2.0 \mu\text{m}$ .

All substrate-bound data was collected on this second FEI Titan Krios after an upgrade to Fringe-Free Imaging using a beam image-shift over a 3x3 hole array and recording 3 movies per hole. All datasets used an underfocus range of 0.5 to  $2 \mu\text{m}$ . The nominal magnification and physical pixel size after upgrade were unchanged. For the DHEA-S-bound MRP4 sample, 5609 80-frame super-resolution movies were collected. This data was merged with a dataset of 1266 movies collected at  $35^\circ$  tilt, collected using a single record per hole. 7219 80-frame super-resolution movies were collected on the PGE<sub>1</sub>-bound MRP4 sample and merged with 1034 80-frame super-resolution movies collected at  $35^\circ$  tilt collected using a single record per hole. Finally, 8649 80-frame super-resolution movies were collected on the PGE<sub>2</sub>-bound MRP4 sample.

## **Image processing**

MotionCor2 [58] was used to correct all movie stacks for beam-induced motion, to sum frames with and without dose weighting, and to Fourier bin images  $2 \times 2$  to the counting pixel size. The contrast transfer function (CTF) and resolution estimates for each corrected and dose weighted micrograph was determined in cryoSPARC [59] using

PatchCTF. Particles were picked in cryoSPARC 3.2 using a Gaussian disk as a template, and subsequently processed in cryoSPARC 3.2 as depicted in workflows shown in **Figures 1.10-1.14**.

### **Model building and structure refinement**

All five atomic models were built using Coot [60], PHENIX [61] and ISOLDE [62]. For the structures of apo- MRP4 and ATP-bound MRP4<sub>E1202Q</sub>, transmembrane helices and linkers were manually built in Coot using the output densities from DeepEMhancer [63]. The NBD models of the closely related bovine MRP1 (PDB: 6BHU), with residues mutated to those of MRP4 via Modeller [64] were initially used to build the NBDs of ATP-bound MRP4<sub>E1202Q</sub>. The final ATP-bound MRP4 NBDs were used to guide model building of the NBDs of apo- MRP4 and all three substrate-bound structures, first by rigid-body fitting in ChimeraX, followed by real-space refinement in PHENIX and further correction in Coot and ISOLDE. All three substrate-bound states were built by rigid-body fitting individual domains of apo- MRP4 into the output densities from DeepEMhancer and following the steps as above for NBDs.

The deposited apo- MRP4 model contains residues 47-398, 409-419, 427-615, 692-745, 756-1298. The deposited PGE<sub>1</sub>-bound MRP4 model contains residues 23-394, 409-615, 693-745, and 756-1298, as well as a one PGE<sub>1</sub> and one water molecule. The deposited PGE<sub>2</sub>-bound MRP4 model contains residues 46-394, 409-615, 693-745, and 756-1298, as well as one PGE<sub>2</sub> and one water molecule. The deposited DHEA-S-bound MRP4 model contains residues 10-398, 409-615, 693-745, and 756-1298, as well as one

DHEA-S and three water molecules. The deposited nucleotide-bound MRP4<sub>E1202Q</sub> model contains residues 48-394, 408-615, 696-746, 756-882, and 898-1298 as well as two bound ATP, two Mg<sup>2+</sup> ions, and a phosphatidylethanolamine lipid molecule. All models were validated against the sharpened densities from cryoSPARC. Visualizations and figures were prepared using UCSF Chimera [65], ChimeraX [66], and Inkscape software. Cavity calculations were made with MOLE*online* [67] and the 3V Server [68]. 2D diagrams of ligand-protein interactions were produced using LigPlot+ [69].

### **Data availability**

All five three-dimensional cryoEM density maps have been deposited to the Electron Microscopy Data Bank under accession numbers EMD-XXXX (apo MRP4), EMD-XXXX (PGE<sub>1</sub>-bound MRP4), EMD-XXXX (PGE<sub>2</sub>-bound MRP4), EMD-XXXX (DHEA-S-bound MRP4), and EMD-XXXX (ATP-bound MRP4<sub>E1202Q</sub>). The coordinates for the atomic models have been deposited in the Protein Data Bank under accession numbers XXXX (apo MRP4), XXXX (PGE<sub>1</sub>-bound MRP4), XXXX (PGE<sub>2</sub>-bound MRP4), XXXX (DHEA-S-bound MRP4), and XXXX (ATP-bound MRP4<sub>E1202Q</sub>). See **Table 1.1** for more details.

## **Acknowledgements**

We thank Phuong Nguyen for assistance with virus production and Daniel Asarnow for helpful discussions regarding purification and reconstitution of MRP4. This work was supported by the National Institute of General Medical Sciences (5P01GM111126 and NIGMS GM24485 to RMS and R35GM140847 to YC). Ruchika Bajaj was supported in part by American Heart Association postdoctoral fellowship Award No. 19POST34370101. Mass spectrometry was performed in the UCSF Mass Spectrometry facility supported by NIH grant P41 GM103481. We thank David P. Bulkley, Glenn Gilbert, and Mathew Harrington for support with cryoEM data collection. All data was collected at the UCSF cryoEM facility, which is supported by NIH grants S10OD020054, S10OD021741 and S10OD026881.

## **Author Contributions**

R.M.S., D.L.K., C.S.C, Y.C., and A.S. conceived this work; S.P., R.B. and G.M.K expressed and functionally characterized proteins; S.P., E.G. and M.G. collected and processed cyroEM data; S.P. and E.G. performed model building and refinement; S.P., R.B., E.G., R.M.S. and D.L.K. wrote the manuscript with contributions from all other authors.

## References

1. Chabowski, D.S., Cohen, K.E., Abu-Hatoum, O., Gutterman, D.D. & Freed, J.K. Crossing signals: bioactive lipids in the microvasculature. *Am J Physiol Heart Circ Physiol* **318**, H1185-H1197 (2020).
2. Harizi, H. & Gualde, N. The impact of eicosanoids on the crosstalk between innate and adaptive immunity: the key roles of dendritic cells. *Tissue Antigens* **65**, 507-14 (2005).
3. Martens, M.D., Fernando, A.S. & Gordon, J.W. A new trick for an old dog? Myocardial-specific roles for prostaglandins as mediators of ischemic injury and repair. *Am J Physiol Heart Circ Physiol* **320**, H2169-H2184 (2021).
4. Mitchell, J.A. & Kirkby, N.S. Eicosanoids, prostacyclin and cyclooxygenase in the cardiovascular system. *Br J Pharmacol* **176**, 1038-1050 (2019).
5. Oyesola, O.O. & Tait Wojno, E.D. Prostaglandin regulation of type 2 inflammation: From basic biology to therapeutic interventions. *Eur J Immunol* **51**, 2399-2416 (2021).
6. Vannuccini, S., Bocchi, C., Severi, F.M., Challis, J.R. & Petraglia, F. Endocrinology of human parturition. *Ann Endocrinol (Paris)* **77**, 105-13 (2016).
7. Zeilhofer, H.U. Prostanoids in nociception and pain. *Biochem Pharmacol* **73**, 165-74 (2007).
8. Biringer, R.G. The enzymology of the human prostanoid pathway. *Mol Biol Rep* **47**, 4569-4586 (2020).

9. Johnson, A.M., Kleczko, E.K. & Nemenoff, R.A. Eicosanoids in cancer: New roles in immunoregulation. *Front Pharmacol* **11**, 595498 (2020).
10. Mitchell, J.A. et al. Cyclooxygenases and the cardiovascular system. *Pharmacol Ther* **217**, 107624 (2021).
11. Wang, D., Cabalag, C.S., Clemons, N.J. & DuBois, R.N. Cyclooxygenases and prostaglandins in tumor immunology and microenvironment of gastrointestinal cancer. *Gastroenterology* **161**, 1813-1829 (2021).
12. Beaman, J., Prifti, C., Schwarz, E.B. & Sobota, M. Medication to manage abortion and miscarriage. *J Gen Intern Med* **35**, 2398-2405 (2020).
13. Klimko, P.G. & Sharif, N.A. Discovery, characterization and clinical utility of prostaglandin agonists for the treatment of glaucoma. *Br J Pharmacol* **176**, 1051-1058 (2019).
14. Lang, I.M. & Gaine, S.P. Recent advances in targeting the prostacyclin pathway in pulmonary arterial hypertension. *Eur Respir Rev* **24**, 630-41 (2015).
15. Lee, O.Y. et al. A comparative study of DA-9601 and misoprostol for prevention of NSAID-associated gastroduodenal injury in patients undergoing chronic NSAID treatment. *Arch Pharm Res* **37**, 1308-16 (2014).
16. Stephenson, M.L. & Wing, D.A. Misoprostol for induction of labor. *Semin Perinatol* **39**, 459-62 (2015).
17. Reid, G. et al. The human multidrug resistance protein MRP4 functions as a prostaglandin efflux transporter and is inhibited by nonsteroidal antiinflammatory drugs. *Proc Natl Acad Sci U S A* **100**, 9244-9 (2003).

18. Wen, J. et al. The pharmacological and physiological role of multidrug-resistant protein 4. *J Pharmacol Exp Ther* **354**, 358-75 (2015).
19. Rius, M., Thon, W.F., Keppler, D. & Nies, A.T. Prostanoid transport by multidrug resistance protein 4 (MRP4/ABCC4) localized in tissues of the human urogenital tract. *J Urol* **174**, 2409-14 (2005).
20. Tanaka, N., Kawai, J., Hirasawa, N., Mano, N. & Yamaguchi, H. ATP-Binding cassette transporter C4 is a prostaglandin D2 exporter in HMC-1 cells. *Prostaglandins Leukot Essent Fatty Acids* **159**, 102139 (2020).
21. Kalinski, P. Regulation of immune responses by prostaglandin E<sub>2</sub>. *J Immunol* **188**, 21-8 (2012).
22. Kochel, T.J., Reader, J.C., Ma, X., Kundu, N. & Fulton, A.M. Multiple drug resistance-associated protein (MRP4) exports prostaglandin E<sub>2</sub> (PGE<sub>2</sub>) and contributes to metastasis in basal/triple negative breast cancer. *Oncotarget* **8**, 6540-6554 (2017).
23. Zelcer, N. et al. Steroid and bile acid conjugates are substrates of human multidrug-resistance protein (MRP) 4 (ATP-binding cassette C4). *Biochem J* **371**, 361-7 (2003).
24. Chen, Z.S., Lee, K. & Kruh, G.D. Transport of cyclic nucleotides and estradiol 17- $\beta$ -D-glucuronide by multidrug resistance protein 4. Resistance to 6-mercaptopurine and 6-thioguanine. *J Biol Chem* **276**, 33747-54 (2001).
25. Hara, Y. et al. Inhibition of MRP4 prevents and reverses pulmonary hypertension in mice. *J Clin Invest* **121**, 2888-97 (2011).



26. Decouture, B. et al. Impaired platelet activation and cAMP homeostasis in MRP4-deficient mice. *Blood* **126**, 1823-30 (2015).
27. Li, C. et al. Spatiotemporal coupling of cAMP transporter to CFTR chloride channel function in the gut epithelia. *Cell* **131**, 940-51 (2007).
28. Moon, C. et al. Compartmentalized accumulation of cAMP near complexes of multidrug resistance protein 4 (MRP4) and cystic fibrosis transmembrane conductance regulator (CFTR) contributes to drug-induced diarrhea. *J Biol Chem* **290**, 11246-57 (2015).
29. Chen, Z.S. et al. Analysis of methotrexate and folate transport by multidrug resistance protein 4 (ABCC4): MRP4 is a component of the methotrexate efflux system. *Cancer Res* **62**, 3144-50 (2002).
30. Ci, L. et al. Involvement of MRP4 (ABCC4) in the luminal efflux of ceftizoxime and cefazolin in the kidney. *Mol Pharmacol* **71**, 1591-7 (2007).
31. Imaoka, T. et al. Functional involvement of multidrug resistance-associated protein 4 (MRP4/ABCC4) in the renal elimination of the antiviral drugs adefovir and tenofovir. *Mol Pharmacol* **71**, 619-27 (2007).
32. Kohler, J.J. et al. Tenofovir renal proximal tubular toxicity is regulated by OAT1 and MRP4 transporters. *Lab Invest* **91**, 852-8 (2011).
33. Ray, A.S. et al. Mechanism of active renal tubular efflux of tenofovir. *Antimicrob Agents Chemother* **50**, 3297-304 (2006).

34. Rius, M., Hummel-Eisenbeiss, J., Hofmann, A.F. & Keppler, D. Substrate specificity of human ABCC4 (MRP4)-mediated cotransport of bile acids and reduced glutathione. *Am J Physiol Gastrointest Liver Physiol* **290**, G640-9 (2006).
35. Rius, M., Hummel-Eisenbeiss, J. & Keppler, D. ATP-dependent transport of leukotrienes B4 and C4 by the multidrug resistance protein ABCC4 (MRP4). *J Pharmacol Exp Ther* **324**, 86-94 (2008).
36. Rius, M., Nies, A.T., Hummel-Eisenbeiss, J., Jedlitschky, G. & Keppler, D. Cotransport of reduced glutathione with bile salts by MRP4 (ABCC4) localized to the basolateral hepatocyte membrane. *Hepatology* **38**, 374-84 (2003).
37. Vogt, K. et al. Release of platelet-derived sphingosine-1-phosphate involves multidrug resistance protein 4 (MRP4/ABCC4) and is inhibited by statins. *Thromb Haemost* **118**, 132-142 (2018).
38. Hagmann, W. et al. Purification of the human apical conjugate export pump MRP2 reconstitution and functional characterization as substrate-stimulated ATPase. *Eur J Biochem* **265**, 281-9 (1999).
39. Mao, Q., Leslie, E.M., Deeley, R.G. & Cole, S.P. ATPase activity of purified and reconstituted multidrug resistance protein MRP1 from drug-selected H69AR cells. *Biochim Biophys Acta* **1461**, 69-82 (1999).
40. Shapiro, A.B. & Ling, V. ATPase activity of purified and reconstituted P-glycoprotein from Chinese hamster ovary cells. *J Biol Chem* **269**, 3745-54 (1994).
41. Sauna, Z.E., Nandigama, K. & Ambudkar, S.V. Multidrug resistance protein 4 (ABCC4)-mediated ATP hydrolysis: effect of transport substrates and

- characterization of the post-hydrolysis transition state. *J Biol Chem* **279**, 48855-64 (2004).
42. Berthier, J., Arnion, H., Saint-Marcoux, F. & Picard, N. Multidrug resistance-associated protein 4 in pharmacology: Overview of its contribution to pharmacokinetics, pharmacodynamics and pharmacogenetics. *Life Sci* **231**, 116540 (2019).
  43. Copsel, S. et al. Multidrug resistance protein 4 (MRP4/ABCC4) regulates cAMP cellular levels and controls human leukemia cell proliferation and differentiation. *J Biol Chem* **286**, 6979-88 (2011).
  44. Hayashi, H. et al. Sorting nexin 27 interacts with multidrug resistance-associated protein 4 (MRP4) and mediates internalization of MRP4. *J Biol Chem* **287**, 15054-65 (2012).
  45. Johnson, Z.L. & Chen, J. Structural basis of substrate recognition by the multidrug resistance protein MRP1. *Cell* **168**, 1075-1085 e9 (2017).
  46. Mi, W. et al. Structural basis of MsbA-mediated lipopolysaccharide transport. *Nature* **549**, 233-237 (2017).
  47. Hofmann, S. et al. Conformation space of a heterodimeric ABC exporter under turnover conditions. *Nature* **571**, 580-583 (2019).
  48. Sedzicki, J. et al. Mechanism of cyclic beta-glucan export by ABC transporter Cgt of *Brucella*. *Nat Struct Mol Biol* **29**, 1170-1177 (2022).

49. Choudhury, H.G. et al. Structure of an antibacterial peptide ATP-binding cassette transporter in a novel outward occluded state. *Proc Natl Acad Sci U S A* **111**, 9145-50 (2014).
50. Olsen, J.A., Alam, A., Kowal, J., Stieger, B. & Locher, K.P. Structure of the human lipid exporter ABCB4 in a lipid environment. *Nat Struct Mol Biol* **27**, 62-70 (2020).
51. Lee, K.P.K., Chen, J. & MacKinnon, R. Molecular structure of human KATP in complex with ATP and ADP. *Elife* **6**(2017).
52. El-Sheikh, A.A., van den Heuvel, J.J., Krieger, E., Russel, F.G. & Koenderink, J.B. Functional role of arginine 375 in transmembrane helix 6 of multidrug resistance protein 4 (MRP4/ABCC4). *Mol Pharmacol* **74**, 964-71 (2008).
53. Wittgen, H.G. et al. Phenylalanine 368 of multidrug resistance-associated protein 4 (MRP4/ABCC4) plays a crucial role in substrate-specific transport activity. *Biochem Pharmacol* **84**, 366-73 (2012).
54. Schuetz, J.D. et al. MRP4: A previously unidentified factor in resistance to nucleoside-based antiviral drugs. *Nat Med* **5**, 1048-51 (1999).
55. van Aubel, R.A., Smeets, P.H., Peters, J.G., Bindels, R.J. & Russel, F.G. The MRP4/ABCC4 gene encodes a novel apical organic anion transporter in human kidney proximal tubules: putative efflux pump for urinary cAMP and cGMP. *J Am Soc Nephrol* **13**, 595-603 (2002).
56. Kawahara, K., Hohjoh, H., Inazumi, T., Tsuchiya, S. & Sugimoto, Y. Prostaglandin E2-induced inflammation: Relevance of prostaglandin E receptors. *Biochim Biophys Acta* **1851**, 414-21 (2015).

57. Barnett, R.E. Effect of monovalent cations on the ouabain inhibition of the sodium and potassium ion activated adenosine triphosphatase. *Biochemistry* **9**, 4644-8 (1970).
58. Zheng, S.Q. et al. MotionCor2: anisotropic correction of beam-induced motion for improved cryo-electron microscopy. *Nat Methods* **14**, 331-332 (2017).
59. Punjani, A., Rubinstein, J.L., Fleet, D.J. & Brubaker, M.A. cryoSPARC: algorithms for rapid unsupervised cryo-EM structure determination. *Nat Methods* **14**, 290-296 (2017).
60. Emsley, P., Lohkamp, B., Scott, W.G. & Cowtan, K. Features and development of Coot. *Acta Crystallogr D Biol Crystallogr* **66**, 486-501 (2010).
61. Adams, P.D. et al. PHENIX: a comprehensive Python-based system for macromolecular structure solution. *Acta Crystallogr D Biol Crystallogr* **66**, 213-21 (2010).
62. Croll, T.I. ISOLDE: a physically realistic environment for model building into low-resolution electron-density maps. *Acta Crystallogr D Struct Biol* **74**, 519-530 (2018).
63. Sanchez-Garcia, R. et al. DeepEMhancer: a deep learning solution for cryo-EM volume post-processing. *Commun Biol* **4**, 874 (2021).
64. Sali, A. & Blundell, T.L. Comparative protein modelling by satisfaction of spatial restraints. *J Mol Biol* **234**, 779-815 (1993).
65. Pettersen, E.F. et al. UCSF Chimera--a visualization system for exploratory research and analysis. *J Comput Chem* **25**, 1605-12 (2004).

66. Goddard, T.D. et al. UCSF ChimeraX: Meeting modern challenges in visualization and analysis. *Protein Sci* **27**, 14-25 (2018).
67. Pravda, L. et al. MOLEonline: a web-based tool for analyzing channels, tunnels and pores (2018 update). *Nucleic Acids Res* **46**, W368-W373 (2018).
68. Voss, N.R. & Gerstein, M. 3V: cavity, channel and cleft volume calculator and extractor. *Nucleic Acids Res* **38**, W555-62 (2010).
69. Laskowski, R.A. & Swindells, M.B. LigPlot+: multiple ligand-protein interaction diagrams for drug discovery. *J Chem Inf Model* **51**, 2778-86 (2011).

## **Chapter 2: Symmetry reduction in a hyperpolarization-activated homotetrameric ion channel**

### **Contributing Authors**

Miles Sasha Dickinson<sup>1,2</sup>, Sergei Pourmal<sup>1,2</sup>, Meghna Gupta<sup>1,2</sup>, Maxine Bi<sup>1</sup>, Robert M. Stroud<sup>1</sup>

<sup>1</sup>Department of Biochemistry and Biophysics, University of California San Francisco, San Francisco, CA, USA.

<sup>2</sup>These authors contributed equally to this work

## Abstract

Plants obtain nutrients from the soil via transmembrane transporters and channels in their root hairs, from which ions radially transport in towards the xylem for distribution across the plant body. We determined structures of the hyperpolarization-activated channel AKT1 from *Arabidopsis thaliana*, which mediates K<sup>+</sup> uptake from the soil into plant roots. These structures of AKT1 embedded in lipid nanodiscs show that the channel undergoes a reduction of C4 to C2 symmetry, possibly to regulate its electrical activation.

## Introduction

Ion channels in plants perform a number of critical physiological tasks including the uptake of nutrients from the soil for plant development and viability, regulation of turgor pressure to control mechanical processes, and action potential-like electrical signaling [1]-[3]. Among the most important nutrients for plants is K<sup>+</sup>, for which there exist numerous validated channel genes in the model organism *Arabidopsis thaliana* [1], [3] including 6-transmembrane helix (TM) Shaker-like channels, 12-TM two-pore channels, 4-TM twin pore channels, and 2-TM Kir channels [1], [2]. The AKT1 channel is necessary for radial K<sup>+</sup> transport, where it mediates the translocation of K<sup>+</sup> from the rhizosphere into the root hair, from which the ion can diffuse through an outwardly-rectifying Stellar K<sup>+</sup> outward rectifying (SKOR) channel into the xylem for transport across the plant shoot [1], [4], [5]. The *Arabidopsis thaliana* akt1 gene, first discovered by phenotypic rescue of K<sup>+</sup> uptake-deficient yeast [6], encodes a 96,990 Dalton  $\alpha$ -subunit that assembles into a homotetrameric channel. The protein contains five distinct domains: 1) a Shaker-like



transmembrane cassette consisting of TM helices S1-S4 (constituting the voltage sensing domain) and S5-S6 (the pore domain); 2) an extended helical C-linker; 3) a cyclic nucleotide binding homology domain (CNBHD); 4) an Ankyrin repeat domain; and 5) a C-terminal KHA interaction domain.

In contrast to other putative cyclic nucleotide binding channels, AKT1 is unlikely to be regulated by cyclic nucleotide monophosphates (cNMPs) as it lacks critical residues for ligand binding that are present in bona-fide cyclic nucleotide binding domains (CNBDs) [7] (**Figure 2.6**). Instead, channel gating is voltage dependent and modulated by a phosphorylation 'switch' [1], [3], [8]-[10]. Yeast two-hybrid experiments show that the AKT1 Ankyrin repeat domain associates with a CIPK23 kinase / calcineurin B-like (CBL) calcium sensor complex, and patch clamp recording of current in *X. laevis* oocytes confirms that phosphorylation by this complex converts a nearly silent channel to a strongly hyperpolarization-activated channel with an activation threshold  $\sim -50$  mV [8]. Conversely, AKT1 can be inhibited by direct interaction with CBL10, or dephosphorylation by PP2C phosphatases [8], [11]. Phosphorylation couples channel activity, and thus K<sup>+</sup> uptake, to intricate Ca<sup>2+</sup> signaling networks in order for the plant to adapt to a range of soil conditions. Additionally, AKT1 is known to hetero-oligomerize with the pseudo-channel KC1, negatively shifting its  $V_{1/2}$  by  $\sim 60$  mV [11]. These modifications and interactions are critical for plant viability: activating modifications are necessary to facilitate the influx of K<sup>+</sup> against large concentration gradients when  $[K^+]_{\text{soil}}$  is low, and inhibition is needed to prevent K<sup>+</sup> leakage out of the roots when  $E_K$  is below  $V_m$ .

Here, we determined the structure of AKT1 from *A. thaliana* by single particle cryogenic electron microscopy (cryoEM) (**Figure 2.1A,B**). We reconstituted AKT1 into soy polar lipid nanodiscs and determined a C2-symmetric consensus structure to an average resolution of 2.8 Å. We observe a reduction of symmetry from the predicted C4 to C2, occurring in regions of the protein with known functional significance, namely the C-linker and CNBHDs. Heterogenous image processing of the consensus refinement reveals that the CNBHDs are highly mobile domains that flex about the channel axis, and that the C-linker alternates between two distinct conformations. Although the electrophysiological implications of these observations are yet to be determined, we suspect that similar processes may occur in other channels from the CNG and hyperpolarization-activated families.

## Results

The overall architecture of the AKT1 channel is similar to other non-domain-swapped ion channels such as the hyperpolarization-activated HCN1 [12], [13], KAT1 [14] and LliK [15] channels, the depolarization-activated ether-a-go-go channel [16], and ligand-gated CNGA1 channel [17]. In these channels, the S4 helix from the voltage sensing domain (VSD) that bears the gating charges is linked to the S5 helix of the pore domain via a short loop (**Figure 2.1A**) such that the pore and voltage sensing domains of the same subunit coalesce together as a bundle. This is in contrast to the canonical domain swapped architecture found in Shaker-like, NaV, and two-pore channels, in which the VSD and pore helices are separated by a long helical S4-S5 linker [13]. Our structure

is consistent with a de-active, closed channel in which the gating charges on S4 are in a resting, 'up' position (**Figure 2.1C**), and the intracellular activation gate is constricted to preclude the diffusion of ions through the central pore (**Figure 2.1D**). Previous work on the hyperpolarization-activated HCN1 channel showed that two gating charges are transferred downwards across the hydrophobic constriction site (HCS) during activation, accompanying a helical break in S4 [13]. In our structure, the corresponding charges are R164 and R167, which rest above the HCS formed by F100, while R169 and R170 are below the HCS closely interacting with an intracellular negative cluster formed by E61, D103 and D139 (**Figure 2.1C**).

The selectivity filter of AKT1 is nearly identical to all other K<sup>+</sup>-selective channels of known structure, consisting of a tetrameric "bracelet" arrangement of backbone carbonyls from the signature TVGYG motif (**Figure 2.1F**), mimicking the 8 water ligand field around K<sup>+</sup> ions in bulk solvent [18], [19] (**Figure 2.1D,E**). We assign four K<sup>+</sup> ions to densities on the channel axis within the selectivity filter which correspond to super-positions of alternately populated pairs of sites (**Figure 2.1E**). In addition, we observe a crown of four extracellular water molecules partially hydrating a S<sub>0</sub> K<sup>+</sup>, which are possibly hydrogen bonded to histidine residues (H260), conserved in plant inwardly-rectifying K<sup>+</sup> channels (**Figure 2.7A,B**) [20], that line the extracellular face of the channel. In this model, H260 donates a hydrogen bond from its δ nitrogen to its own backbone carbonyl, poising its putatively un-protonated δ nitrogen towards a crown water proton, thus aligning the water towards the S<sub>0</sub> K<sup>+</sup> (**Figure 2.7A**). The H260 imidazoles may facilitate partial dehydration of incoming K<sup>+</sup>•(H<sub>2</sub>O)<sub>8</sub> complexes by positioning the hydration crown, allowing the K<sup>+</sup> to

transition into a partially hydrated state (i.e.  $K^+(H_2O)_4(C=O)_4$ ) above the selectivity filter. Below the selectivity filter is an aqueous bath where  $K^+$  ions can re-hydrate, followed by an intracellular activation gate wherein the sidechains of I285 and T289 form an ion-excluding constriction point (**Figure 2.1D**).

Initial image processing with imposition of C4 symmetry showed high resolution features in the transmembrane domain, including an abundance of annular phospholipids,  $K^+$  ions in the selectivity filter and pore waters, but smeared density corresponding to intracellular domains. For this reason, we re-performed all 3D image processing without imposition of symmetry and also four-fold symmetry expanded the consensus C4 particle stack. Subsequent 3D classification produced multiple conformations of the channel, each exhibiting a dramatic reduction of symmetry from four to two-fold. Intriguingly, we observe the C-linker, which links the pore domain to the CNBHD, in two distinct configurations on the same C2-symmetric reconstruction. Neighboring AKT1 subunits adopt alternating C-linker conformations: the first conformation is termed 'flat', similar to that observed in the published structures of LliK [15] and HCN1 [12], whereas the second conformation is termed 'kinked' and resembles that of KAT1 [14]. Variations in C-linker and CNBD / CNBHD architecture have been observed between different channels though the exact nature of these differences is not always clear [7], [12], [14], [15], [17], [21]. Our structures suggest that these channels may sample multiple conformations during their respective activation cycles, and that there may be direct implications for regulation of electrical activation (**Figure 2.2A-D**).

In the kinked conformation, the C-linker forms an intricate interaction nexus with S6 and its neighboring protomer's VSD (**Figure 2.2A**). D337 is situated at the summit of the kink and forms an apparent salt bridge with R298 on S6. Y334 forms H-bonds with K180 at the bottom of S4 and R298, and also an aryl stacking interaction with F302 on S6. Furthermore, the kink appears to be stabilized by a close interaction between K333 and E339 from the C-linker itself. In the flat conformation, this nexus is significantly altered due to the intercalation of an N-terminal helix that precedes S1 (**Figure 2.2A,B**). This N-helix is only observed above the flat C-linker, where it makes extensive contacts with S6, the VSD, and the C-linker. The linkage between the N-helix and S1 is not resolved, yet we are able to confidently model a 12 amino acid stretch that well-satisfies the EM density and chemical environment (**Figure 2.2D, Figure 2.5D**).

In the flat conformer, the aryl interaction between Y334 and F302 is largely broken, as are the salt bridges between K333 and E339 and between D338 and R298 as D337 is forced to face away from S6 (**Figure 2.2A,E**). Although the exact functional consequence of these differences is still unclear, we propose that the insertion of the N-helix serves to autoregulate the electrical activation of S4. In order to activate the channel, S4 must translocate downwards to some extent [13], [14], [22], and the presence of the N-helix between it and the C-linker may sterically occlude this process (**Figure 2.2B**). The N-helix makes extensive contacts with the VSD, S6 and C-linker (**Figure 2.2D**). D18 forms an electrostatic bridge between K115 on the S2-S3 loop and K180 on the S4-S5 loop. E19 forms a salt bridge with R335 on the C-linker, and a multitude of Van der Waals interactions are satisfied between the N-helix, S6 and C-linker (**Figure 2.2B**). Finally, we

observe strong continuous density between C8 and C331 from the C-linker, suggesting that the N-helix may be covalently stapled to the C-linker (**Figure 2.2A,D, Figure 2.5D**)

Asymmetry is further observed in subsequent domains. The CNBHD that follows the flat C-linker is notably flexible, whereas the post-kinked CNBHD is resolved to high resolution allowing for accurate atomic structure determination. As a result of this asymmetry, the inter-CNBHD interactions around the channel ring differ considerably. Focused classification on the CNBHD domains from the original C1 particle stack of EM images without imposition of symmetry recovered three distinct states. The first of these has apparent C4 symmetry while the latter two have varying degrees of C2 symmetry (**Figure 2.2E**). At low contour levels, the Ankyrin domains are also seen to adopt a strongly-elongated C2 symmetric configuration in which two adjacent pairs of Ankyrin domains form close contacts with one another leaving a gap between these and the alternate pair of domains (**Figure 2.2F**). As the channel was heterologously expressed in mammalian cells without a CIPK/CBL10 phosphorylation system, we assume that the Ankyrin domains are unmodified. Therefore, it's feasible that Ankyrin phosphorylation alters this configuration for channel activation, possibly by breaking apart these inter-Ankyrin interactions to symmetrize the channel.

## **Discussion**

Although the precise role of symmetry breaking in a degenerate ligand-binding domain remains unclear, our results suggest that it might serve a regulatory role. The observed differences between adjacent CNBHD conformations is reminiscent of the

transition between apo- and cNMP-bound states of cyclic nucleotide-gated ion channels (**Figure 2.2C,D**), posing the possibility that this domain in AKT1 has been converted from a ligand-binding domain to a site of allosteric communication between the Ankyrins and the channel's pore. It is enticing to compare our observations with those of other CNBHD-containing channels whose electrical properties are altered by N- and C-terminal regulatory domains. In the case of hERG, an N-terminal helix acts in concert with the CNBHD to enhance the channel's activation kinetics and mar its speed of deactivation [23], [24]. In the depolarization-activated hERG channel, insertion of an N-terminal helix between its C-linker and VSD would, according to our model, push the S4 helix upwards towards an activated conformation, and prevent its deactivation into a resting, downwards state. Inversely, downwards translocation of S4 during activation in a hyperpolarization-activated channel such as AKT1 would be inhibited by the presence of such a helix. We hope that the unusual findings presented in this manuscript will help inform experiments on this very important plant channel, and on the many salient hyperpolarization- and CNBD-containing channels in human physiology.

## Figures

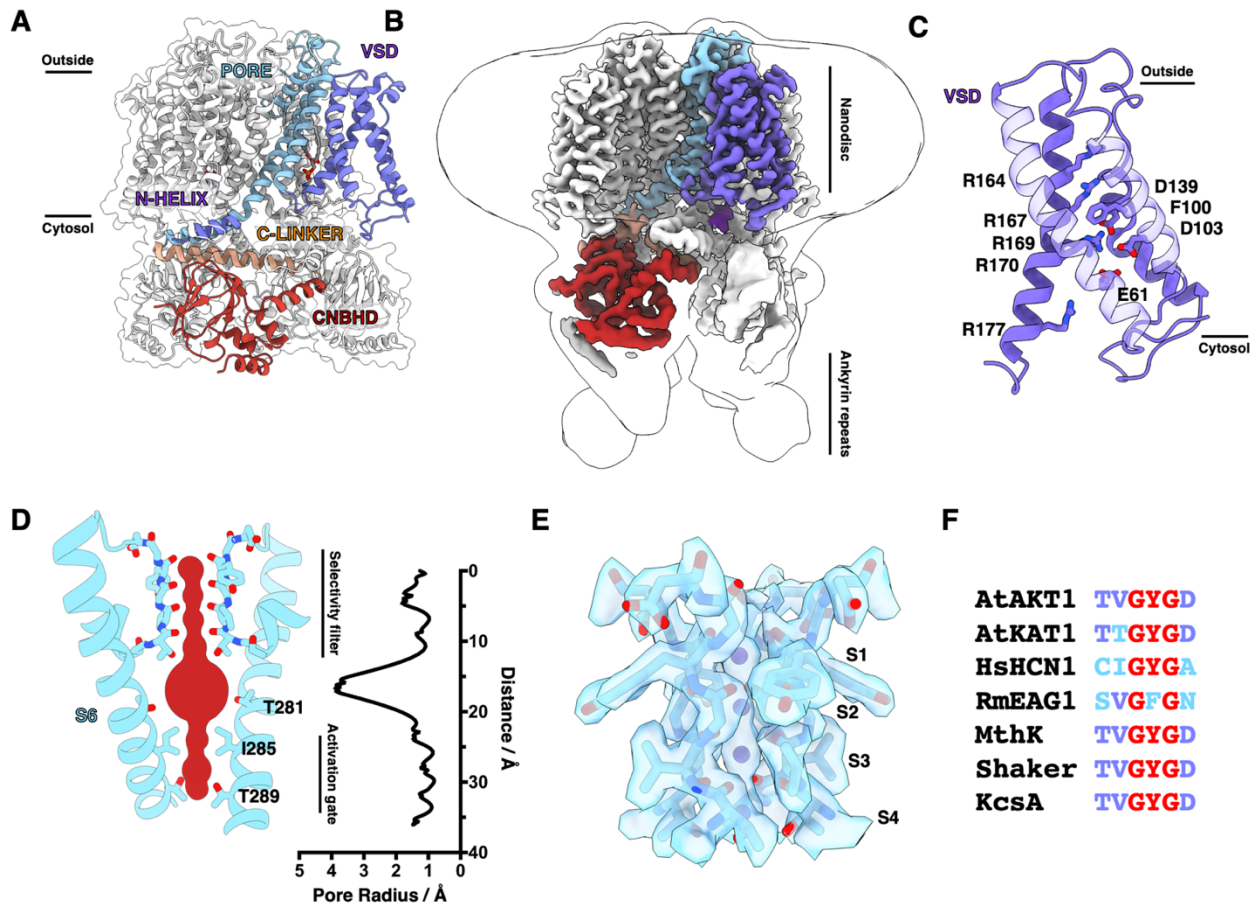


**Figure 2.1 | CryoEM structure and functional state of AKT1 in a lipid bilayer**

**a**, Molecular model of the AKT1 homotetramer with a single subunit colored by domain. **b**, Sharpened electrostatic potential map, colored by domain as in **a** with low-pass filtered envelope shown to depict the nanodisc and poorly-resolved Ankyrin repeats. **c**, The de-active voltage sensing domain with charge transfer center residues shown. **d**, Pore profile of the closed channel with pore-lining residues on the P-loop and S6 shown including the selectivity filter near the extracellular side, and activation gate at the intracellular side. The pore radius is shown plotted with respect to the distance along the channel axis, calculated using MOLE [25]. **e**, Atomic model of the selectivity filter and K<sup>+</sup> ion superpositions, with sharpened electrostatic potential map shown zoned 2.5 Å around the atoms of interest. **f**, Residues that form the selectivity filter from AKT1 and other K<sup>+</sup> channels, highlighting the signature GYG motif.



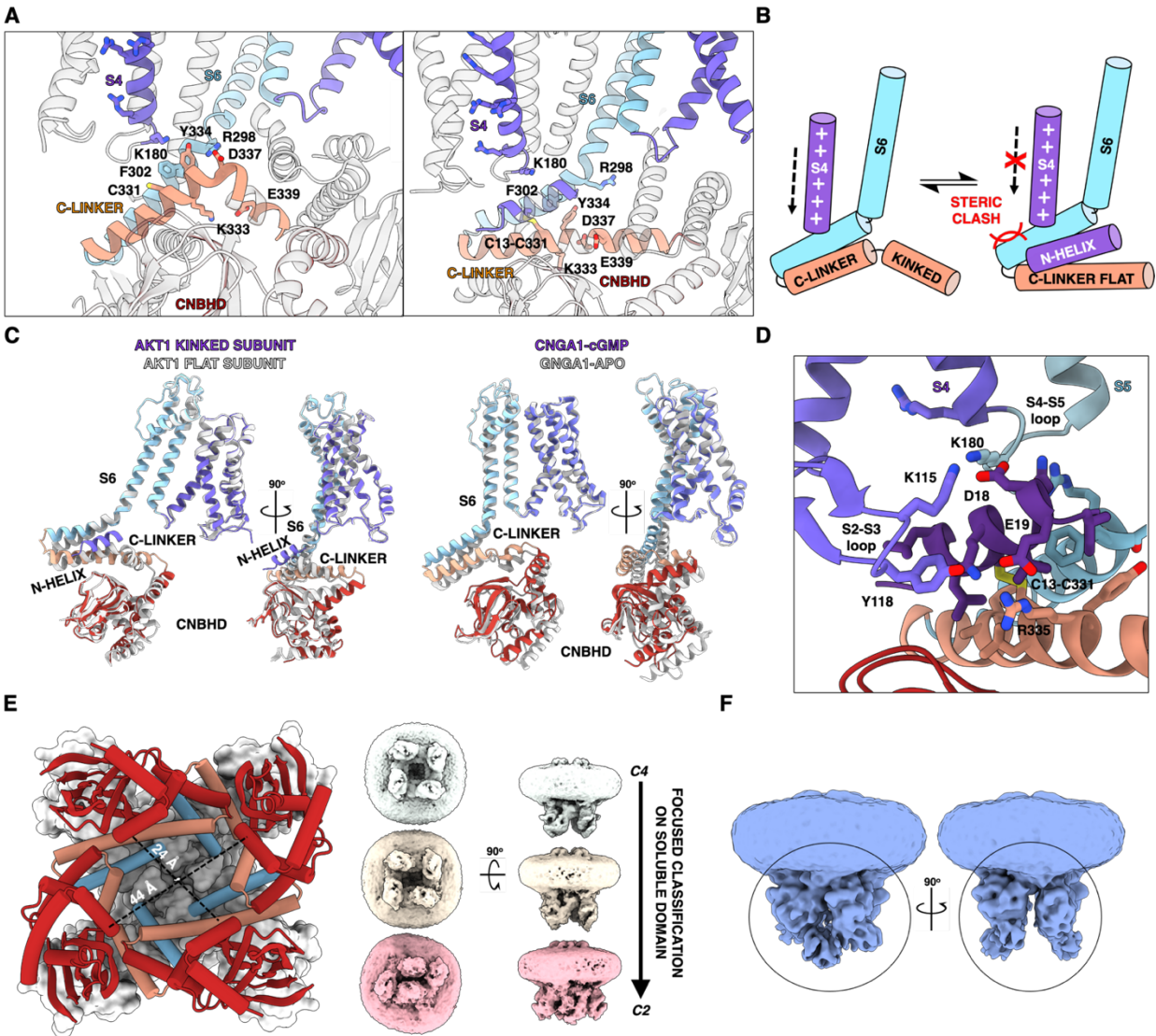


**Figure 2.2 | Symmetry reduction in AKT1 and its implications for voltage activation**

**a**, The C-linker adopts two different conformations in the C2-symmetric structure. In one conformation, the linker is kinked (left box), forming a nexus with S4 and S6. In the adjacent subunit, the C-linker is flattened by insertion of the pre-VSD N-terminal helix, breaking most atomic interactions in the nexus (right box). **b**, Graphical model of how N-helix insertion flattens the C-linker (represented by solid arrows) and potentially interferes with the downward translocation of S4 during membrane hyperpolarization (represented by dashed arrows). **c**, Orthogonal views of overlaid AKT1 kinked and flat subunits (left), and apo- and holo-CNGA1 (right) (PDBs: 7LFT and 7LFW, respectively) highlighting differences in C-linker and CNBD conformations. **d**, Atomic interactions between the N-helix, the VSD, C-linker and pore domain. **e**, Three conformations of the CNBHD domains are recovered from 3D classification (right), the C4 class at  $\sim 2.6$  Å displayed at top, mid-C2 class at  $\sim 2.8$  Å in the center (used for model building and atomic interpretation), and the ultra-C2 class at  $\sim 4.5$  Å on the bottom, all viewed at low contour. The soluble region

in the mid-C2 class was resolved to high resolution and was used to build an atomic model of AKT1, shown on the left. The degree of asymmetry is quantified by the distances between D337 on opposite C-linkers. **f**, Orthogonal views of the mid-C2 map, displayed at low contour to show the Ankyrin domains in two distinct configurations: one pair exhibits extensive inter-domain interactions while the neighboring pair does not touch.

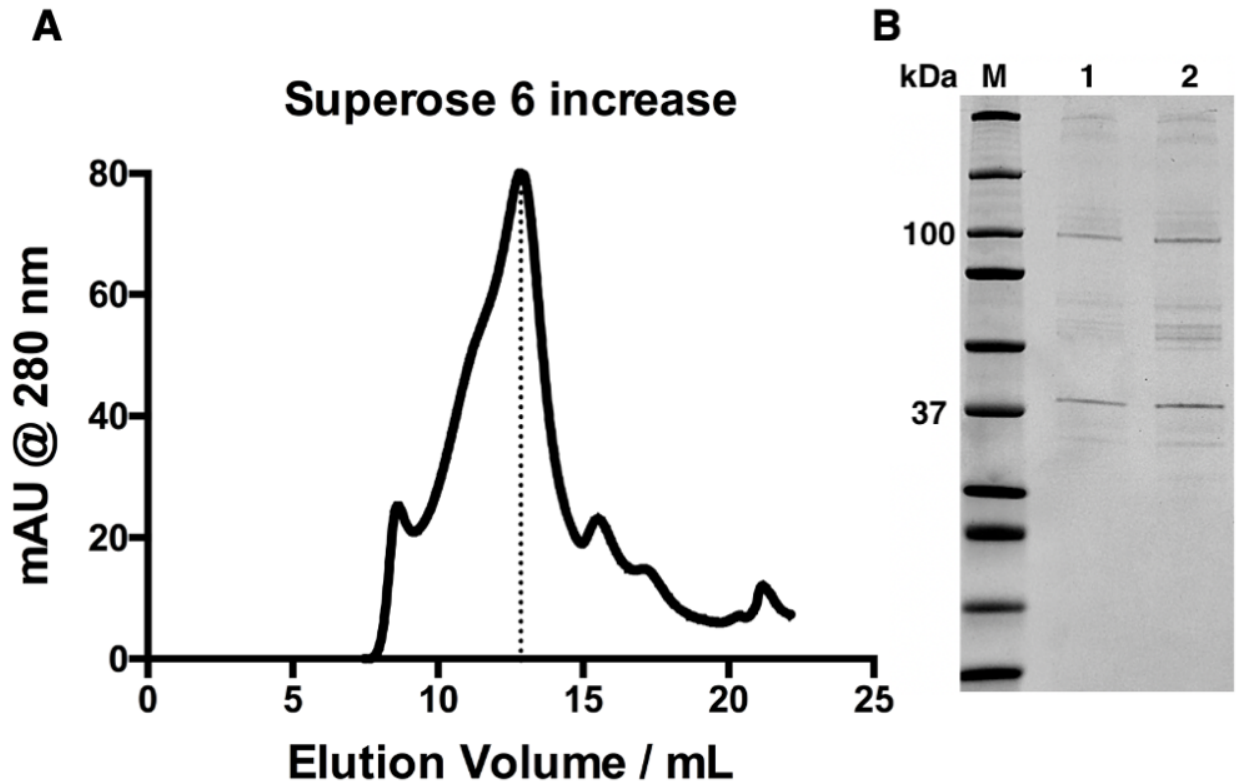


**Figure 2.3 | Purification of AKT1 from HEK GnTi- cells**

**a**, Size exclusion chromatogram of AKT1 post nanodisc reconstitution. The column is a Superose 6 increase 10/300. The dotted line indicates the elution volume of the peak fraction used for structure determination. **b**, SDS-PAGE gel of purified AKT1 showing a band for the protein at ~100 kDa and a band for MSP 2N2 at ~40 kDa.

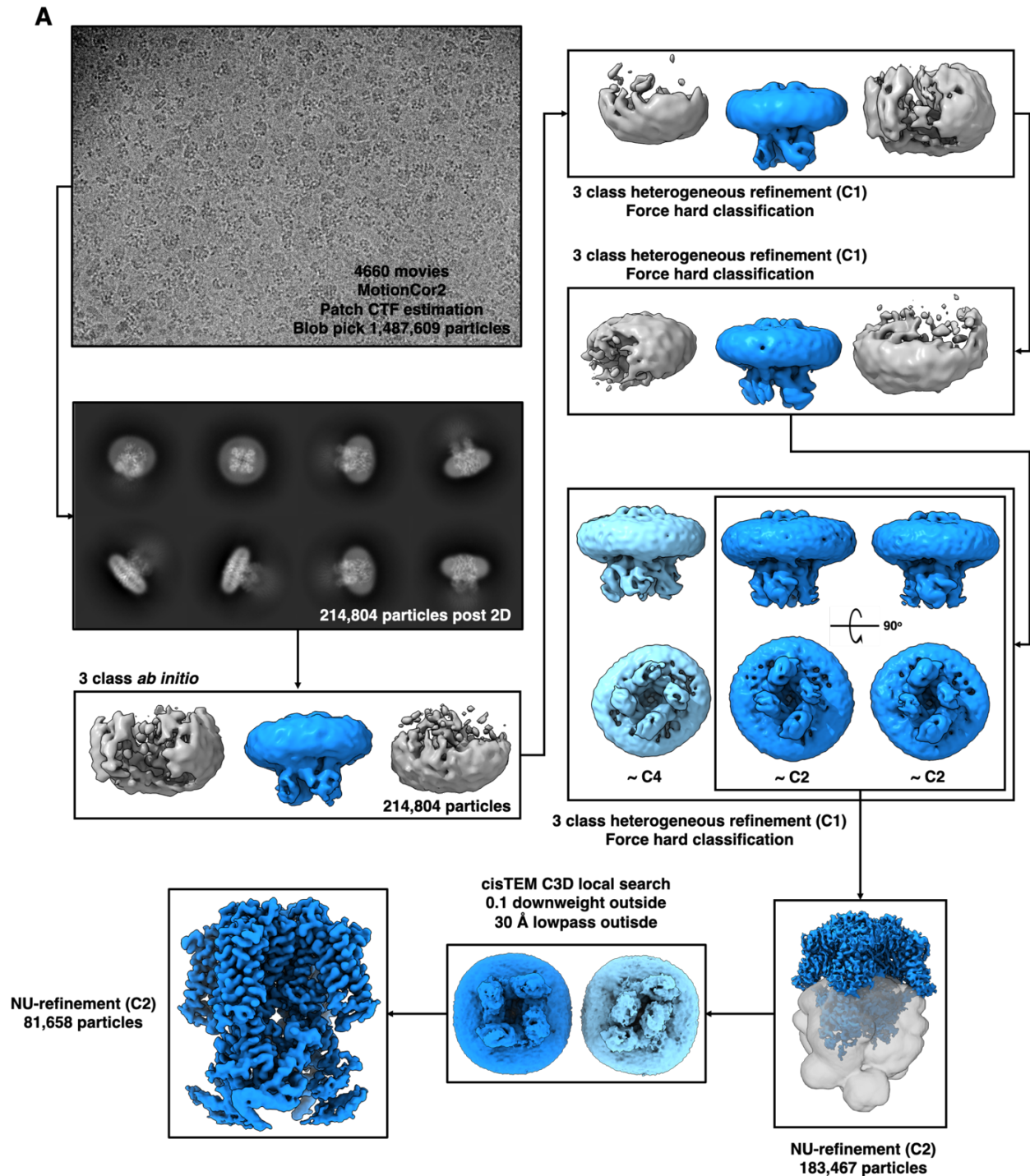


**Figure 2.4 | Image processing of AKT1 leading to a 2.8 Å cryo-EM reconstruction**  
Image processing scheme from movie alignment until final reconstruction. All steps use cryoSPARC v3.0 unless otherwise noted.



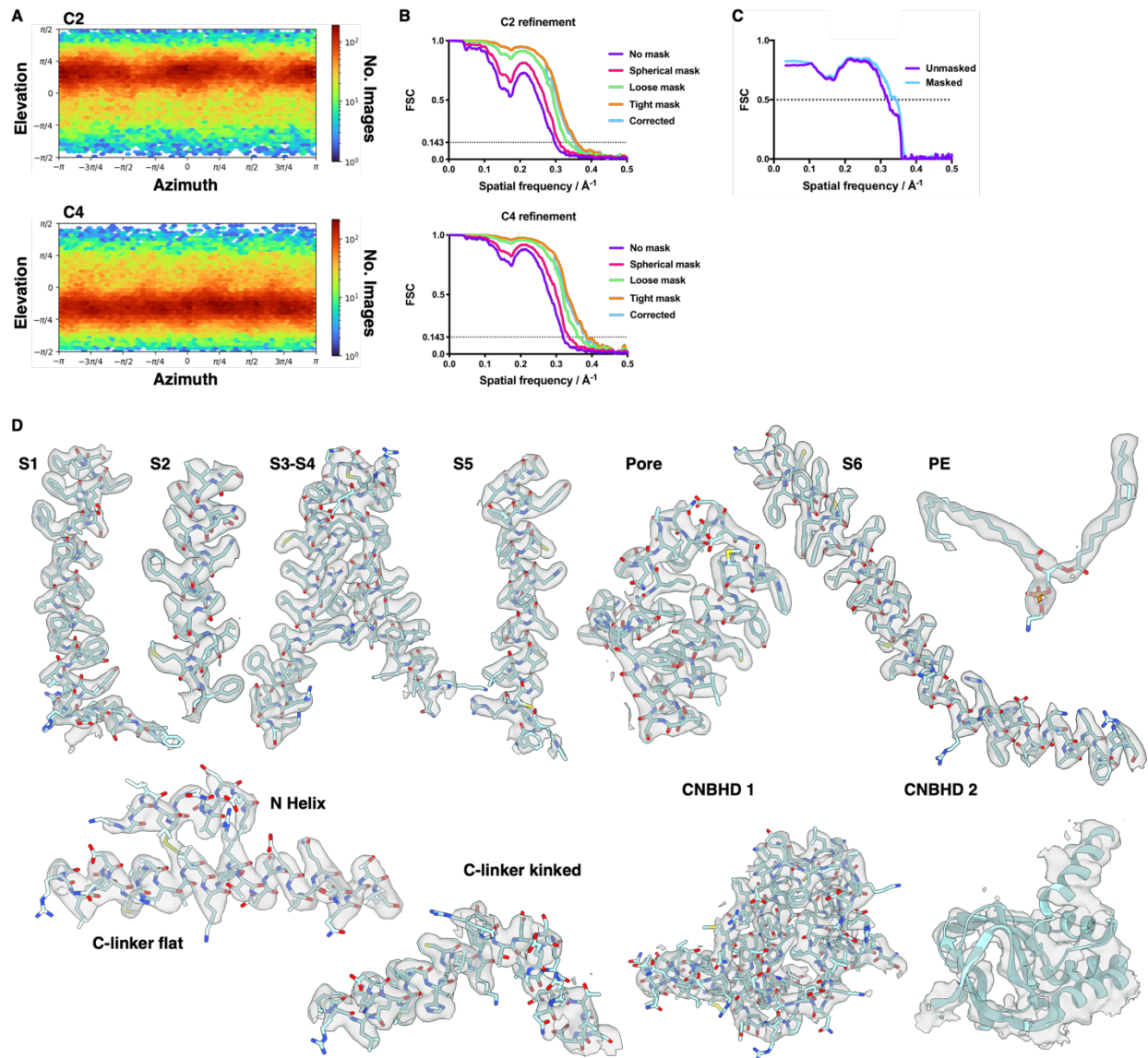


### Figure 2.5 | Cryo-EM map and model validation

**a**, Euler angle heat maps from the C2 and C4 symmetrized refinements. **b**, Gold-standard Fourier shell correlations (FSCs) from the C2 and C4 symmetrized refinements using 0.143 as the correlation threshold to determine average resolution. The masked/unmasked  $FSC_{0.143}$  resolutions for the C2 and C4 refinements are 2.8/3.3 and 2.6/3.0  $\text{\AA}$ , respectively. **c**, Map to model FSC for the atomic model and the high resolution C2-symmetrized reconstruction, using 0.5 as the correlation threshold. **d**, Sharpened electrostatic potential map from the 'mid-C2' refinement, zoned around each segment of the atomic model. The density around CNBHD2 was filtered to 5  $\text{\AA}$ .

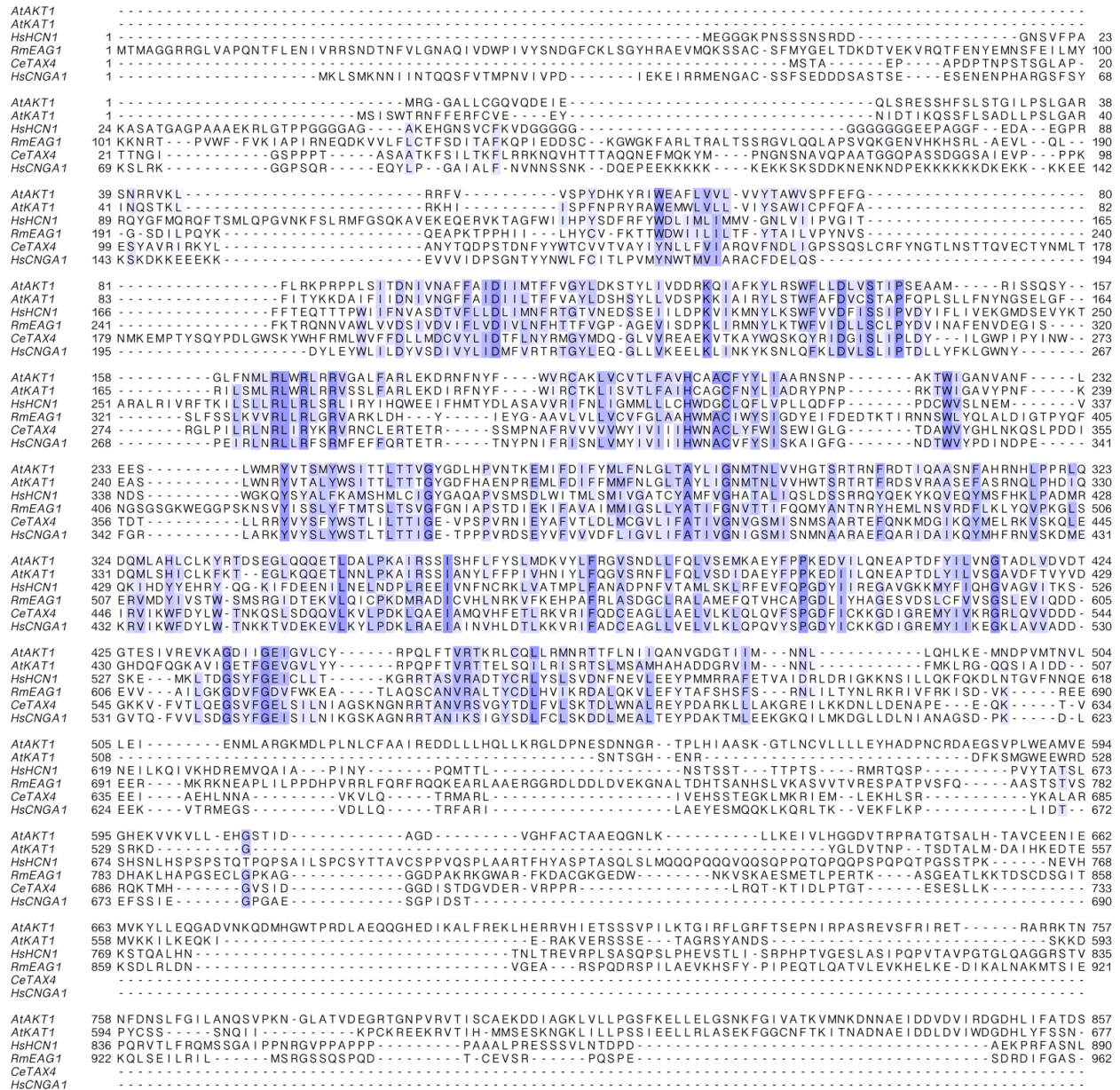


**Figure 2.6 | Sequence alignment of AKT1 and other cyclic nucleotide-gated and hyperpolarization-activated channels of known structure.**

**a, Alignment of *Arabidopsis thaliana* AKT1 (AtAKT1) with *Arabidopsis thaliana* KAT1 (AtKAT1), *Homo sapiens* HCN1 (HsHCN1), *Rattus norvegicus* EAG1 (RnEAG1), *Caenorhabditis elegans* TAX4 (CeTAX4), and *Homo sapiens* CNGA1 (HsCNGA1).**

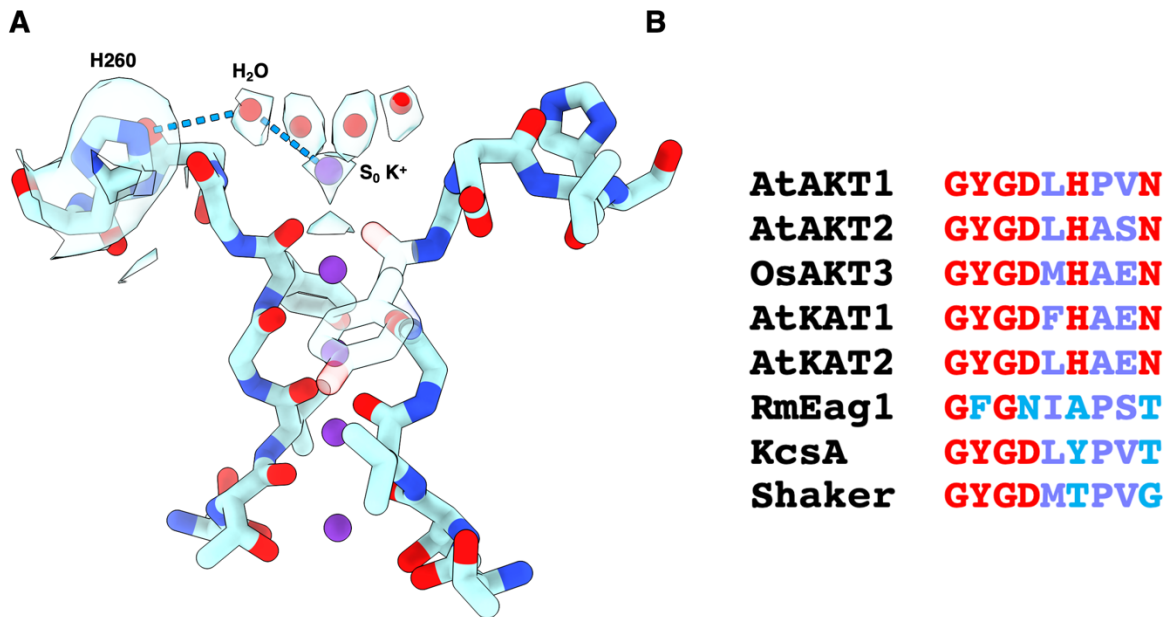


**Figure 2.7 | AKT1 pore structure and hydration**

**a**, Two pore loops of opposite chains are shown with density zoned around the modelled S<sub>0</sub> K<sup>+</sup> ion, its crown of four water molecules, and H260. **b**, Sequence alignment of the selectivity filter region of some K<sup>+</sup> channels showing the conservation of H260 among plant inward rectifiers. The AKT1 string begins with G255 and ends with N263.

## Tables

**Table 2.1 | Cryo-EM data collection, refinement, and validation statistics**

	AKT1 (EMD-25691) (PDB 7T4X)
<b>Data collection and processing</b>	
Microscope	Titan Krios G3
Imaging System	K3 BioQuantum, 20 eV slit
Voltage (kV)	300
Electron exposure (e <sup>-</sup> /Å <sup>2</sup> )	67
Exposure time (s)	5.9
Underfocus range (μm)	-0.7 to -1.5
Pixel size (super-resolution)	0.4175 Å pix <sup>-1</sup>
Frames per movie	117
Movies collected	4660
Acquisition software	SerialEM
Symmetry imposed	C2
Map resolution (Å)	2.8
FSC threshold	0.143
<b>Refinement</b>	
Model resolution (Å)	
Masked	2.9
Unmasked	3.1
FSC threshold	0.5
Model composition	
No. Atoms (non-hydrogen)	14,626
No. Residues	1778
No. Water	13
No. Ligands	K: 5 PTY: 2
R.m.s. deviations	
Bond lengths (Å) (# > 4σ)	0.005 (0)
Bond angles (°) (# > 4σ)	0.920 (0)
<b>Validation</b>	
MolProbity score	0.86
Clashscore	0.68
Ramachandran plot	
Favored (%)	98.63
Allowed (%)	1.37
Outliers (%)	0.00
Rama Z-score (RMSD)	
Whole	(N=1758) -0.26 (0.18)
Helix	(N=1142) -0.17 (0.14)
Sheet	(N=40) 1.01 (0.62)
Loop	(N=576) 0.09 (0.25)



## Methods

### AtAKT1 expression and purification

The full length *Arabidopsis thaliana* AKT1 (UniProt ID: Q38998) open reading frame was cloned into a AKT1-thrombin-eGFP-10xHis cassette within a pEG-BacMam HEK expression plasmid [26]. P2 virus was prepared in Sf9 cells and used to infect 1 L of HEK293 GnTi<sup>-</sup> cells growing at 37° C. 24 hr post infection, 10 mM sodium butyrate was added to the cells and the temperature was lowered to 30° C. 48 hr post induction with sodium butyrate, the cells were harvested by centrifugation at 1000 G. The cell pellets were resuspended in lysis buffer (50 mM HEPES pH 7.5, 200 mM KCl, 1 mM PMSF, 1 Roche cOmplete protease inhibitor tablet 100 mL<sup>-1</sup>) and Dounce homogenized 20-30 times with a type “B” piston.  $\beta$ -dodecylmaltoside ( $\beta$ -DDM) and cholesterol hemi-succinate (CHS) were added to concentrations of 1% and 0.2%, respectively, and the cells were solubilized for 2 hr at 4° C with gentle nutation. The insoluble material was removed by centrifugation at 30,000 rpm in a Ti45 rotor for 35 min, and the supernatant was incubated with 2 mL Talon resin for 2 hr along with 5 mM imidazole. The flow through was collected and the resin was washed with 5 column volumes each of buffer A (50 mM HEPES pH 7.5, 200 mM KCl, 0.05%  $\beta$ -DDM and 0.02% CHS) plus 5 mM and 10 mM imidazole. The protein was eluted from the resin with buffer A plus 150 mM imidazole and concentrated to ~500  $\mu$ L (using an Amicon 100 kDa MWCO filter) for injection onto a Superose 6 increase 10/300 column equilibrated in buffer A. The peak fractions were collected and concentrated to ~2 mg mL<sup>-1</sup> for nanodisc reconstitution.

## **AtAKT1 nanodisc reconstitution**

The membrane scaffold protein MSP 2N2 was expressed and purified from *E. coli*. For nanodisc reconstitution, 10 mg of soybean polar lipid extract (Avanti) dissolved in chloroform was dried into a film using a nitrogen stream and vacuum desiccated overnight to remove residual solvent. The lipid film was then solubilized in buffer B (50 mM HEPES pH 7.5, 200 mM KCl, 30 mM  $\beta$ -DDM) at a concentration of 10 mM and sonicated until clear. Purified AKT1 protein ( $\sim 2$  mg mL<sup>-1</sup>) was mixed with the soy polar lipid solution and MSP2N2 ( $\sim 2.4$  mg/ml) at a 4:10:125 (AKT1 monomer : MSP 2N2 : soy polar lipid) molar ratio and incubated on ice for 1 hr. MeOH washed Bio-beads SM2 (Bio-Rad) were added to the reconstitution mixture at  $\sim 40$  mg mL<sup>-1</sup> and incubated overnight at 4° C with nutation. Bio-beads were then removed from the mixture by gentle centrifugation. The reconstitution mixture was then batch bound to Ni<sup>2+</sup> NTA resin for 2 hr along with 10 mM imidazole. The resin was then washed with 5 CV each of buffer C (50 mM HEPES pH 7.5, 200 mM KCl) plus 10 mM and 40 mM imidazole in a gravity column. The nanodisc-reconstituted protein was eluted off of the resin with buffer C containing 250 mM imidazole. The elution was concentrated in an Amicon 50 kDa. MWCO concentrator to  $\sim 500$   $\mu$ L, then 0.22  $\mu$ m filtered and injected onto a Superose 6 increase 10/300 gel filtration column (GE Healthcare) equilibrated with buffer C. The peak fractions were pooled and concentrated to 0.4 mg mL<sup>-1</sup> for vitrification.

## Cryo-EM sample preparation and data acquisition

Vitrification was performed using a Mark IV Vitrobot with 100% relative humidity, a 4° C chamber, and a 5 s blot time with 0 blot force, on freshly plasma cleaned holey carbon 300 mesh gold R1.2/1.3 Quantifoil grids, using liquid nitrogen-cooled liquid ethane as the cryogen. Imaging was performed on the UCSF Titan Krios G3 operated at 300 kV, equipped with a Gatan K3 BioQuantum detector, using an energy slit width of 20 eV and correlated double sampling in super-resolution mode. Imaging was performed using beam-image shift over a 3x3 hole array, focusing once per stage shift, with a nanoprobe parallel beam, 70  $\mu\text{m}$  C2 aperture and no objective aperture. SerialEM [27] was used for automated data collection. The nominal EFTEM magnification was 105,000x resulting in a super-resolution pixel size on the specimen of 0.4175  $\text{\AA}$   $\text{pix}^{-1}$ . The dose rate on the camera was 8  $\text{e}^{-}$   $\text{pix}^{-1}$   $\text{s}^{-1}$  and 117 frame movies were collected over an accumulated fluence of 66  $\text{e}^{-}$   $\text{\AA}^{-2}$ .

## Image processing

Movies were drift corrected and dose weighted with MotionCor2 [28], and Fourier binned 2x to a pixel size of 0.835  $\text{\AA}$   $\text{pix}^{-1}$ . Dose weighted micrographs were imported into cryoSPARC v2.0 [29] and the contrast transfer function (CTF) was estimated in patches. Micrographs with CTF fit resolutions worse than 5  $\text{\AA}$  were discarded. ~800,000 particles were picked using Gaussian template matching, extracted in 432  $\text{pix}$  boxes, and subjected to 2D classification. 2D classes corresponding to ~400,000 particles were selected and used to calculate 3 *ab initio* volume classes using stochastic gradient

descent, one of which resembled the homotetrameric channel. The three classes were used in multi-reference classification using the “force hard classification” option in cryoSPARC. One class corresponding to ~ 120,000 particles was selected for refinement with C4 symmetry using “non-uniform refinement”, resulting in a 2.7 Å reconstruction.

The C4 volume displayed very high resolution features in the transmembrane domains, but was washed out in the soluble regions corresponding to the CNBDs and the Ankyrin repeats. 3D classification without imposition of symmetry was performed in cryoSPARC iteratively and two high resolution classes were recovered with apparent C2 and C4 symmetries. Particles from each class were refined against their respective models with imposition of their respective apparent symmetries. Further refinement of the C2 and C4 particle groups using the cryoSPARC v2.0 ‘non-uniform’ algorithm and subsequent refinement of per-particle defocus and per-image shift group beam tilt, trefoil and tetrafoil resulted in reconstructions at average resolutions of 2.8 and 2.6 Å, respectively.

The metadata for the refined particles were converted to star format using `csparc2star.py` (from Daniel Asarnow’s `pyem` package) and a single image stack was generated using `reliion preprocess` [30]. The image stack was imported into `cisTEM` [31] along with a binary mask around the intracellular soluble volume, and local angular search classification and refinement was performed using outside weights of 0 and 1, respectively and outside filtering to 30 Å. The resolutions allowed during classification and final refinement didn’t exceeded 8 and 6 Å, respectively.

## **Model building and structure refinement**

An initial model of AKT1 was generated in Phyre2 [32], using AtKAT1 (PDB: 6V1X) as a template, and the Ankyrin repeat domains were modeled using the crystal structure (PDB: 5AAR [33]). The model was refined manually using Coot [34] and Isolde [35] and validated using phenix.validation\_cryoem [36].

## **Acknowledgements**

We thank Phuong Nguyen for assistance with mammalian cell culture. We thank David Bulkley, Glen Gilbert and Zanlin Yu for their maintenance of the UCSF electron microscopy core, and the NIH grants that support them. We thank Paul Thomas, Matt Harrington, Joshua Baker-LePain and the Wynton HPC team for computational advice and support. We thank Janet Finer-Moore, Evan Green and Richard Aldrich for critical reading of the manuscript. M.S.D. acknowledges an NSF graduate research fellowship. Research was supported by NIH grant GM24485 (to R.M.S.).

## **Author Contributions**

M.S.D., S.P., M.G. and M.B. expressed and functionally characterized proteins; M.S.D., S.P., M.G. and M.B. collected and processed cryoEM data; S.P. and M.S.D. performed model building and refinement; M.S.D., S.P., M.B., and R.M.S. wrote the manuscript.

## References

1. Hedrich, R. Ion channels in plants. *Physiol. Rev.* **92**, 1777–1811 (2012).
2. Ward, J. M., Mäser, P. & Schroeder, J. I. Plant ion channels: gene families, physiology, and functional genomics analyses. *Annu. Rev. Physiol.* **71**, 59–82 (2009).
3. Sharma, T., Dreyer, I. & Riedelsberger, J. The role of K(+) channels in uptake and redistribution of potassium in the model plant *Arabidopsis thaliana*. *Front. Plant Sci.* **4**, 224 (2013).
4. Hirsch, R. E., Lewis, B. D., Spalding, E. P. & Sussman, M. R. A role for the AKT1 potassium channel in plant nutrition. *Science* **280**, 918–921 (1998).
5. Li, J. *et al.* The Os-AKT1 channel is critical for K<sup>+</sup> uptake in rice roots and is modulated by the rice CBL1-CIPK23 complex. *Plant Cell* **26**, 3387–3402 (2014).
6. Anderson, J. A., Huprikar, S. S., Kochian, L. V., Lucas, W. J. & Gaber, R. F. Functional expression of a probable *Arabidopsis thaliana* potassium channel in *Saccharomyces cerevisiae*. *Proc. Natl. Acad. Sci. USA* **89**, 3736–3740 (1992).
7. Matulef, K. & Zagotta, W. N. Cyclic nucleotide-gated ion channels. *Annu. Rev. Cell Dev. Biol.* **19**, 23–44 (2003).
8. Lee, S. C. *et al.* A protein phosphorylation/dephosphorylation network regulates a plant potassium channel. *Proc. Natl. Acad. Sci. USA* **104**, 15959–15964 (2007).
9. Hedrich, R. & Kudla, J. Calcium signaling networks channel plant K<sup>+</sup> uptake. *Cell* **125**, 1221–1223 (2006).

10. Xu, J. *et al.* A protein kinase, interacting with two calcineurin B-like proteins, regulates K<sup>+</sup> transporter AKT1 in Arabidopsis. *Cell* **125**, 1347–1360 (2006).
11. Ren, X.-L. *et al.* Calcineurin B-like protein CBL10 directly interacts with AKT1 and modulates K<sup>+</sup> homeostasis in Arabidopsis. *Plant J.* **74**, 258–266 (2013).
12. Lee, C.-H. & MacKinnon, R. Structures of the Human HCN1 Hyperpolarization-Activated Channel. *Cell* **168**, 111–120.e11 (2017).
13. Lee, C.-H. & MacKinnon, R. Voltage Sensor Movements during Hyperpolarization in the HCN Channel. *Cell* **179**, 1582–1589.e7 (2019).
14. Clark, M. D., Contreras, G. F., Shen, R. & Perozo, E. Electromechanical coupling in the hyperpolarization-activated K<sup>+</sup> channel KAT1. *Nature* **583**, 145–149 (2020).
15. James, Z. M. *et al.* CryoEM structure of a prokaryotic cyclic nucleotide-gated ion channel. *Proc. Natl. Acad. Sci. USA* **114**, 4430–4435 (2017).
16. Whicher, J. R. & MacKinnon, R. Structure of the voltage-gated K<sup>+</sup> channel Eag1 reveals an alternative voltage sensing mechanism. *Science* **353**, 664–669 (2016).
17. Xue, J., Han, Y., Zeng, W., Wang, Y. & Jiang, Y. Structural mechanisms of gating and selectivity of human rod CNGA1 channel. *Neuron* **109**, 1302–1313.e4 (2021).
18. Zhou, Y., Morais-Cabral, J. H., Kaufman, A. & MacKinnon, R. Chemistry of ion coordination and hydration revealed by a K<sup>+</sup> channel-Fab complex at 2.0 Å resolution. *Nature* **414**, 43–48 (2001).
19. Morais-Cabral, J. H., Zhou, Y., MacKinnon, R. Energetic optimization of ion conduction rate by the K<sup>+</sup> selectivity filter. *Nature* **414**, 37–42 (2001).

20. Hoth, S. *et al.* Molecular basis of plant-specific acid activation of K<sup>+</sup> uptake channels. *Proc. Natl. Acad. Sci. USA* **94**, 4806–4810 (1997).
21. Li, M. *et al.* Structure of a eukaryotic cyclic-nucleotide-gated channel. *Nature* **542**, 60–65 (2017).
22. Dai, G., Aman, T. K., DiMaio, F. & Zagotta, W. N. The HCN channel voltage sensor undergoes a large downward motion during hyperpolarization. *Nat. Struct. Mol. Biol.* **26**, 686–694 (2019).
23. Muskett, F. W. *et al.* Mechanistic insight into human ether-à-go-go-related gene (hERG) K<sup>+</sup> channel deactivation gating from the solution structure of the EAG domain. *J. Biol. Chem.* **286**, 6184–6191 (2011).
24. Gustina, A. S. & Trudeau, M. C. hERG potassium channel gating is mediated by N- and C-terminal region interactions. *J. Gen. Physiol.* **137**, 315–325 (2011).
25. Pravda, L. *et al.* MOLEonline: a web-based tool for analyzing channels, tunnels and pores (2018 update). *Nucleic Acids Res.* **46**, W368–W373 (2018).
26. Goehring, A. *et al.* Screening and large-scale expression of membrane proteins in mammalian cells for structural studies. *Nat. Protoc.* **9**, 2574–2585 (2014).
27. Schorb, M., Haberbosch, I., Hagen, W. J. H., Schwab, Y. & Mastrorarde, D. N. Software tools for automated transmission electron microscopy. *Nat. Methods* **16**, 471–477 (2019).
28. Zheng, S. Q. *et al.* MotionCor2: anisotropic correction of beam-induced motion for improved cryo-electron microscopy. *Nat. Methods* **14**, 331–332 (2017).

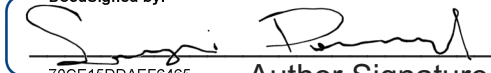


29. Punjani, A., Rubinstein, J. L., Fleet, D. J. & Brubaker, M. A. cryoSPARC: algorithms for rapid unsupervised cryo-EM structure determination. *Nat. Methods* 14, 290–296 (2017).
30. Zivanov, J. et al. New tools for automated high-resolution cryo-EM structure determination in RELION-3. *Elife* 7, (2018).
31. Grant, T., Rohou, A. & Grigorieff, N. cisTEM, user-friendly software for single-particle image processing. *Elife* 7, e35383 (2018).
32. Kelley, L. A., Mezulis, S., Yates, C. M., Wass, M. N. & Sternberg, M. J. E. The Phyre2 web portal for protein modeling, prediction and analysis. *Nat. Protoc.* 10, 845–858 (2015).
33. Clark, M. D., Contreras, G. F., Shen, R. & Perozo, E. Electromechanical coupling in the hyperpolarization-activated K<sup>+</sup> channel KAT1. *Nature* 583, 145–149 (2020).
34. Emsley, P., Lohkamp, B., Scott, W. G. & Cowtan, K. Features and development of Coot. *Acta Crystallogr. Sect. D, Biol. Crystallogr.* 66, 486–501 (2010).
35. Croll, T. I. ISOLDE: a physically realistic environment for model building into low-resolution electron-density maps. *Acta Crystallogr. D Struct. Biol.* 74, 519–530 (2018).
36. Adams, P. D. et al. PHENIX: a comprehensive Python-based system for macromolecular structure solution. *Acta Crystallogr. Sect. D, Biol. Crystallogr.* 66, 213–221 (2010).

## Publishing Agreement

It is the policy of the University to encourage open access and broad distribution of all theses, dissertations, and manuscripts. The Graduate Division will facilitate the distribution of UCSF theses, dissertations, and manuscripts to the UCSF Library for open access and distribution. UCSF will make such theses, dissertations, and manuscripts accessible to the public and will take reasonable steps to preserve these works in perpetuity.

I hereby grant the non-exclusive, perpetual right to The Regents of the University of California to reproduce, publicly display, distribute, preserve, and publish copies of my thesis, dissertation, or manuscript in any form or media, now existing or later derived, including access online for teaching, research, and public service purposes.

DocuSigned by:  
  
70CE15DDAEF6465... Author Signature

3/20/2023  
Date